2025-11

Solar Energy Assessment using Data-driven and Physical Models: Application for Crystalline Silicon Photovoltaic Systems in Ethiopia

Gedifew, Assaye

Bahir Dar University

College of Science

Department of Physics

Solar Energy Assessment using Data-driven and Physical Models: Application for Crystalline Silicon Photovoltaic Systems in Ethiopia

By

Assaye Gedifew Yismaw

November, 2025
Bahir Dar, Ethiopia

Bahir Dar University

College of Science

Department of Physics

Solar Energy Assessment using Data-driven and Physical Models: Application for Crystalline Silicon Photovoltaic Systems in Ethiopia

By

Assaye Gedifew Yismaw

A Dissertation Submitted in Partial Fulfillment of the Requirements for the Degree of Doctor of Philosophy (Ph.D) in Condensed Matter Physics: Solar Energy.

Principal Supervisor: Amare Benor Belay

- Associate Professor of Physics
- Department of Physics
- Bahir Dar University
- Bahir Dar, Ethiopia

Bahir Dar University
College of Science
Department of Physics

Declaration

This is to certify that the thesis entitled "***Solar Energy Assessment using Data-driven and Physical Models: Application for Crystalline Silicon Photovoltaic Systems in Ethiopia***", submitted in partial fulfillment of the requirements for the degree of Doctor of Philosophy in Condensed Matter Physics: Solar Energy in Department of Physics, Bahir Dar University, is a record of original work carried out by me and has never been submitted to this or any other institution to get any other degree or certificates. The assistance and help I received during this investigation have been duly acknowledged.

Assaye Gedifew Yismaw

Bahir Dar University
College of Science
Department of Physics

Approval of Dissertation

I hereby certify that I have supervised, read, and evaluated this dissertation entitled ***"Solar Energy Assessment using Data-driven and Physical Models: Application for Crystalline Silicon Photovoltaic Systems in Ethiopia"*** by Assaye Gedifew Yismaw prepared under my guidance. I recommend the dissertation be submitted for oral defense.

Research Supervisor: _____ Dr. Amare Benor Belay

Department Head: _____ Dr. Tamiru Nigussie

Bahir Dar University
College of Science
Department of Physics

Approval of Dissertation Defense Result

As members of the board of examiners, we examined this dissertation entitled ***"Solar Energy Assessment using Data-driven and Physical Models: Application for Crystalline Silicon Photovoltaic Systems in Ethiopia"*** by Assaye Gedifew Yismaw. We hereby certify that the dissertation is accepted for fulfilling the requirements for the award of the degree of Doctor of Philosophy in Condensed Matter Physics: Solar Energy.

Board of Examiners

External Examiner 1:	(XXXXXXXXXXXXXXXXXXX)
External Examiner 2:	(XXXXXXXXXXXXXXXXXXX)
Internal Examiner 1:	(XXXXXXXXXXXXXXXXXXX)
Internal Examiner 2:	(XXXXXXXXXXXXXXXXXXX)
Research Supervisor:	Dr. Amare Benor Belay
Chair Person:	(XXXXXXXXXXXXXXXXXXX)

Acknowledgment

I want to express my sincere gratitude to my principal supervisors, Dr. Amare Benor from Bahir Dar University for his invaluable guidance and support throughout my doctoral studies. His expertise, encouragement, and solid belief in my abilities have been instrumental in completing this research. Additionally, I am thankful to Dr. Ambelu Tebabal for his unwavering support and encouragement, which have been invaluable in navigating the challenges of doctoral research. Their integral perspective and scientific insights have profoundly impacted my understanding of the subject matter. Furthermore, I am deeply thankful to Bahir Dar University, Injibara University, and the International Science Program for their generous financial support, which has made this research possible. The National Meteorological Institute (NMI) of Ethiopia, NASA Power data archive, and MERRA-2 for providing the ground observational and satellite data essential for this research are also great fully acknowledged. I also want to thank the developers of the Python programming language and ArcGIS software for the indispensable tools used in data analysis and visualization. Special thanks are also extended to Canadian Solar-Datasheet for providing crucial technical specifications. Finally, I would like to express my heartfelt appreciation to my parents and friends for their support, encouragement, and care throughout this journey.

Abstract

Solar radiation, the electromagnetic energy emitted from the Sun, is a fundamental driver of Earth's weather and climate systems and represents a vast, clean energy source. Global solar radiation (GSR) is the total amount of solar radiation (both direct and diffuse) reaching a horizontal surface on Earth. It is a key measurement for evaluating the solar energy potential of a specific location, which in turn is essential for assessing the expected performance and efficiency of solar photovoltaic (PV) system. Thus, the accurate measurement and estimation of GSR is crucial for assessing and utilizing solar energy resources at both global and local scales. Hence, this study investigates estimations of GSR and assesses the performance of crystalline silicon (c-Si) PV cells/modules across Ethiopia, by utilizing a comprehensive approach that integrates data-driven and physical models. The study also implemented various optimization techniques such as determining the optimum tilt angle and tracking mechanisms. For this purpose, twelve machine learning (ML) and one stacked/ensembled model were trained and validated with hourly, daily and monthly ground-based global solar radiation data from 16 synoptic weather stations (2020-2022), supplemented by meteorological, aerosol, and sky condition data from MERRA-2 and NASA POWER archives. The three stations with distinct weather patterns were withheld from the model development process for model transferability/generality test. A stacked/ensemble model (i.e., constructed by stacking better performing separate models) showed exceptional predictive performance with error metric values ranging (R^2: 0.956-0.963; RMSE: 9.938-11.784 W/m^2) for all time scales. With this performance capability we generated a high-resolution (1° x 1°) global solar radiation data across Ethiopia for the year 2022, and the distribution showed a precise spatial and seasonal dependence with the highest in spring (i.e., 594 - 641 W/m^2; eastern and northeastern) and lowest in summer (i.e., 359 – 405 W/m^2; western and southern parts of the nation). Such analogs were also observed on the peak sun hours and plane-of-array (POA) irradiance distribution with their annual value ranging from 4.83 – 6.57 kWh/m^2/day and 0.65 – 1.05 kW/m^2, respectively, across the nation. Here it's worth noting that to model POA irradiance, we implemented five decomposition and six transposition models (i.e., thirty different independent combinations). Furthermore, we incorporated POA irradiance into a single diode PV cell model to evaluate c-Si PV cell performances. Consequently, the annual PV cell temperature, ranging

from 38.84°C to 55.45°C, significantly impacted device parameters. The short-circuit current (J_{sc}) mirrored POA irradiance trends, while the open-circuit voltage (V_{oc}) showed an inverse temperature dependence. The annual PV cell efficiency varied from 13.02% to 22.35%, with clear average seasonal variations such as the highest in spring (20.72%) and the lowest in summer (16.01%). Besides, optimal PV module tilt angles and implementation of different tracking mechanisms were determined. The monthly optimal tilt angles ranged from 0° (July) to 47.90° (January), while seasonal averages were observed as 29.40° (winter), 21.65° (autumn), 12.34° (spring), and 8.8° (summer). The annual optimal tilt angle varied from 14.51-21.52°. In addition, the performance of different tracking mechanisms (dual/full axis: DAT, vertical-axis: V-axis, east-west/incline east-west: EW/IEW, north-south: NS) were also evaluated. Dual/full axis tracking yielded the highest annual average efficiency (44.89%), while NS tracking resulted in a 28.46% energy loss compared to horizontal mounting. On the other hand, PV module mounted at optimal tilt angle resulted in a 4.12% gain, while EW/IEW and vertical axis tracking yielded 43.12% and 24.94% energy gains, respectively compared to horizontally mounted. Overall, this study provides a valuable resource for selecting, comparing, and designing future solar PV systems in Ethiopia. It contributes to strategic PV deployment by aiding in energy assessment and forecasting. Moreover, the study offers an optimal tilt angle model, guiding the selection and implementation of the best tracking mechanisms for PV modules/panels in Ethiopia. This information is essential for effective energy assessment and forecasting across the nation.

Publications:

1. **A. Gedifew**, G. M. Tsidu, A. Tebabal, A. Benor, Estimating Solar Radiation by using Machine Learning for Improved Photovoltaic System Design. Under Review on Journal of Renewable and Sustainable Energy
2. **A. Gedifew**, G.M. Tsidu, and A. Benor, Spatial and temporal variability of crystalline silicon solar cell performance in Ethiopia: A hybrid approach. ***Energy Reports***, 13, 3369-3378, (2025).
3. **A. Gedifew**, and A. Benor, Evaluating the impact of tilt angles and tracking mechanisms on photovoltaic modules in Ethiopia. ***Frontiers in Energy Research: Solar Energy***, 12, 1519725, (2025).
4. G. Yirga, U. J. P. Raju, **A. Gedifaw**, and A. Nigusie, Tree-based machine learning and global models for long-term rainfall estimation: intercomparison and evaluation over Bahir Dar, Ethiopia. ***Journal of Water and Climate Change***, *16*(2), 344-360, (2025).
5. A. Benor, **A. Gedifew**, S. Yigizaw, and K. Davis, Patterning Indium Tin Oxide Using Self-Assembled Monolayers as Etch Resists for Photovoltaic and Display Devices. ***ACS Applied Nano Materials***, *5*(5), 6505-6512, (2022).
6. S. Yigzaw, **A. Gedifew**, N. Bekri, B. Gebremichael, and A. Benor, Effect of ozone plasma on the electronic properties of PEDOT: PSS. ***AIP Advances***, *15*(7), (2025).
7. S. Yigzaw, N. Bekri, **A. Gedifew**, S. Alayau, and A. Benor, Effect of visible light on the electrical conductivity of conductive grade PEDOT: PSS. ***Materials Research Express***, *(2025)*.
8. S. Yigizaw, N. Bekri, **A. Gedifew**, D. Alemu, T. Matsushima and A. Benor, Impact of Oxidation on the Electrical and Surface Property PEDOT_PSS, Under review in ***Materials Advances*** *Journal.*

Conference and Seminar Presentation:

1. **A. Gedifew**, G.M. Tsidu, and A. Benor, Spatial and temporal variability of crystalline silicon solar cell performance in Ethiopia: A hybrid approach. *Energy Reports*, 13, (2025), ***5th African Graduate Students Conference (AGSC V-BDU-2025).***
2. **A. Gedifew**, G.M. Tsidu, and A. Benor, Spatial and temporal variability of crystalline silicon solar cell performance in Ethiopia: A hybrid approach. *Energy Reports*, 13, (2025), ***13th Annual Science Conference on Recent Trends in Scientific Research (NCRTSR-2025).***
3. **A. Gedifew**, G. M. Tsidu, A. Tebabal, A. Benor, Estimating Solar Radiation by using Machine Learning for Improved Photovoltaic System Design. Final Decission in Helyion Journal, ***Department of Physics, Bahir Dar University, Bahir Dar, Ethiopia.***

Dedication

- This dissertation work is dedicated to those with a vested interest in the rigorous investigation and intellectual advancement of this field of solar energy assessment and forecast.

Table of Contents

Contents **Page**

List of Tables

List of Figures

Acronyms

ASSD	*All sky surfaces downward*	kNN	*k-nearest neighbor*
CSSD	*Clear sky surface downward*	XGB	*Extreme gradient boost*
Lat.	*Latitude*	GB	*Gradient boost*
Lon.	*Longitude*	AdaB	*AdaBoost*
Temp.	*Temperature*	CNN	*Convolutional neural network*
SZA	*Solar zenith angle*	LSTM	*Long-short term model*
GSR	*Global solar radiation*	MLR	*Multi-linear regression*
Eleva	*Elevation*	RF	*Random forest*
PSH	*Peak sun hour*	DHI	*Diffused horizontal irradiance*
Decl.	*Declination angle*	DT	*Decision tree*
DNI	*Direct normal irradiance*	POA	*Plain of array irradiance*
WD	*Wind direction*	LGB	*Light gradient boost*
WS	*Wind speed*	SVM	*Supportive vector machine*
AOD	*Aerosol optical depth*	MAE	*Mean average error*
PM	*Particulate matter*	MSE	*Mean square error*
NASA	*National aeronautics and space administration*	RMSE	*Root mean square error*
MERR-2	*Modern-era retrospective analysis for research and applications, version 2*	MAPE	*Mean average percentage error*
NMI	*National meteorological institute*	NSE	*Nash-Sutcliffe efficiency*
ANN	*Artificial neural network*	Albedo	*Surface albedo*

Symbols

$\sum$	*Summation*	V_{oc}	*Open circuit voltage*
H_T	*Total irradiance on the tilted surface*	V_{mp}	*Voltage at maximum power point*
H_b	*Direct or beam irradiance*	P_{mp}	*Maximum power*
H_d	*Diffused irradiance*	FF	*Fill factor*
H_r	*Reflected irradiance*	η	*Efficiency*
T_a	*Ambient temperature*	T_c	*PV cell temperature*
κ_T	*Clearness index*	P_t	*POA irradiance*
P_{dc0}	*DC-power reference condition*	T_{ref}	*Reference temperature*
γ_{pdc}	*Temperature coefficients power*	V_{mp-ref}	*Voltage at maximum power point at reference conditions*
α_{sc}	*Normalized temperature coefficient for I_{sc}*	V_{oc-ref}	*Open circuit voltage at reference conditions*
I_{mp-ref}	*Current at maximum power point at reference conditions*	l, m, y	*Compensation coefficient*
I_{sc-ref}	*Short circuit current at reference conditions*	P_{ref}	*Irradiance at reference condition*
I_{L-ref}	*Light-generated current at reference conditions*	q	*Charge*
I_{o-ref}	*Diode saturation current at reference conditions*	E_g	*Energy band gap*
I_x	*Current at module V = 0.5*V_{oc}*	$E_g(0)$	*Energy band gap at 0 ^oK*
I_{xx}	*Current at module V = 0.5*(V_{oc} +V_{mp})*	V_{th}	*Thermal velocity*

I_{mp}	*Current at the maximum power point*	A	*Area of cell/module*
I_{sc}	*Short circuit current*	N_P	*Number of cells in parallel*
V_{mp-ref}	*Voltage at maximum power point at reference conditions*	N_S	*Number of cells in series*
V_{oc-ref}	*Open circuit voltage at reference conditions*	V_{NS}	*Voltage generated by N_S*
R_s	*Series resistance*	I_{NP}	*Current generated by N_P*
R_{sh}	*Shunt resistance*	$I_{NP,MP}$	*Current at maximum power point by N_P*
β_{voc}	*Temperature coefficient for module open-circuit-voltage*	$V_{NS,MP}$	*Voltage at maximum power point by N_S*
α_{mp}	*Normalized temperature coefficient for I_{mp}*	ξ_{pj}	*Predicted solar radiation*
R	*Correlation coefficient*	ξ_{pj}	*Observed solar radiation*
θ	*Incidence angle*	β	*Tilt angle*
θ_Z	*Zenith angle*	β_{Opt}	*Optimum tilt angle*
α	*Elevation angle*	γ	*Azimuth angle*
J_{sc}	*Short circuit current density*	$\bar{\xi_p}$	*Mean values*
J_o	*Reverse saturation current density*	^{o}	*Degree*

Chapter 1

1. Introduction

1.1. Background of the Study

Solar radiation, the electromagnetic energy emitting from the Sun, is a primary driver of Earth's climatic and weather systems.[1,2] It also constitutes a vast source of clean energy. Global solar radiation (GSR) is the total amount of solar radiation/energy (both direct and diffuse) reaching a horizontal surface on Earth.[3] Due to the increasing concerns about global warming and depleting fossil fuel reserves require a paradigm shift towards sustainable energy sources.[4] Of the different sustainable/renewable energy sources, solar energy is a top candidate due to its abundance, cleanliness, and long-term sustainability.[5] Regarding this, photovoltaic (PV) cells/panels, are the most important device for converting solar radiation into electrical energy via the photoelectric effect.[6] The working principle and its components of a typical PV cell are illustrated in Figure 1-1. Due to their maturity, market dominance (covers roughly 95% of all solar cells)[7], long-term stability (with a typical lifespan > 25 years and an annual power degradation rate below 1%)[8], standardization, better efficiency[9], and cost-effectiveness (i.e., high efficiency reduces installation costs)[10], silicon solar cells are the most widely used technology for solar energy assessment, generation, and forecasting. Crystalline silicon (c-Si) solar cells have reduced grain boundaries and fewer charge recombination centers, which makes them an ideal material for achieving higher efficiency in silicon-based PV devices compared to amorphous silicon (a-Si).[11] However, this efficiency is influenced by a complex interplay between intrinsic device characteristics and extrinsic environmental factors.[12,13] Among environmental factors, solar radiation is a primary and key factor governing the overall performance of these PV cells.[14] Understanding the effect of solar radiation pattern on PV cell performance provides insight into the indirect effects of other environmental parameters, such as temperature and cloud cover. For instance, a specific region with consistently high solar radiation levels often experiences higher ambient

temperatures and greater thermal extremes, which can negatively impact cell efficiency. Which likely implies that the increased solar irradiance generally leads to higher current and power output, but also elevates cell temperature, which can reduce voltage and overall efficiency.[15] Conversely, area with lower solar radiation levels, often due to significant cloud cover, will have reduced power output. Therefore, solar radiation serves as a central variable, whose influence on cell performance is inherently linked to and reflects the impact of other environmental conditions. Thus, the efficient PV systems assessment and forecasting relay on the quality/ability to measure/predict spatiotemporal (location and time: hourly, daily, monthly, seasonal and annual) variation of solar radiation that will offers vital insights for PV system design, including anticipated device performance stability and backup battery capacity requirements. Furthermore, these fluctuations, in turn, affect the intricate processes within the PV cell, including light absorption, charge carrier generation, and separation, charge transport and collection, and leakage currents.[16] This inherent link between PV performance and solar irradiance underscores the critical need for spatiotemporal irradiance prediction/estimation. Such predictions provide a key parameter for accurately assessing PV power generation potential.[17] Besides, linking the operating parameters of the PV cell/module with detailed device physics, incorporating the spatiotemporal dimension of irradiance for a specific site or region, forms the foundation for comprehensive PV power assessment and generation prediction.

However, accurate spatiotemporal solar irradiance prediction is a complex task due to the high variability of atmospheric conditions, leading to a spectrum of modeling approaches with varying trade-offs between complexity and accuracy. Simple empirical models, such as the Angström-Prescott model, are easy to implement and require minimal data, making them useful in data-scarce regions.[18,19] However, their primary limitation is the oversimplification of atmospheric physics, which fails to account for dynamic factors like cloud type, aerosol content, and water vapor, resulting in poor accuracy outside of their specific calibration conditions. Linear regression and time series models offer a balance of simplicity and interpretability but often struggle to capture

complex non-linear relationships or long-term trends effectively.[20] A significant leap in complexity involves advanced machine learning (ML) models like tree-based and simple neural networks.[21,22] These data-driven models learn complex, non-linear relationships from multiple atmospheric parameters, surpassing empirical and time-series models in accuracy. Yet, their performance is constrained by the need for relative substantial historical data and their less ability to effectively capture the intricate spatiotemporal dependencies inherent in weather patterns. The most sophisticated methods are deep learning (DL) models, particularly Recurrent Neural Networks (RNNs) and Long Short-Term Memory (LSTMs), which excel at learning long-term dependencies in sequential data, making them ideal for time-series forecasting.[23,24] Additionally, Convolutional Neural Networks (CNNs) can analyze satellite imagery to assess cloud cover and its impact on irradiance.[25] While DL models offer the highest predictive accuracy, their drawbacks are the immense computational resources and vast datasets required for training, as well as their "black box" nature, which makes their decision-making process difficult to interpret. On the other hand, hybrid or ensemble models that combine the strengths of different approaches are increasingly being explored to achieve a better balance of accuracy, efficiency, and interpretability.[26] The GSR is converted to plane of array (POA) irradiance through the application of decomposition models and transposition models and further incorporated in to PV cell/module model.[27]

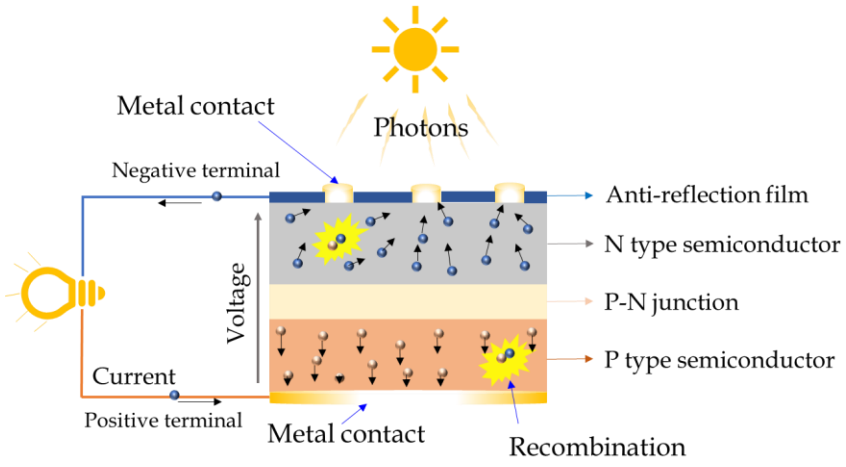

Figure 1-1: A typical PV cell components and its working principle.

Ethiopia, a nation endowed with substantial solar irradiation in East Africa, currently demonstrates a significantly low level of solar energy utilization within the regional context.[28] Despite being one of the least electrified countries, Ethiopia is actively exploring alternative energy sources, with solar power emerging as a promising path for sustainable development.[29] Indeed, the implementation of solar energy technologies offers a multifaceted approach to address the nation's energy challenges and global climate/environmental concerns. [30,31] Consequently, this study presents a novel hybrid approach for assessing solar radiation estimation and solar cell performance's spatial and temporal variability across Ethiopia. For this purpose, a 15-minute GSR data were obtained from sixteen Ethiopian synoptic stations operated by the National Meteorology Institute (NMI) for 2020-2022. Upon the twelve distinct machine learning models such as Multiple Linear Regression (MLR)[32], Artificial Neural Network (ANN)[33], k-nearest Neighbors (KNN)[34], Decision Tree (DT)[35], and Support Vector Regression (SVR)[36], AdaBoost (Ada)[37], XGBoost (XGB)[38], Random Forest (RF)[39], Light Gradient Boosting Regressor (LGB)[40], and Gradient Boosting (GB)[41], Long Short-Term Memory (LSTM)[42] and Convolutional Neural Networks (CNN)[43] and a single stacked/ensembled model (i.e., constructed by stacking kNN, XGB, RF, GB, DT, and LGB) were trained and evaluated across diverse climatic conditions to estimate GSR. The 15-minute interval GSR data by Pyranometer SP-Lite and CMP3 instruments, were aggregated to the desired time resolutions (like hourly, daily, and monthly) to enhance computational efficiency during the analysis. High-resolution (i.e., hourly) temperature, wind speed and wind direction data were also obtained from the same station. Furthermore, supplementary feature variables, including all-sky surface downward radiation (ASSD), clear sky-surface downward radiation (CSSD), aerosol optical depth (AOD), particulate matter with a diameter of 2.5 micrometers or less (PM2.5), and others, were incorporated from the Modern-Era Retrospective Analysis for Research and Applications, Version 2 (MERRA-2) archive maintained by the National Aeronautics and Space Administration (NASA). Thereafter, we generated accurate, high resolution (1^{o} by 1^{o}), average GSR maps for the entire country by leveraging a stacked/ensemble machine learning model for the year

2022. These maps, combined with detailed physical models of c-Si solar cells (such as four-parameter single-diode model – for its predictive power and computational efficiency) and PV modules (i.e., for real-world or outdoor performance), enabled a comprehensive evaluation of device performance across different regions and seasons. In addition, the study framework utilizes a diverse set of thirty (i.e., five decomposition and six transpositions: three isotropic and three anisotropic models) POA irradiance models, encompassing both direct and diffuse solar radiation components, to refine solar irradiance estimations for deployed PV cells and/or modules.[44] The five decomposition models like Erbs *et al.*[45], DISC[46], Boland *et al.*[47], Louche *et al.*[48], and Orgill-Holland[49] implemented to derive DNI, and DHI. Then the three isotropic such as Liu-Jordan[50], Badescu[51], and Koronakis[52] and three anisotropic models Reindl *et al.*[53], Hay[54], and Steven-Unsworth[55] transposition models also implemented to estimate POA irradiance. These improved POA irradiance data are subsequently integrated into established four-parameter single-diode PV cell physical model. This physical model incorporates critical electrical parameters that characterize the PV cell performance, including reverse saturation current density (J_o), short-circuit current density (J_{sc}), short-circuit current (I_{sc}), open-circuit voltage (V_{oc}), fill factor (FF), maximum power (P_{mp}), and efficiency (η). Furthermore, the study also integrated optimum tilt angle, and various tracking mechanisms to maximize the amount of solar irradiance incident on solar PV module/panel for specific location across the nation. This comprehensive approach enables a more realistic and accurate evaluation of solar cell/module performance. Overall, the study provides valuable insights for optimizing Ethiopia's PV system design, deployment, and energy forecasting, facilitating informed decision-making in the country's transition to renewable energy sources.

1.2. Statement of the Problem

The core challenge in solar energy assessment and PV system performance modeling, particularly in data-scarce regions like Ethiopia, is the lack of long-term, high-

resolution, and reliable ground-based GSR data. According to Benti *et al.*, less the five of Ethiopia's 90 national meteorological stations are equipped to measure GSR.[56] Moreover, even at these few stations, existing GSR data often contain significant gaps or are unreliable due to equipment malfunctions and other technical issues. This scarcity relays empirical models for estimating GSR have been limited by low accuracy and poor generalizability and advanced data-driven models like DL are also constrained by their extensive data requirement and high computational demands. Additional complicating this issue is the absence of comprehensive studies that integrate these advanced data-driven and physical models for PV cell/module performance optimization in Ethiopia. The efficiency of c-Si PV cells/modules is a dynamic function of both internal device characteristics and an assembly of external meteorological factors, mainly solar radiation, temperature that also reveal spatiotemporal variation themself. A thorough understanding of these interactions is crucial for optimizing performance through mechanisms like tilt angle and tracking systems. However, a significant research gap exists in applying and validating these integrated methodologies to the specific climatic and geographical conditions of Ethiopia. Therefore, implementing a robust, physics-informed, data-driven framework for accurate GSR estimation and subsequent PV performance assessment for c-Si cell/module in Ethiopia was a critical need. The problem lies in creating a methodology that overcomes the limitations of data scarcity by integrating accessible datasets—from ground-based observations to reanalysis and satellite sources—with advanced ML/DL and ensembled models. This approach not only bridge the gap between data availability and the need for accurate solar resource data but also pioneer the application of integrated physical and data-driven models for optimizing PV system performance, thereby supporting sustainable energy development in data-poor environments.

Furthermore, despite significant year-on-year growth in global solar PV installations, reaching a record 553 GW in 2024, the current pace of deployment is insufficient to meet the ambitious climate goals set by international bodies.[57] The

Intergovernmental Panel on Climate Change (IPCC) highlights the urgent need for over 80% of energy to come from renewable sources to limit global warming to under 2°C and achieve net-zero carbon emissions.[58] This discrepancy between the rapid, yet inadequate, growth of solar PV and the required transition to a renewable-dominated energy landscape presents a critical problem: the current trajectory of solar PV deployment is not aligned with the scale and speed needed to decarbonize the global energy system and mitigate the most severe impacts of climate change.[59] This necessitates an investigation into the barriers hindering a faster and more widespread adoption of solar PV to achieve these critical climate targets.

1.3. Research Questions

- How can we implement different machine learning, deep learning, and hybrid/ensembled models to estimate GSR across the nation?
- How can we incorporate estimated GSR into PV cell/module model to extract PV cell/module parameters?
- How to evaluate the effects of optimum tilt angle and different tracking mechanisms on PV module performance?

1.4. General and Specific Objectives of the Study

General Objective:

- To assess solar energy using data-driven and physical models: application for crystalline silicon photovoltaic systems in Ethiopia

Specific Objectives:

- To estimate GSR nationwide by using diverse ML models for improved PV assessment.

- To study the spatiotemporal variability of solar radiation across the nation.
- To investigate the seasonal and location-dependent variability of c-Si PV cell performance across the nation through a device physics-based assessment.
- To determine the seasonal and site-specific optimal tilt angle for PV modules across the nation.
- To quantify the performance enhancement provided by single-axis and dual-axis tracking mechanisms compared to fixed-horizontal and/or tilt PV module under varying seasonal conditions.
- To develop a comparative analysis of the energy yield and power output for each configuration (horizontal, fixed-tilt, single-axis, and dual-axis tracking) to identify the most effective strategy for maximizing PV module efficiency and energy generation.

1.5. Significance of the Study

The study provides a significant scientific and practical importance, as it addresses a multifaceted challenge in the field of solar energy: the accurate estimation, assessment and optimization of PV system performance on a nationwide scale. By integrating diverse ML models and a hybrid model, this study provides a more robust and precise estimation of GSR. This enhanced GSR dataset will be a crucial input for a wide range of solar energy assessment and applications, from resource mapping to project feasibility studies. Furthermore, the study focusses on the spatiotemporal variability of GSR and its impact on c-Si PV cell performance which is a key for understanding the underlying physics of device operation under real-world conditions. By employing a device physics-based approach, the study insightfully goes beyond empirical correlations to provide a deeper understanding into how factors like solar radiation, temperature, orientation and tracking mechanisms influence PV cell/module efficiency. This fundamental understanding will be invaluable for developing more accurate performance models and improving the design of future PV devices. The investigation into optimal tilt angles and the performance benefits of single - and dual-axis tracking mechanisms provide

actionable insights for practitioners and policymakers. The site-specific and seasonal recommendations for tilt angles will enable a significant increase in energy yield for fixed-tilt installations, while the detailed quantification of performance enhancement from tracking systems will provide a clear cost-benefit analysis for more advanced configurations. The comparative analysis of different PV module configurations (horizontal, fixed-tilt, single-axis, and dual-axis) will serve as a comprehensive guide for selecting the most effective strategy to maximize energy generation and efficiency, thereby accelerating the deployment of solar energy technologies and contributing to national energy security and sustainability goals.

Furthermore, this study probes into the device physics of crystalline silicon (c-Si) solar cells, aligning with the global scientific community's concerted efforts to harness solar energy for electricity generation. The research contributes directly to the urgent transition towards zero-carbon energy, a critical step required to mitigate the dangerous impacts of climate change.

1.6. Dissertation Structure

Chapter 2: Discusses the need for renewable energy, PV energy assessment across the world, renewable energy distribution in Ethiopia, and factors that affect PV cell/module performance. It should also explore the different modeling approaches, including empirical, physical, and data-driven methods like machine learning and deep learning, that have been employed to predict solar radiation and PV performance.

Chapter 3: Introduce the study area, Ethiopia, and describe the ground-based observational and satellite data used in the research. It should also outline the pre-processing and post-processing techniques applied to integrate the data and models. The chapter should present the various POA irradiance models, PV cell models, tilt angles, and tracking mechanisms considered for optimizing PV performance.

Chapter 4: Presents the performance of different machine learning and deep learning models in predicting the spatiotemporal variation of solar radiation across the nation. It should present key PV cell/module parameters such as reverse saturation current density (J_o), short circuit current density (J_{sc}), open circuit voltage (V_{oc}), fill factor (FF), and efficiency (η). Additionally, the chapter should evaluate the optimal tilt angle of PV modules using five decomposition and six transposition models with thirty independent different combinations and various tracking mechanisms (dual/full-axis, vertical-axis, east-west/incline east-west, and north-south) to assess PV module performance across Ethiopia.

Chapter 5: Summarize the key findings of the research, draw conclusions based on the results, and provide recommendations for future research directions.

Chapter 2

2. Literature Review

Energy, a fundamental cornerstone of human civilization, has witnessed a dramatic rush in demand since the Industrial Revolution.[60] This rising consumption is primarily powered by population growth and technological advancements. Developing nations, such as China and India, have emerged as significant contributors to this rising trend.[61] As depicted in Figure 2-1, the historical trajectory and future perspective of world population and energy consumption reveal a clear correlation. To meet this growing energy demand, humanity has primarily relied on two broad categories of energy sources such as conventional (non-renewable) and non-conventional (renewable).

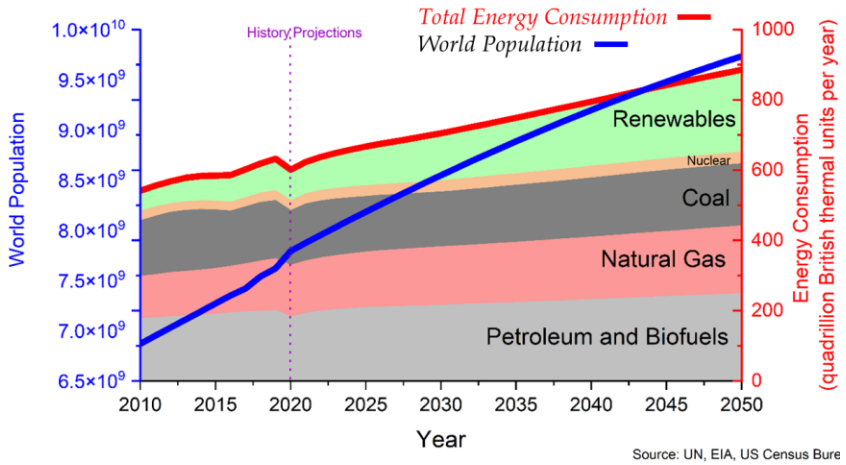

Figure 2-1: World population and energy consumption: A historical overview and future projections.

Conventional fossil fuels, such as oil, coal, and natural gas, account for 81.5-82% of global energy consumption, with oil being the primary source, followed by coal and natural gas (IEA: 2024).[62] Despite their prevalent utilization, they face critical limitations as illustrated in Figure 2-2. These resources are inherently finite and geographically concentrated, leading to geopolitical vulnerabilities. Furthermore, their extraction,

transportation, and combustion processes are substantial contributors to environmental degradation (see Figure 2-2a). As Kelvin *et al.*, highlighted, the reliance on fossil fuels accounts for approximately 75% of global greenhouse gas emissions and a staggering 90% of carbon dioxide (CO_2) emissions.[63] Consequently, the heavy dependence on these energy sources has driven a significant increase in per capita CO_2 emissions, as visually represented in Figure 2-2b. This rising trend underscores the urgent need to transition towards more sustainable energy alternatives, such as renewable energy sources, to mitigate environmental pollution and climate change.

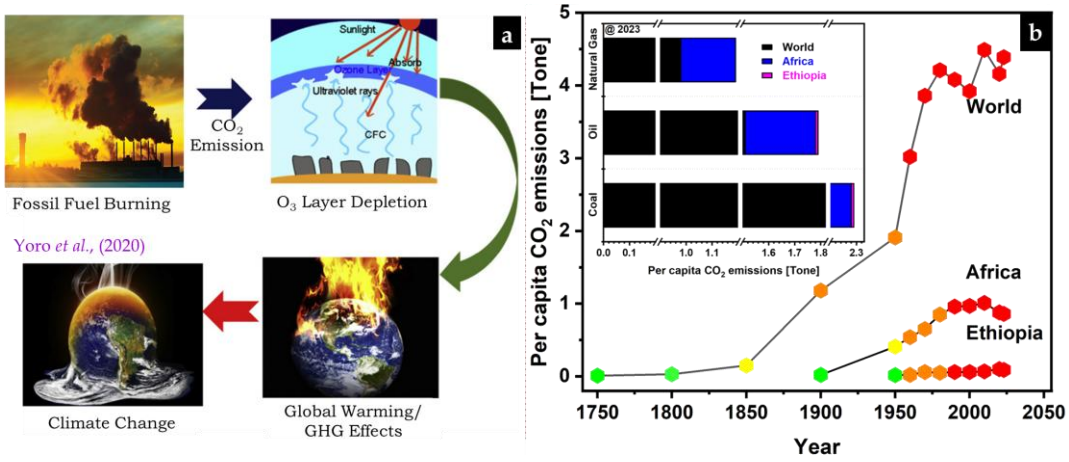

Figure 2-2: Effect of using conventional energy sources on climate change (a) and CO_2 emission by type (World, Africa, Ethiopia: adopted from Kelvin et al., and H. Ritchie et al., 2024) (b).

On the other hand, the renewable energy sources, particularly solar power, are widely accessible, non-polluting, and have a minimal environmental impact, making them ideal for sustainable energy generation as presented in Figure 2-3. For example, the observation from Figure 2-3a, indicating a consistent rise in per capita renewable energy utilization globally and across Africa, suggests a growing global commitment towards transitioning to cleaner energy sources and a recognition of the need to decouple energy consumption from fossil fuels.[64] This trend likely reflects increasing awareness of climate change impacts, advancements in renewable energy technologies making them more

cost-competitive, and supportive policies and investments aimed at fostering sustainable energy development. Furthermore, according to the (IEA, 2024) assessment, Ethiopia's energy sector exhibits a near-complete reliance on renewable resources, with hydroelectric power constituting the overwhelming majority of its energy generation (i.e., ~ >78%: World renewable energy and ~ > 95%: Ethiopia total energy) as presented in Figure 2-3b. This signifies a notable achievement in leveraging indigenous renewable resources for national energy needs.

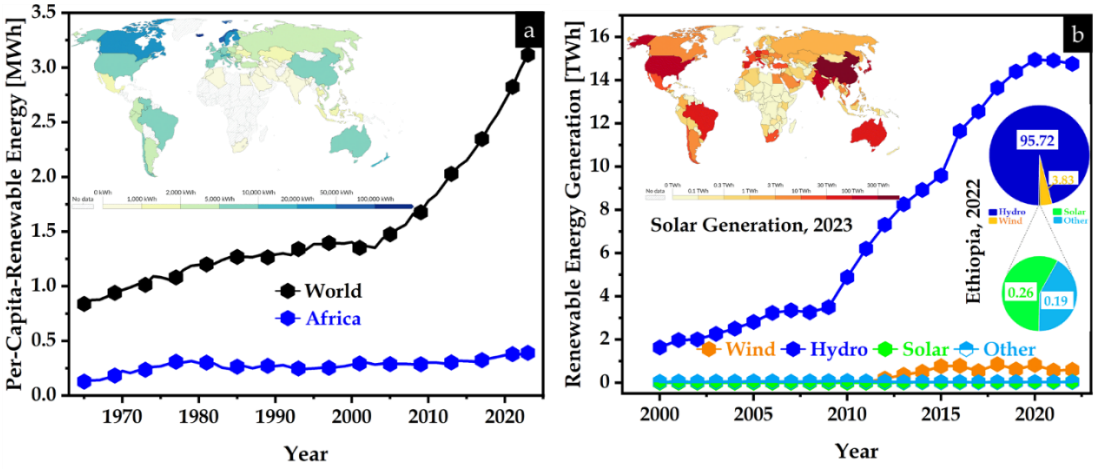

Figure 2-3: Per-capita consumption of renewable energy: World, and Africa (a), Ethiopia (b), (H. Ritchie et al., 2024).

However, while hydropower demonstrates a strong commitment to clean energy within the power sector, its substantial reliance on a single renewable resource, such as water, introduces vulnerabilities linked to climate variability, notably droughts impacting water levels. This necessitates energy system diversification to strengthen resilience and effectively meet escalating energy demands across sectors beyond just electricity generation. Not only this, hydropower development faces critical limitations, including significant environmental consequences stemming from dam construction and altered river ecosystems, susceptibility to climate fluctuations affecting water availability ("*Dams are Drying*": by Professor P. L. O. Lumumba), high initial capital investment as exemplified by projects like the Grand Ethiopian Renaissance Dam (GERD), geographical

constraints due to the limited availability of suitable locations with sufficient water flow and topography, adverse impacts on local communities through displacement and altered livelihoods, and its inherently centralized nature which can pose challenges for widespread and decentralized energy access.

In contrast, over 1.3 kW/m^2 of solar energy is delivered to the atmosphere by our primary source, the Sun.[65] Approximately 1.8 × 10^{11} megawatts (MW) of solar energy are absorbed globally, which is sufficient to meet the world's current power demands.[66,67] The IEA predicts that solar PV could contribute 11% of global green energy, reducing CO_2 emissions by 2.3 gigatons annually.[68] The International Renewable Energy Agency (IRENA) also forecasted that the global solar energy generation capacity will increase by 8,519 gigawatts (GW) by 2050.[69] Figure 2-5 shows a significant increase in solar energy generation capacity over the past decade and the future projections.

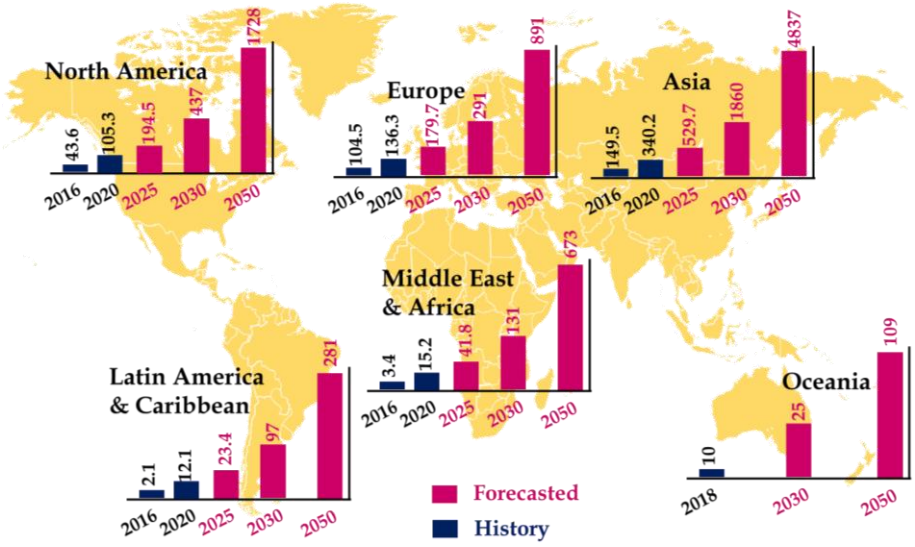

Figure 2-4: A regional breakdown of globally installed PV capacity [in GW]; (Source: IRENA).

Consequently, the cumulative installed capacity of solar photovoltaic (PV) systems worldwide has experienced a remarkable surge in recent years, surpassing the 1 terawatt (TW) milestone in 2022. China, the United States, and India have emerged as the

accredited leaders in solar PV deployment, collectively accounting for most of the world's total installed capacity as reported by IEA-PVPS.[70] China's dominance is particularly noteworthy, with its capacity exceeding that of the world combined. Figure 2-6 graphically depicts the escalating global solar PV capacity trend from 2005 to 2022 [in GW]. The steep upward trajectory clearly illustrates the accelerating adoption of solar energy as a clean and renewable energy source. This rapid expansion underscores the increasing recognition of solar PV as a viable and cost-effective solution to address both energy security and climate change challenges.

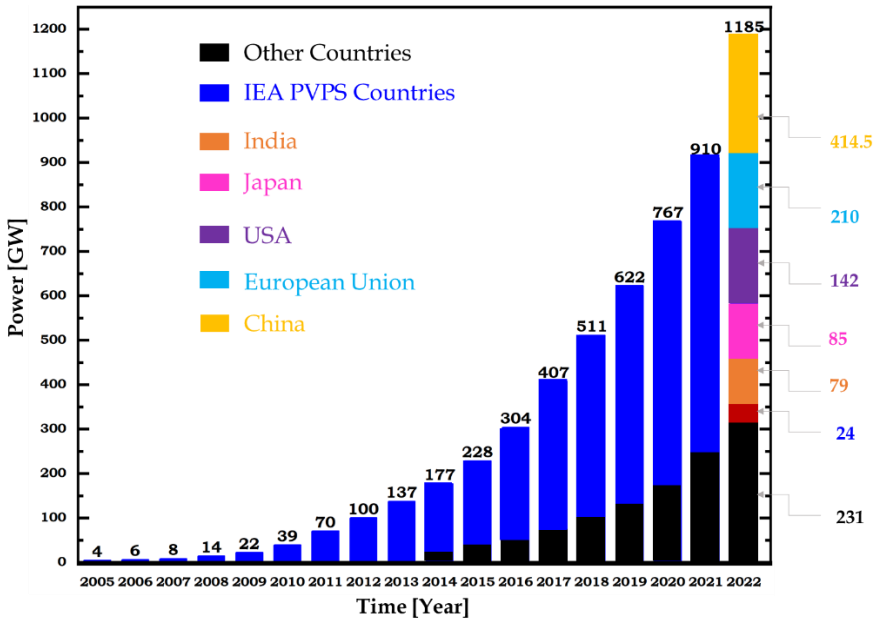

Figure 2-5: Cumulative installed capacity of most leading countries (source: IEA PVPS).

On the other hand, Africa, endowed with abundant solar resources ('the sun continent'), has traditionally relied heavily on fossil fuels for energy. Despite receiving an average annual solar irradiation exceeding 2,119 kWh/m² in many regions, translating to a substantial theoretical solar energy reserve (nearly 40% of the global total), solar power adoption remains limited (report by IRENA).

2.1. Solar Potential in Africa

Africa, particularly North and South Africa, possesses significant solar energy potential due to their equatorial location and high solar irradiation levels, as evidenced by IRENA.[71] Figure 2-7 demonstrates substantial PV solar power potential across the continent. Notably, South Africa exhibits considerable capacity for both Concentrating Solar Power (CSP) and PV solar power, estimated at 43,275 TWh/year and 42,243 TWh/year, respectively.[72] With over 2,500 annual sunshine hours and an average solar irradiation of 220 W/m², South Africa presents favorable conditions for solar energy development. Similarly, North Africa's Sunbelt region, encompassing countries like Algeria, Morocco, Egypt, and Tunisia, receives high levels of annual solar irradiance (2,700, 2,600, 2,800, and 2,300 kWh/m², respectively).[73] Notably, a solar farm occupying a mere 0.3% of Africa's land area could potentially meet the entire electricity demand of the European Union.[74] Despite these abundant resources, many African nations, particularly in sub-Saharan Africa (like Ethiopia), face challenges such as limited financing, high initial costs, low electricity tariffs, inadequate grid infrastructure, regulatory barriers, and a shortage of skilled personnel that hinder their widespread deployment and fully harnessing their solar energy potential.[75]

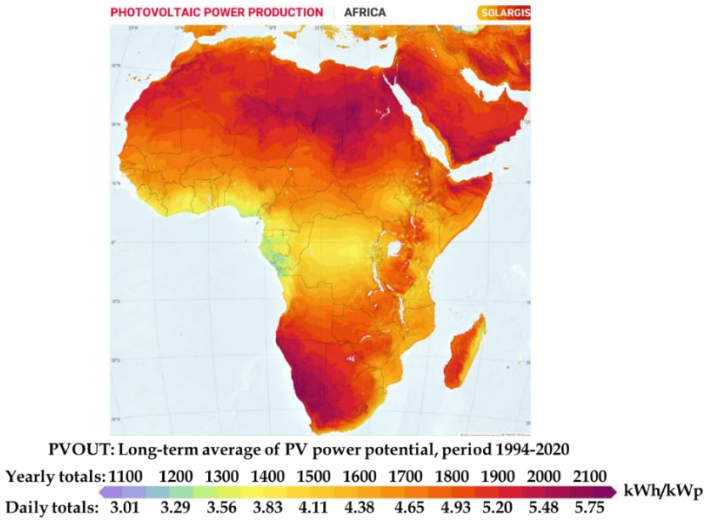

Figure 2-6: Spatial distribution of PV power potential across Africa (Source: Solar Atlas).

2.2. Factors that Affect Solar Energy Harvesting

Even though solar PV energy offers a sustainable alternative to fossil fuels, it faces the challenge of low efficiency. Granting theoretically achievable at 29%, the actual maximum efficiency of commercial PV panels is currently 26%.[76] Several external and internal factors contribute to the degradation of PV cell/module efficiency as presented in Figure 2-8. While advancements have been made in PV construction and installation, environmental factors remain a significant obstacle to overcome.[77]

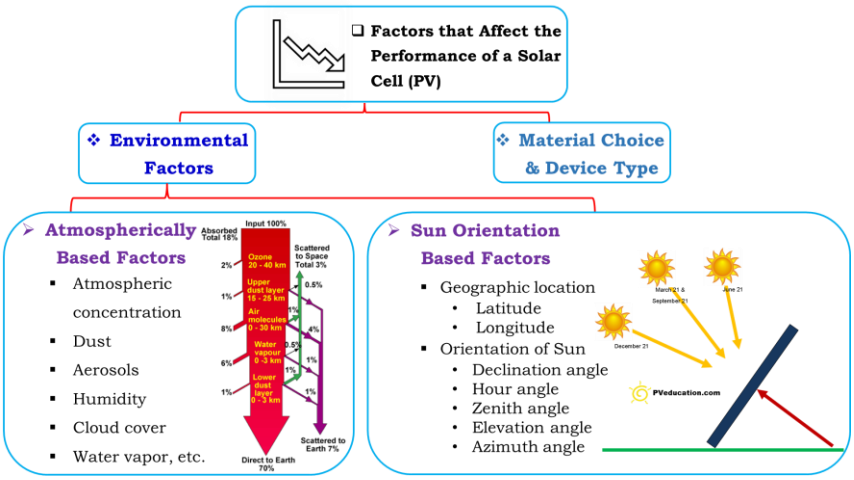

Figure 2-7: Factors that affect PV cell/module performance.

The PV modules/panels heat up when exposed to the sun, and the amount of light absorbed by non-solar cell parts contributes to this heating. This heating decreases bandgap energy and results in poor power output. Solar modules/panels are mounted at a certain height to escape excess heat energy.[78] Adding ventilation, fans, winds, or cooling systems can increase PV module/panel output power by assisting air movement around the panels.[79] While wind can cool the PV panel, it also carries dust and sand particles, reducing PV power output. Therefore, operational and maintenance works are required to mitigate the negative environmental effects in some cases. As a result, a detailed analysis incorporating all environmental, operational, and maintenance factors

and their corresponding effects is necessary to increase PV performance. Figure 2-9 illustrates the effect of environmental factors on current-voltage (I-V) curve of PV cell/modules.

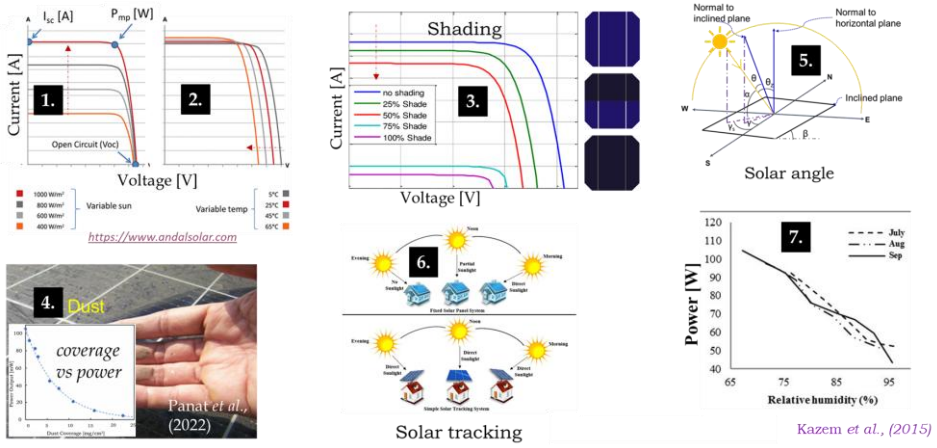

Figure 2-8: Environmental factors on current-voltage (I-V) PV cell/module; 1) solar radiaition, 2) temperature, 3) shadig, 4) dust, 5) solar angle or orientation, 6) solar tracking, and 7) relative humidity.

2.3. Solar Radiation Estimation

Solar radiation, a crucial component of Earth's energy balance, is pivotal in various fields, from renewable energy to agriculture.[80] Countries with high solar energy potential, such as those in Africa, Australia, South America, Southern Europe, and Asia, have witnessed likely they seem have a substantial economic and environmental gains from large-scale solar energy adoption.[81] These benefits have urged increased investment in solar power plants, leading to a growing share of solar energy in national electricity production. The distribution of global horizontal irradiance worldwide is illustrated in Figure 2-10.

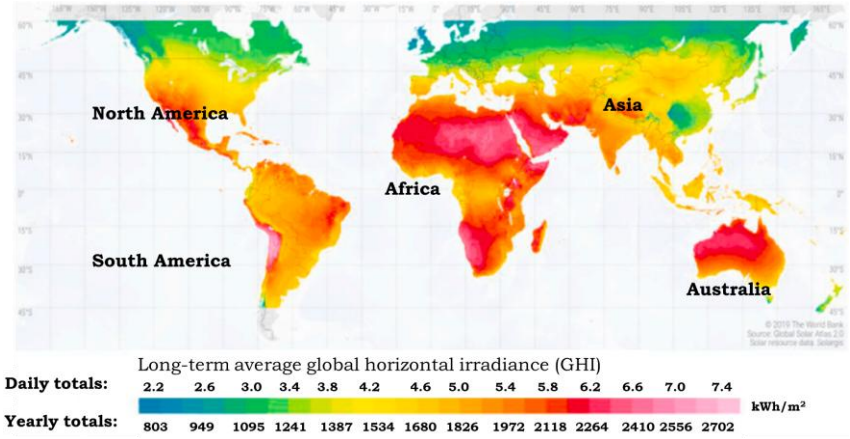

Figure 2-9: The global horizontal irradiance (GHI) worldwide, [source: solar atlas].

However, its accurate measurement and prediction pose significant challenges due to atmospheric conditions, cloud cover, and the high cost of traditional measurement devices. Figure 2-11 illustrates the various factors that influence the amount of solar radiation reaching the Earth's surface.

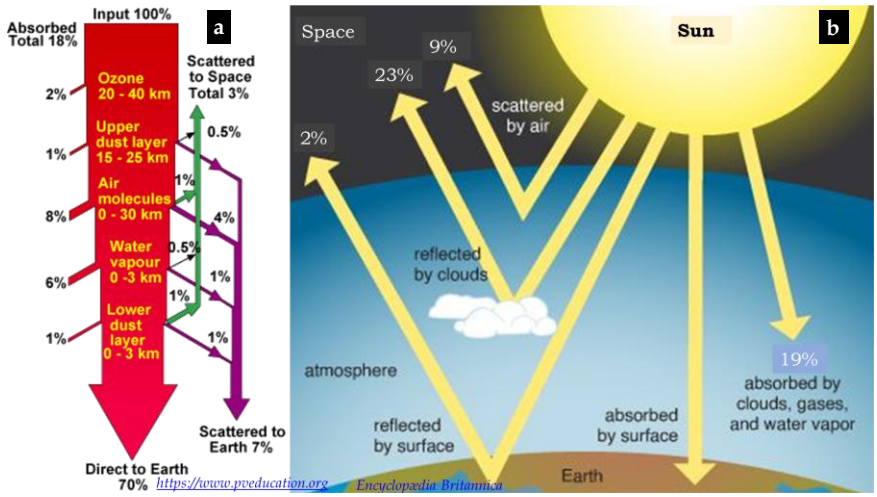

Figure 2-10: Illustrates the interaction of incident solar radiation with the Earth's atmosphere under clear (a) and cloudy (b) conditions; [source: Pv-education and Encyclopædia Britannica].

Despite the importance of solar radiation data for effective solar energy planning, the scarcity of measurements due to the high cost and maintenance of devices like

pyranometers, pyrheliometers, and solar meters hinders accurate solar energy potential estimation and assessments.[82,83] Figure 2-12 illustrates the pyranometers, pyrheliometers, devices, and their underlying principles.

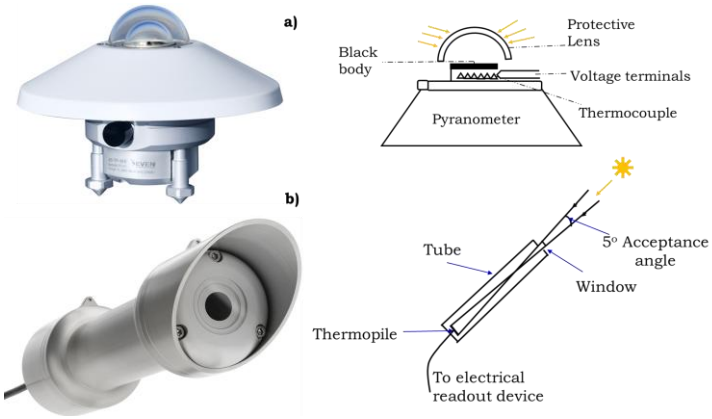

Figure 2-11: Solar irradiance measurement devices: pyranometer (a), and pyrheliometer (b).

To overcome these challenges, AI-based approaches, including machine learning (ML) and hybrid models, offer a promising solution by effectively handling incomplete data, learning complex relationships between solar radiation and various factors, and adapting to changing conditions.[84] These advantages make AI particularly suitable for regions with limited measurement infrastructure, such as Ethiopia, enabling improved understanding of solar energy resources and optimizing renewable energy systems.[85,86,87]

2.3.1. Machine Learning (ML) and Deep Learning (DL) Models

The rapid advancement of computer science, particularly AI, has revolutionized human life by enhancing efficiency and convenience.[88] AI, encompassing ML and DL, empowers systems to compete with human intelligence, learn from data (i.e., supervised learning), and adapt dynamically. Unlike traditional methods, AI excels in handling uncertainty and responding quickly to unforeseen events, making it vital in today's complex world.[89] The fundamental differences between AI, ML, DL, and the basic working principles of ML and DL are illustrated in Figure 2-13.

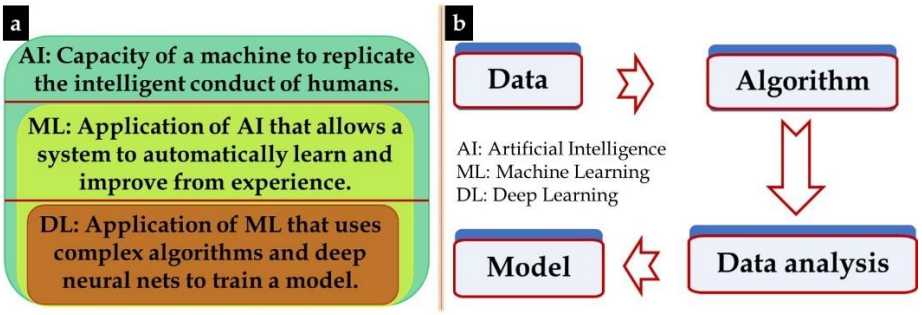

Figure 2-12: Components of AI algorithms, encompassing ML and DL (a), basic operational principles of ML and DL algorithms (b).

2.3.2. Stacked/Ensemble Model

Predicting solar radiation accurately is challenging due to the variability of atmospheric conditions and the dynamic nature of solar radiation itself. While single/separate methods like empirical, separate ML or DL, and time series models have limitations, hybrid/ensemble/stacked models, combining the strengths of multiple approaches, have shown significant promise in enhancing prediction accuracy.[90,91] Examples include the RFs-FFA, which optimizes random forests using the firefly algorithm, and the ANN/SA, which employs simulated annealing to improve neural network performance.[92] Numerous studies have explored using nature-inspired metaheuristic algorithms (e.g., firefly, cuckoo search, genetic algorithms) to optimize prediction structures and network parameters. Other hybrid approaches, such as the SOM-SVR-PSO, combine data pre-processing techniques (like SOM: self-organizing maps clustering) with prediction models (like SVR: support vector regression) and optimization algorithms (like PSO: particle swarm optimization) to effectively handle the diverse characteristics of solar radiation data.[93] These ensemble methods demonstrate the potential to overcome the complexities of solar radiation prediction and achieve higher accuracy levels. Figure 2-14 illustrates the basic framework of the

stacked/ensemble model. This estimated solar radiation is global solar radiation from any surface, to determine amount of solar radiation on a tilted surface we incorporated different plain of array irradiance models.

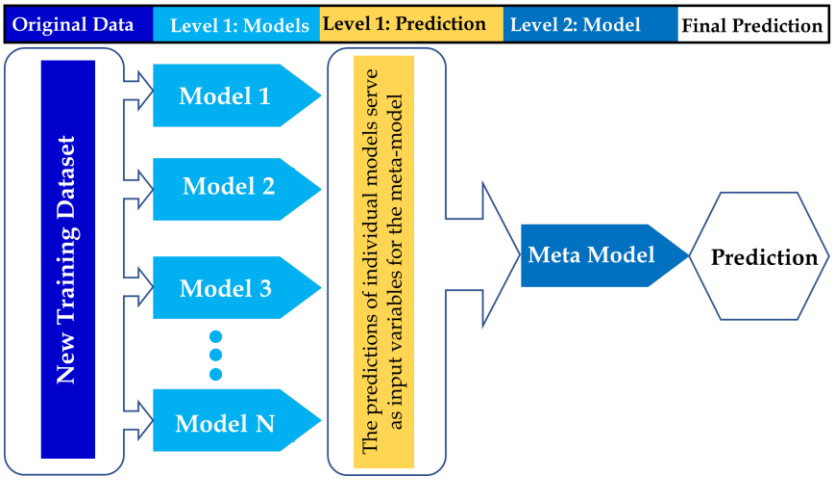

Figure 2-13: The schematic framework of the stacked/ensembled model.

2.4. Solar Radiation on Tilted Surface

The amount of solar radiation on a tilted surface is referred to as a plane of array (POA) irradiance. It's a key factor in determining the energy output of a photovoltaic (PV) system. POA irradiance is affected by the sun's position, the panel's orientation (tilt and azimuth), and the amount of direct, diffuse, and reflected sunlight. Accurately estimating POA irradiance is crucial for predicting PV power output. This typically involves a two-stage process. First, decomposition models separate Global Solar/Horizontal Radiation/Irradiance (GSR/GHI) into Direct Normal Irradiance (DNI) and Diffuse Horizontal Irradiance (DHI).[94] Subsequently, transposition models convert these components into POA irradiance. While established models exist, research continues to refine combined approaches for improved accuracy of these transposition models. However, a universally accepted standard for GSR-to-POA irradiance conversion remains elusive.[95] Studies comparing various model combinations, such as Pelland *et al.*, who examined 12 combinations, have shown that the choice of specific models may have

a limited impact on overall PV power estimation accuracy.[96] Figure 2-15 illustrates different compositions and components of solar irradiance and POA irradiance on PV modules.

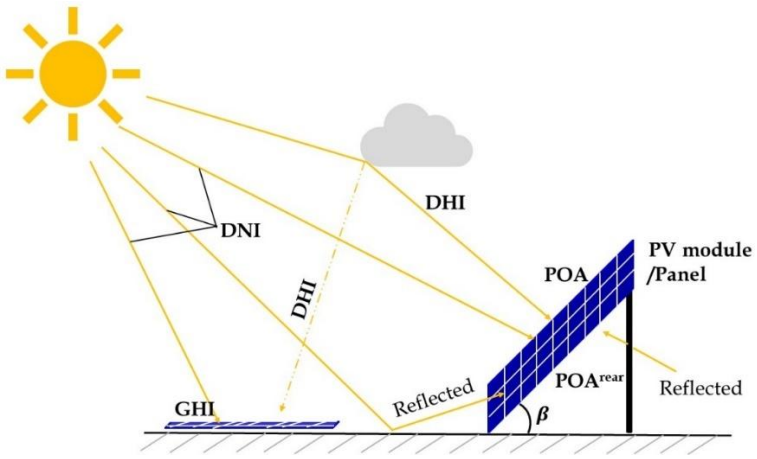

Figure 2-14: Components of POA irradiance impinging upon PV modules.[44]

2.5. Solar Radiation Maximization: Tilt Angle and Tracking Model

Maximizing solar energy capture hinges on optimizing solar module tilt angles. While latitude-based rules of thumb offer initial guidance, they often lack precision for specific locations due to variations in solar radiation influenced by elevation, longitude, and local conditions, particularly for low latitude regions.[97] To accurately determine optimal tilt angles, site-specific solar radiation data analysis is crucial. On the other hand, solar tracking systems, which dynamically adjust panel orientation to follow the sun's path, significantly enhance energy capture compared to fixed-tilt systems.[98] These systems are classified into single-axis tracking (SAT) and dual-axis tracking (DAT).[99] SAT configurations include north-south[100], east-west[101], vertical[102], and inclined east-west axis tracking[103]. Figure 2-16 illustrates schematic diagrams of these configurations, while Table 2-1 provides solar angle parameters for each mechanism.

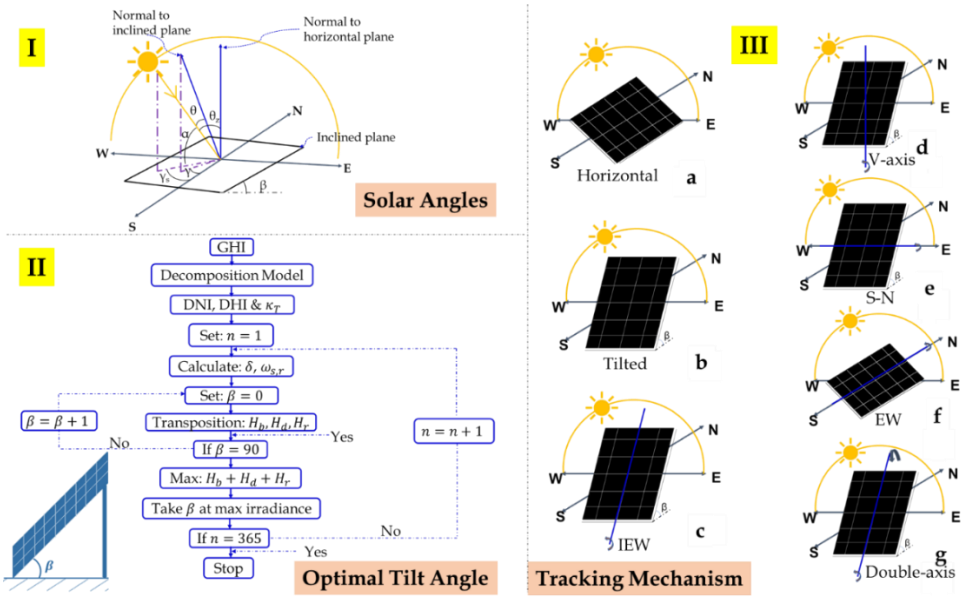

Figure 2-15: Basic solar angle (I), optimal tilt angle (II), and different tracking mechanisms (III).

Table 2-1: Equations of solar angle parameters that are implemented for different tracking mechanisms.[104]

Dual tracker	Vertical-axis tracker	EW/IEW tracker	NS tracker
$\theta = 0,$	$\theta = \theta_z - \beta_{Opt},$	$s_x = \cos\delta\cos\omega\cos(\phi - \beta) + \sin\delta\sin(\phi - \beta),$	$\gamma = \tan^{-1}(\tan\theta_z\cos\gamma_s),$ $\theta = \cos^{-1}(\sin\theta_z\cos\gamma_s\sin\gamma + \cos\theta_z\cos\gamma),$
$\beta = \theta_z,$	$\beta = \beta_{Opt},$	$s_y = -\cos(\delta)\sin(\omega),$ $\theta = \cos^{-1}\left(\sqrt{s_x^2 + s_y^2}\right),$	
$\gamma = \gamma_s,$	$\gamma = \gamma_s,$	$\beta = \cos^{-1}\left(\frac{s_x\cos(\beta)}{\sqrt{s_x^2+s_y^2}}\right),$	$\beta = \gamma,$

2.6. PV Cell Model

The solar cell is a building block representing the performance of a PV power system. Developing a precise solar cell power estimation model is critical for evaluating numerous crucial aspects of a PV system. In PV cells, incident light with photon energies exceeding the material's band gap (E_g) is absorbed, creating electron-hole pairs. These free carriers migrate to opposite electrodes (electrons to negative, holes to positive, implying electric field generation), generating an electric current (see Figure 1-1). Figure 2-17 displays the equivalent circuit diagram for a single diode solar cell, and its I-V characteristic described in equation (2.1).

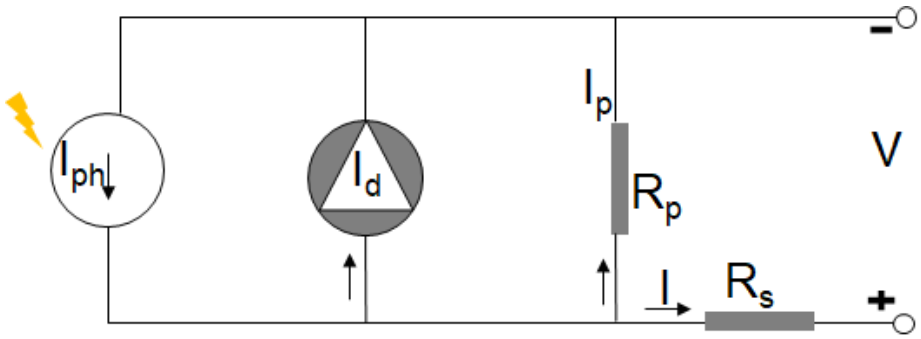

Figure 2-16: Equivalent circuit diagram of single diode solar cell.

$$I = I_{ph} - I_0 \left\{ \exp\left[\frac{q(V+IR_s)}{fkT_a}\right] - 1 \right\} - \frac{V+IR_s}{R_p}. \qquad 2.1$$

Here, the effect of temperature on the energy band gap of semiconductor material is described as follows:[105]

$$E_g(T) = E_g(0) - \frac{\alpha T^2}{(T+\beta)}, \qquad 2.2$$

where, $E_g(T)$ is the band gap of the semiconductor at temperature T (K), $E_g(0)$ at 0 K, and α, β are constants.

The exclusive dependence of solar cell temperature on incoming solar irradiance (P_t) and ambient temperature (T_a) is described by:[106]

$$T = T_a + \Gamma \times P_t, \quad 2.3$$

where,

$$\Gamma = \frac{NOCT-20}{800\ (W/m^2)}. \quad 2.4$$

NOCT represents nominal operating temperature (^oC) and the value of Γ is taken to 0.03 $^oC/Wm^{-2}$ as recommended in the literature.

Equation (2.1) describes the single diode behavior with variables representing key electrical characteristics: light-generated current (I_{ph}), reverse saturation current (I_0), ideality factor (f), series resistance (R_s), and parallel resistance (R_p). Due to the intricate relationship between these variables, a simplified approach is required. To address this, the equivalent circuit model is rationalized by introducing a correction coefficient. This coefficient facilitates the estimation of four parameters at specific conditions of cell temperature (T_c) and incident irradiance (P_t). The following related equations provide a detailed explanation of this approach:[107]

$$I_{sc} = I_{scref}\left[1 + l\left(T_c - T_{ref}\right)\right]\frac{P_t}{P_{ref}}, \quad 2.5$$

$$I_{mp} = I_{mpref}\left[1 + l\left(T_c - T_{ref}\right)\right]\frac{P_t}{P_{ref}}, \quad 2.6$$

$$V_{oc} = V_{ocref}\left[1 + m\left(T_c - T_{ref}\right)\right] ln\left[e + y\left(P_t - P_{ref}\right)\right], \quad 2.7$$

$$V_{mp} = V_{mpref}\left[1 + m\left(T_c - T_{ref}\right)\right] ln\left[e + y\left(P_t - P_{ref}\right)\right], \quad 2.8$$

where e is the base of natural logarithms; l, m, and y are the compensation coefficient, $P_{ref}$is the reference irradiance, T_{ref} is the reference temperature,T_c is cell temperature, I_{scref} is the short circuit current at reference condition, I_{mpref} is current at maximum power point, V_{ocref} is the open circuit voltage at reference condition, V_{mpref} is the voltage at the maximum power point. The constants used in equations (2.1-2.8) and their values are listed in the Table 2-2.

Table 2-2: Constants and values of characteristic variables at reference condition[107,108,109].

Variable	Value	Variable	Value	Variable	Value
q	$1.602x10^{-19}$ C	y	0.0005/ (W/m^2)	I_{scref}	6.24 A
k	$1.381x10^{-23}$ J/°K	m	-0.00288/ °C	I_{mpref}	5.83 A
e	2.718	P_{ref}	1000 W/m^2	V_{ocref}	0.682 V
l	0.0025/°C	T_{ref}	25 °C	V_{mpref}	0.574 V
$E_g(0)$	1.1557 eV	a	7.021×10^{-4} (eV/k)	β	1108 K

Another important parameter is reverse saturation current density (J_0), a critical factor influencing temperature-dependent device performance, quantifies minority carrier leakage across the p-n junction under reverse bias. Primarily governing the open-circuit voltage (V_{oc}), J_0 exhibits a strong dependence on the bandgap within the desired range, as predicted by the p-n junction model:[110]

$$J_0 = \chi \exp\left(-\frac{qE_g}{kT}\right), \tag{2.9}$$

where, $\chi = C \times T^3 = 1.5 \times 10^8\ mA/cm^2$.[110]

The theoretical maximum fill factor (*FF*) of an ideal solar cell, absent of resistive losses (ideal solar cell), can be determined using the following equation:[105]

$$F = \frac{v_{oc} - ln(v_{oc} + 0.72)}{v_{oc} + 1}, \tag{2.10}$$

where, $v_{oc} = (V_{oc}/V_{th})$, is normalized V_{oc}, and $V_{th} = kT/q$ is the thermal velocity.

A solar cell's maximum power (P_{mp}) corresponds to the operating point on its current-voltage (I-V) curve where the product of voltage (V) and current (I) reaches its maximum value.[111] This point can be mathematically represented by:

$$P_{mp} = I_{mp} \times V_{mp}. \tag{2.11}$$

Solar cell efficiency (η) is defined as the ratio of the electrical power output of the cell to the power of the incident light. It is typically expressed as a percentage and can be mathematically described by:

$$\eta = \frac{P_{mp}}{P_{ref} \times A} \times 100, \qquad 2.12$$

where, A is the area of solar cells, P_{mp} is the product of I_{mp} and V_{mp} and P_{ref} is the power of the incident light with 1000 W/m^2. The area of typical solar cells is 125 mm^2 or 156 mm^2.[112]

Furthermore, the I-V characteristics of solar cells are significantly influenced by their interconnection. For instance, parallel connections increase the overall current while maintaining a constant voltage, shifting the I-V curve vertically. This results in a higher short-circuit current (I_{sc}) while the open-circuit voltage (V_{oc}) remains relatively unchanged. Conversely, series connections increase the overall voltage while limiting the current, shifting the I-V curve horizontally as illustrated in Figure 2-18. This leads to a higher V_{oc} while the I_{sc} remains relatively constant. Practical applications often employ a combination of series and parallel connections to optimize the voltage and current output for specific system needs.

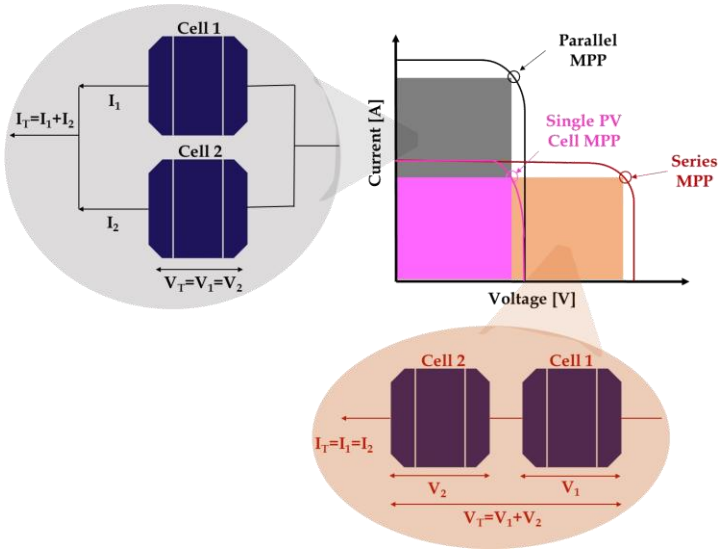

Figure 2-17: The I-V curve of two series and parallel connected PV cells.

Chapter 3

3. Study Area, Data, and Methodology

3.1. Study Area

Ethiopia's intricate topography, encompassing both landforms and inland water bodies, combined with diverse vegetation cover, plays a critical role in shaping its climate. Additionally, large-scale atmospheric and oceanic circulation patterns exert a significant influence. These patterns include the seasonal movement and intensity of semi-permanent subtropical high-pressure systems situated over the Indian and Atlantic Oceans, the Tropical Easterly Jet (TEJ), the low-level Somali Jet, and the Intertropical Convergence Zone (ITCZ). The complex interplay between these local and large-scale factors ultimately determines the weather systems and climatic conditions observed across Ethiopia. Figure 3-1 describes the map of the study area and some of the synoptic weather stations.

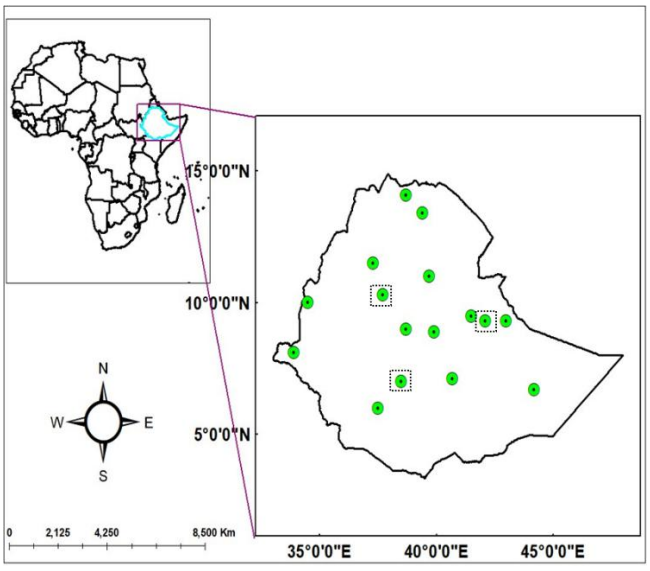

Figure 3-1: The study area with 16 synoptic weather stations (green circled). Stations marked by black dotted squares were withheld from the model development for generality test and represent the Bahir Dar, Arba Minch, and Harar stations.

3.2. Datasets

A three-year high-resolution solar radiation, wind speed, wind direction, and temperature data were acquired from sixteen Ethiopian synoptic stations maintained by the NMI, i.e., from 2020-22. The solar radiation data, collected at 15-minute intervals using Pyranometer SP-Lite and CMP3 instruments, underwent temporal aggregation to the hourly (60-minute) resolution to optimize computational efficiency during model development. Table 3-1 details the geographic coordinates of these instruments for model construction and validation.

Table 3-1: List of synoptic weather stations with geographic coordinates (latitude [Lat., ^{o}N], longitude [Lon., ^{o}E], altitude [Alt., km]) for the data observation period (2020 – 22).

Stations	Lat.	Lon.	Alt.	Stations	Lat.	Lon.	Alt
Addis Ababa	9.0	38.7	2.36	Gambela	8.1	33.9	0.53
Arba Minch	6.0	37.5	1.27	Harar	9.3	42.1	1.89
Methehara	8.9	39.9	0.95	Jijiga	9.3	42.8	1.63
Kebri Dehar	6.7	44.2	1.61	Axum	14.1	38.7	2.13
Bahir Dar	11.5	37.3	1.8	Mekele	13.4	39.4	2.25
Bale Robe	7.1	40.7	2.49	Hawassa	10.0	34.5	1.71
Kombolcha	11.0	39.7	1.84	Asosa	7.0	38.5	1.57
Dabre Markos	10.3	37.7	2.45	Dire Dawa	9.5	42.0	1.28

The dataset was divided into training and testing sets to effectively train and evaluate the model performance. Thirteen stations with substantial data, including 341,440 hourly, 14,227 daily, and 467 monthly data points, were selected for this purpose. Seventy-five percent (i.e., 75%) of this data, comprising 256,080 hourly, 10,670 daily, and 350 monthly data points, was allocated for training the model. The remaining 25%, consisting of 85,360 hourly, 355 daily, and 117 monthly data points, was reserved for testing its performance. To assess the model's generalizability, three stations with distinct climatic conditions were chosen for transferability testing: Bahir Dar (from north,

experiencing temperate mediterranean climate), Arba Minch (from south, experiencing tropical savanna climate), and Harar (from east, experiencing warm semi-arid climate). These stations exhibit significant differences in seasonal climate patterns as illustrated in Figure 3-2 (Koppen climate classification of Ethiopia). By selecting these geographically dispersed stations with distinct climatic characteristics, the model's ability to adapt to varying conditions can be rigorously evaluated.

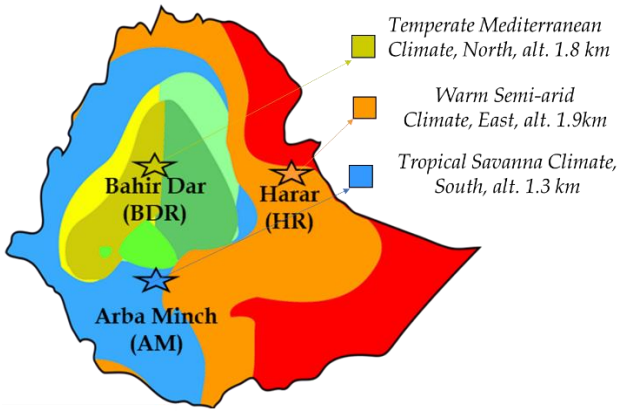

Figure 3-2: Koppen climate classification of Ethiopia [Source: Wikipidia].

Furthermore, we implemented comprehensive data preprocessing techniques to optimize model performance and computational efficiency. This involved normalizing numerical features,[113] imputing missing values using methods like mean/median substitution or KNN imputation[114], and detecting and handling outliers through the interquartile range (IQR) method[115]. Visualizing data distributions using scatter, Taylor, violine, and box plots enabled us to assess data quality and make informed decisions regarding outlier treatment.[116] By addressing these data quality issues, we enhanced model performance and reduced computational costs relatively.

3.3. Global Solar Radiation (GSR) Estimation

Table 3-2 describes the input fields (parameters) for model implementations for estimating global solar radiation (GSR).

Table 3-2: Input fields for the ML algorithm.

Nomenclature	Description and/or Unit	Data Source	Reference
ASSD	All sky surface downward [W/m^2]	NASA Power	117
CSSD	Clear sky surface downward [W/m^2]	>>	>>
AOD	Aerosol optical depth [550nm]	MERRA-2	118
PM	Particulate matter [μm]	>>	>>
Lat	Latitude [^{o}]	NMI	119
Lon	Longitude [^{o}]	>>	>>
Temp	Ambient temperature [^{o}C]	>>	>>
WD	Wind direction [^{o}]	>>	>>
WS	Wind speed [m/s]	>>	>>
Eleva	Elevation [m]	>>	>>
GSR	Global solar radiation [W/m^2]	>>	>>
KT	Clearness index [-]	Calculated	-
Decl	Declination angle [^{o}]	>>	-
SZA	Solar zenith angle [^{o}]	>>	-
Albedo	Surface albedo [-]	>>	-

Figure 3-3 shows the linear correlations among the parameters. The correlation coefficients range from -1 to 1, with -1 indicating a perfect negative correlation, 1 indicating a perfect positive correlation, and 0 indicating no correlation. Based on the correlation Figure 3-3 provided, GSR has a strong positive correlation with the following parameters; ASSD (80%), CSSD (78%), KT (56%), and Temp (51%); weak positive correlation with; WS (10%), Lon (7%), and Eleva (2%); and negative correlation with, Albedo (52%), SZA (32%), PM (16%), AOD (9%), Decl (3%), WD (2%), and Lat (2%).

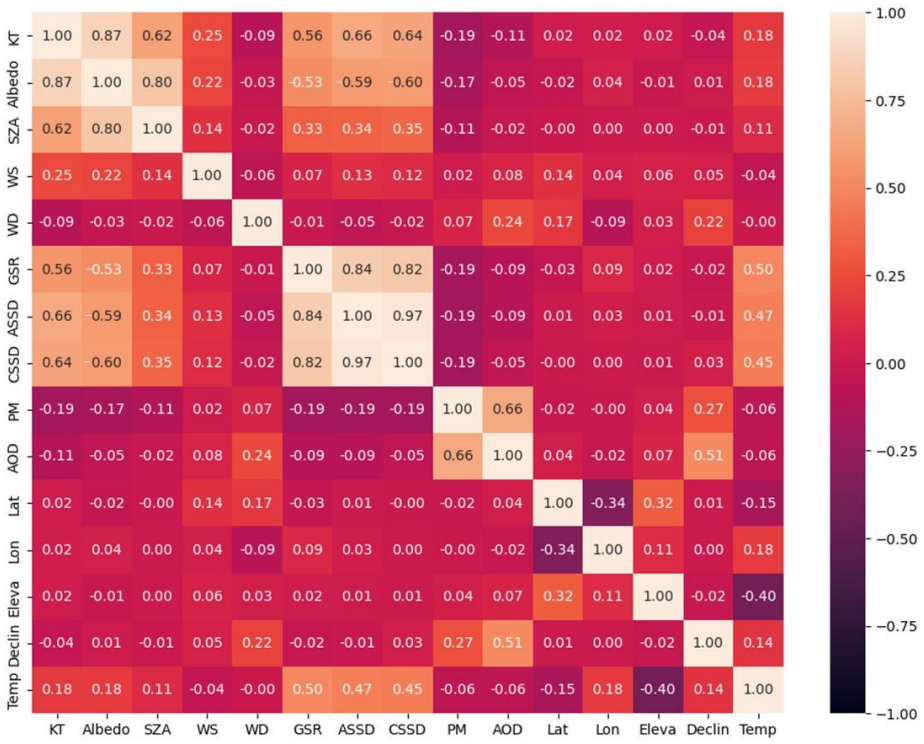

Figure 3-3: Correlation of each input field with the others.

3.3.1. Data Processing and ML Implementation

Data preprocessing, model construction, and model evaluation are key elements of ML experiments. Figure 3-4 illustrates the schematic representation of the basic working principles of ML algorithms.

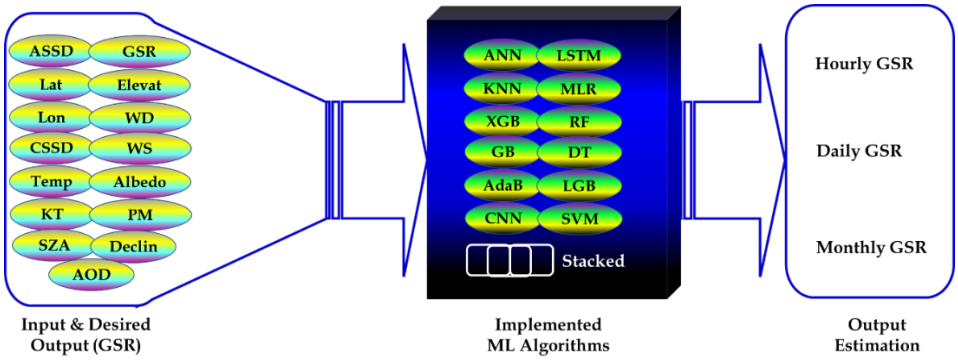

Figure 3-4: Basic principle of a machine learning algorithm.

The four data preparation steps were data quality assurance, dataset splitting, data scaling, and variable selection.[120,121] During the model-building process, the ML algorithm, parameter selection, model construction, and model saving were the main steps.[122] Figure 3-5 provides a visual representation of the data processing flows during model implementation. Model performance skill is assessed using various skill metrics based on the test dataset and the saved model from the model construction step as described from Equation 3.1 to 3.7.

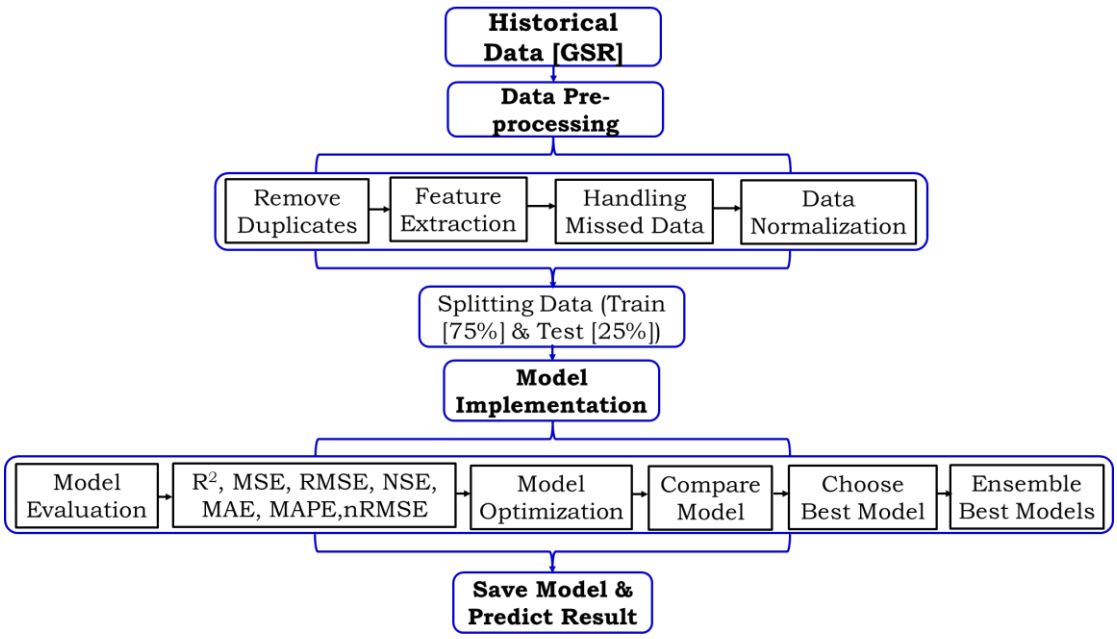

Figure 3-5: Flow chart diagram of data processing and assessing ML models to predict solar radiation.

3.3.2. Stacked (Ensemble) Model Implementation

A stacked ensemble ML model, comprising six base better performing models such as GB, XGB, DT, kNN, RF, and LGB, was utilized to generate high-resolution (1° x 1°) solar radiation data for 2022 across Ethiopia as illustrated in Figure 3-6.

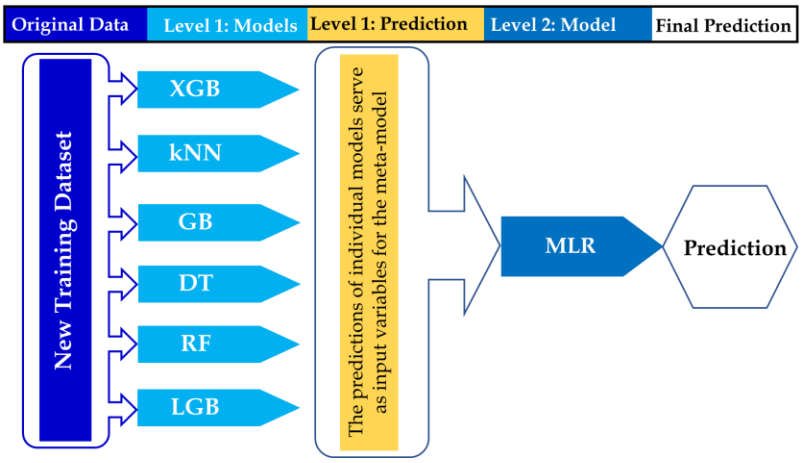

Figure 3-6: The stacked/ensembled model that implemented for this particular study.

The model was trained on observational data acquired from Ethiopia's NMI. The projection of data from observational to estimated (1° x 1°) is presented in Figure 3-7.

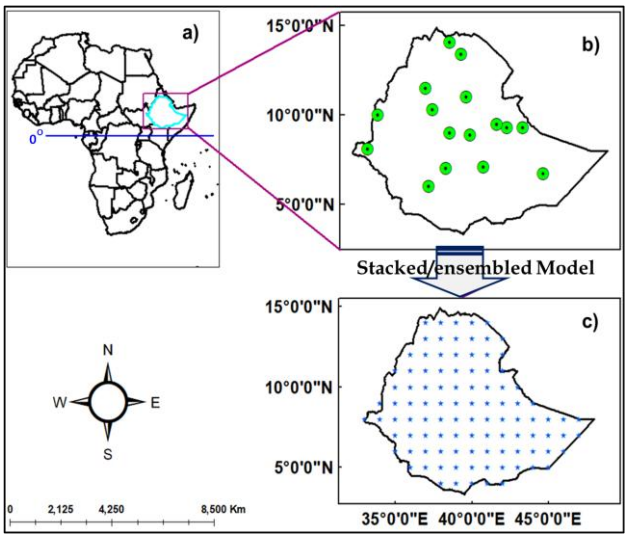

Figure 3-7: Projecting observational data into regular 1-1^{o} by using the stacked model; map of Africa (a), Ethiopia; synoptic weather stations (b), estimated 1° by 1° GSR map (c).

3.3.3. Model Evaluation Metrics

Seven indicators were used to evaluate the model performances; mean absolute error (MAE), mean squared error (MSE), root mean squared error (RMSE), normalized root mean squared error (nRMSE), mean average percentage error (MAPE), Nash-Sutcliffe efficiency (NSE), and R-squared (R^2).

$$MAE = \frac{(\sum_{i=1}^{n}|y_{ai}-y_{pi}|)}{n}, \quad 3.1$$

$$MAPE = \frac{\sum_{i=1}^{n}\left|\frac{y_{ai}-y_{pi}}{y_{ai}}\right|}{n} \times 100, \quad 3.2$$

$$MSE = \frac{\left(\sum_{i=1}^{n}(y_{ai}-y_{pi})^2\right)}{n}, \quad 3.3$$

$$NSE = 1 - \frac{\sum_{i=1}^{n}(y_{ai}-y_{pi})^2}{\sum_{i=1}^{n}(y_{ai}-\overline{y_a})^2}, \quad 3.4$$

$$RMSE = \sqrt{\frac{\left(\sum_{i=1}^{n}(y_{ai}-y_{pi})^2\right)}{n}}, \quad 3.5$$

$$R^2 = \frac{\left(\sum_{i=1}^{n}(y_{ai}-\overline{y_a})(y_{pi}-\overline{y_p})\right)^2}{\sum_{i=1}^{n}(y_{ai}-\overline{y_a})^2 \cdot \sum_{i=1}^{n}(y_{pi}-\overline{y_p})^2}, \quad 3.6$$

$$nRMSE = \frac{RMSE}{y_{a,max}-y_{a,min}}, \quad 3.7$$

where n denotes the number of data points, y_{pi} and y_{ai} stand for predicted and observed global solar radiation, respectively, and $\overline{y_p}$ and $\overline{y_a}$ stand for the average of the results. The observed and predicted values are strongly associated if R^2 is close to 1.

3.4. Plain of Array (POA) Irradiance Estimation

Following the estimation of global solar radiation using a stacked/ensemble modeling approach, we employed five decomposition models (Erbs *et al.*[123], DISC[124], Boland *et al.*[125], Louche *et al.*[126], and Orgill-Holland[127]) and six transposition models; including three isotropic models (Liu and Jordan[128], Badescu[129], and Koronakis[130]) and three anisotropic models (Reindl *et al.*[131], Hay[132], and Steven-Unsworth[133]), which results, thirty different combinations to determine the POA irradiance across the nation. Figure 3-8 visually represents the schematic diagram outlining this process.

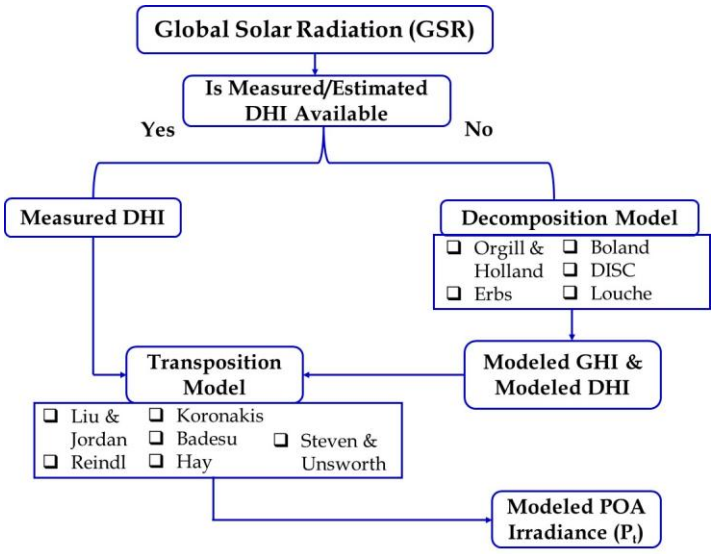

Figure 3-8: Schematic diagram to model POA irradiance.

3.5. PV Cell Parameters

Finally, we successfully integrated POA irradiance data into a PV cell parameter model. This integration enabled the better determination of key PV cell/module parameters, including short-circuit current (I_{sc}), maximum power point current (I_{mp}), short-circuit current density (J_{sc}), open-circuit voltage (V_{oc}), maximum power point voltage (V_{mp}), and others. Figure 3-9 illustrates the schematic diagram outlining the integration process.

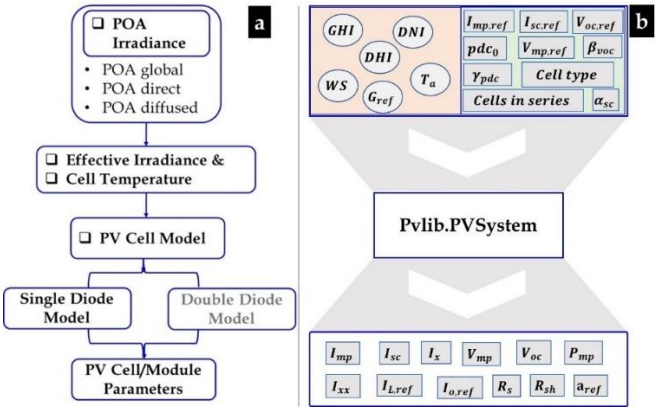

Figure 3-9: Integrating POA irradiance into PV cell (a), and PV module (b) model.

Chapter 4

4. Results and Discussion

Section 4 offers a comprehensive analysis of solar energy potential assessment in Ethiopia. Subsection 4.1 probes into the estimation of global solar radiation (GSR), a crucial factor in solar energy assessment across the nation. By quantifying GSR across the country, this section provides valuable insights for optimizing solar power generation. Subsection 4.2 focuses on the evaluation of single-crystalline silicon photovoltaic (PV) cells performance which is a widely used technology in solar energy conversion. This analysis examines the suitability of these cells for Ethiopia's specific solar conditions, considering factors such as efficiency and performance under diverse climates. Finally, Subsection 4.3 investigates the impact of tilt angles and tracking mechanisms on photovoltaic module performance. By comparing different configurations, this section explores strategies for maximizing solar energy capture and improving system efficiency in Ethiopia's diverse solar environments.

4.1. Estimate Global Solar Radiation (GSR)

Twelve ML models and one stacked/ensembled model were evaluated for their ability to predict global solar radiation at various time scales (hourly, daily, monthly). The models were trained and tested on data from thirteen stations, with 25% reserved for independent testing. Additionally, the transferability and scalability of the top-performing models were assessed using data from three separate stations (i.e., with likely distinct climatic conditions). Feature importance analysis, using a random forest model, revealed that ASSD as the largest contributor to model estimation, followed by Lon., CSSD, Lat., Temp., Eleva., Declin., PM, and AOD. The importance of the input variables as contributor to model prediction of global solar radiation by using a random forest model is illustrated in Figure 4-1.

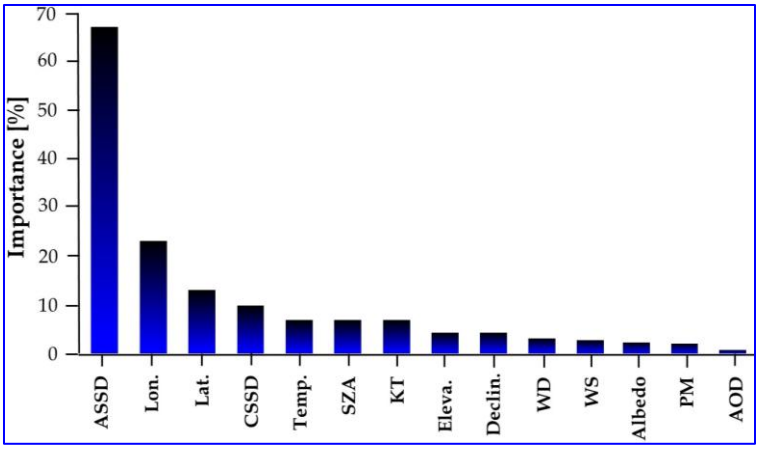

Figure 4-1: Importance of feature variables to estimate GSR (i.e., the contribution of each variable to model estimation).

4.1.1. Predicting Hourly Solar Radiation

Figure 8 illustrates the performance of nine ML algorithms in predicting hourly solar radiation. Statistical metrics revealed promising results for most models. The R^2 values ranged from 0.834 to 0.985, indicating a strong positive correlation between predicted and observed values. However, models like SVM, LSTM, and CNN were excluded due to their lower R^2 (<0.5) and computationally expensive nature. The models, XGB, RF, GB, DT, KNN, and LGB emerged as top performers, achieving high R^2 values of 0.98, 0.98, 0.96, 0.95, 0.97, and 0.96, respectively. Notably, these models demonstrated superior predictive performance while maintaining computational efficiency, making them suitable for relatively small datasets. These findings suggest that tree-based models offer a compelling alternative to computationally intensive neural networks and deep learning models, particularly for datasets of moderate size. Conversely, Ada and MLR displayed the lowest accuracy (R^2 = 0.834 and 0.828, respectively). RMSE served as another performance indicator. All models achieved RMSE values between 33.62 and 115.25 W/m². The top-performing models (XGB, RF, KNN, and LGB) exhibited the lowest RMSEs (XGB = 33.62, RF = 38.54, KNN = 47.44, and LGB = 51.02 W/m²), highlighting

their superior accuracy. Notably, the XGB model achieved the absolute lowest RMSE (33.62 W/m²), solidifying its position as the most accurate predictor. MAE complemented the analysis by measuring the average prediction error. XGB once again emerged as the leader with the smallest MAE value (33.62 W/m²), signifying minimal deviation between predicted and measured values. Conversely, the MLR model displayed the highest MAE (84.93 W/m²), indicating a larger prediction bias. Notably, most other models achieved MAE values below 35 W/m². The details of evaluation metrics are described in Table 3.

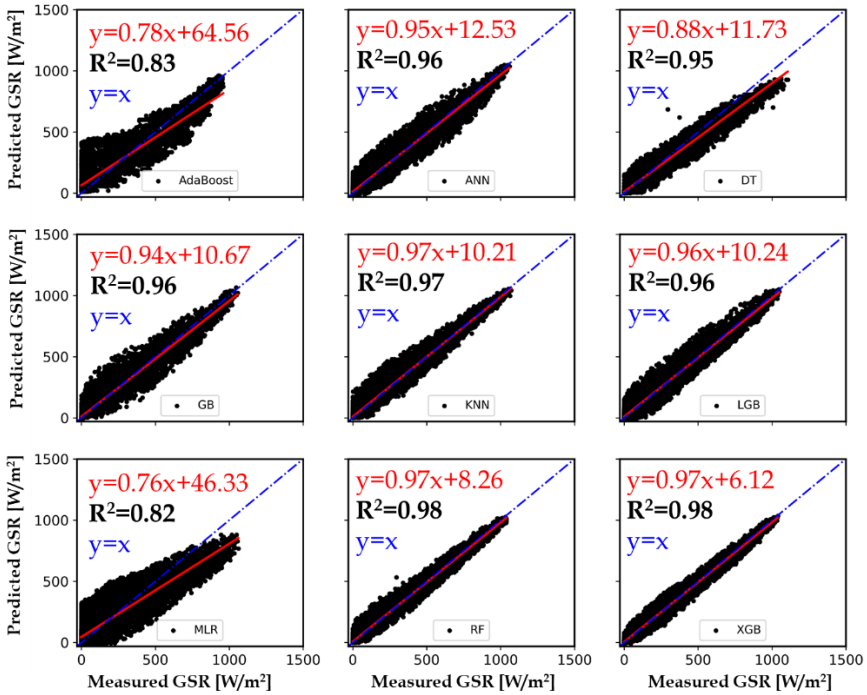

Figure 2: Scatter plots of the cross-validation results for 9 ML models to predict hourly solar radiation.

Table 3: Model evaluation metrics for hourly predicted solar radiation.

ML	*Ada*	*ANN*	*DT*	*GB*	*KNN*	*LGB*	*MLR*	*RF*	*XGB*
MAE	*79.77*	*31.43*	*33.70*	*30.30*	*26.35*	*32.69*	*84.93*	*22.41*	*20.03*
RMSE	*112.4*	*53.66*	*58.27*	*54.92*	*47.44*	*51.02*	*115.2*	*38.54*	*33.62*
nRMSE	*0.11*	*0.05*	*0.06*	*0.05*	*0.04*	*0.05*	*0.11*	*0.03*	*0.03*
NSE	*0.82*	*0.96*	*0.95*	*0.96*	*0.97*	*0.96*	*0.82*	*0.98*	*0.98*

R^2	*0.83*	*0.96*	*0.95*	*0.96*	*0.97*	*0.96*	*0.82*	*0.98*	*0.98*

Figure 9 presents the distribution of variance in hourly deviation probabilities for nine ML models used to predict solar radiation. The error frequency distribution revealed a wide error range, with some models exhibiting errors up to ±200 W/m². In contrast, a six models - KNN, RF, XGB, GB, LGB, and DT demonstrated significantly high accuracy. These models showed a more concentrated error distribution, with approximately 50% of hourly errors centered within a narrow range of ~< ±50 W/m² and a mean close to zero. This concentration indicates the robustness and superior performance of these models for hourly solar radiation estimation. Consequently, these six models were selected as prime base learners for a stacking ensemble, which is expected to exploit their individual strengths and complementary behaviors to achieve more accurate and stable daily and monthly solar radiation estimations than any a single-model approach. . By mitigating the limitations inherent in single-model predictions, the Stacked model is anticipated to enhanced both predictive accuracy and stability. In addition, the mean bias analysis provided further insight into model behavior (Figure 9). For instance, AdaBoosting (Ada) model showed a mean bias of -23.79 W/m², suggesting a consistent over-prediction of hourly solar radiation. In contrast, the DT model, with a mean bias of 9.65 W/m², was the only one among the nine models to consistently under-predict the values. These models indicate relatively higher biases in both Ada and DT model, while the remaining models displayed in intermediate bias levels. The GB model on the other hand, showed a mean bias close to zero, indicating it is a relatively unbiased model for hourly solar radiation estimation.

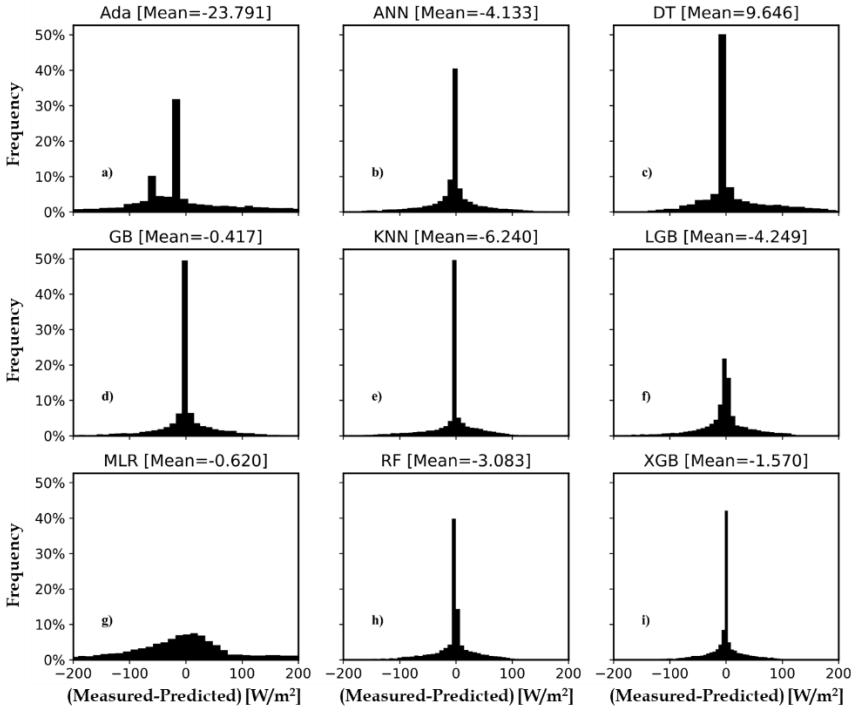

Figure 3: The frequency distribution of hourly solar radiation bias relative to observations from ML models to predict hourly solar radiation.

4.1.2. Predicting Daily Solar Radiation

The analysis in Figure 10 assessed the performance of twelve ML models (i.e., 11 separate and one Stacked models) for predicting daily solar radiation across Ethiopia. Stacked, KNN, GB, RF, and XGB emerged as the most successful models to estimate daily solar radiation. These exhibited high R^2 values (0.935 - 0.963) indicating strong correlations between predicted and observed values. Additionally, they displayed low RMSE (11.784 - 15.645 W/m²) and MAE (9.719 - 13.5 W/m²), signifying minimal prediction errors and bias. Notably, the Stacked model achieved the best overall performance with the highest R^2 (0.963) and the lowest RMSE (11.784 W/m²) and MAE (9.719 W/m²). Conversely, MLR, SVM, and Ada models demonstrated considerably lower performance. These models yielded lower R^2 values (0.687 - 0.724), suggesting weaker correlations between predictions and observations. Furthermore, they exhibited higher RMSE (31.566 - 40.895 W/m²) and MAE (26.343 - 33.500 W/m²), indicating larger

prediction errors and biases. Model performance evaluation metrics for the prediction of daily solar radiation are presented in Table 4.

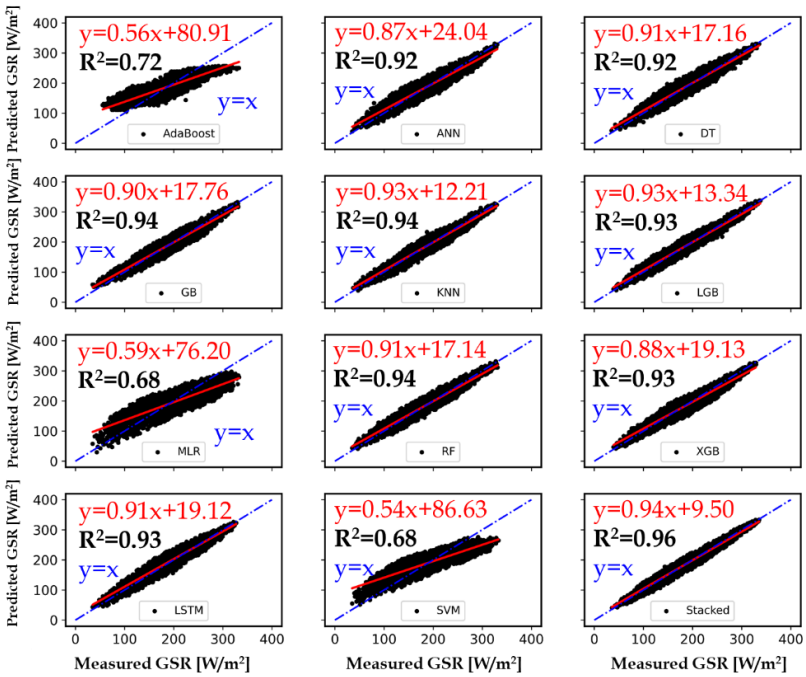

Figure 4: Scatter plots of the cross-validation results for 12 ML models to predict daily solar radiation.

Table 4: Model evaluation metrics for daily predicted solar radiation.

ML	*Ada*	*ANN*	*DT*	*GB*	*KNN*	*LGB*	*MLR*	*RF*	*XGB*	*LSTM*	*CNN*	*SVM*	*Stack*
MAE	*26.34*	*13.92*	*13.07*	*11.80*	*10.85*	*11.09*	*28.27*	*11.96*	*12.79*	*13.14*	*33.50*	*28.02*	*9.71*
RMSE	*31.56*	*17.18*	*16.17*	*14.63*	*13.62*	*13.57*	*34.20*	*14.66*	*15.64*	*16.04*	*40.89*	*33.86*	*11.78*
nRMSE	*0.11*	*0.06*	*0.05*	*0.05*	*0.04*	*0.04*	*0.12*	*0.05*	*0.05*	*0.05*	*0.14*	*0.11*	*0.04*
MAPE	*16.79*	*8.49*	*78.08*	*7.12*	*6.45*	*6.65*	*17.16*	*7.23*	*7.44*	*7.95*	*20.72*	*17.24*	*5.76*
NSE	*0.71*	*0.91*	*0.92*	*0.93*	*0.94*	*0.94*	*0.68*	*0.93*	*0.93*	*0.92*	*0.54*	*0.68*	*0.96*
R^2	*0.72*	*0.92*	*0.93*	*0.94*	*0.95*	*0.93*	*0.68*	*0.94*	*0.93*	*0.93*	*0.58*	*0.68*	*0.96*

Figure 11 illustrates the error distribution of 11 separate and 1 Stacked model for daily solar radiation estimation. As shown , all ML models demonstrated improved accuracy, with error range narrowing to less than ±100 W/m². This reduction in error

variance is attributed to the smoothing effect of averaging hourly data. The best-performing models: the Stacked, KNN, GB, RF, and XGB exhibited particularly tight error distributions falling within ±30 W/m². Among them, the Stacked model showed exceptional performance, with an error distribution of less than ±20 W/m². This confirms that the ensemble approach effectively leverages the complementary nature of its base learners to outperform individual models. While models like MLR, Ada, and SVM exhibited relatively wider error distributions for daily estimation, a mean bias analysis provided further insights. The mean bias values ranged from -3.382 W/m² for the LSTM model to 2.221 W/m² for the XGBoost model. The relatively high mean bias of the LSTM model is likely due to the dataset size and the model's complex architecture, which requires extensive computational resources for optimal performance. The RF, Stacked, ANN, and SVM models were considered relatively unbiased for daily estimation, as their mean bias values were close to zero.

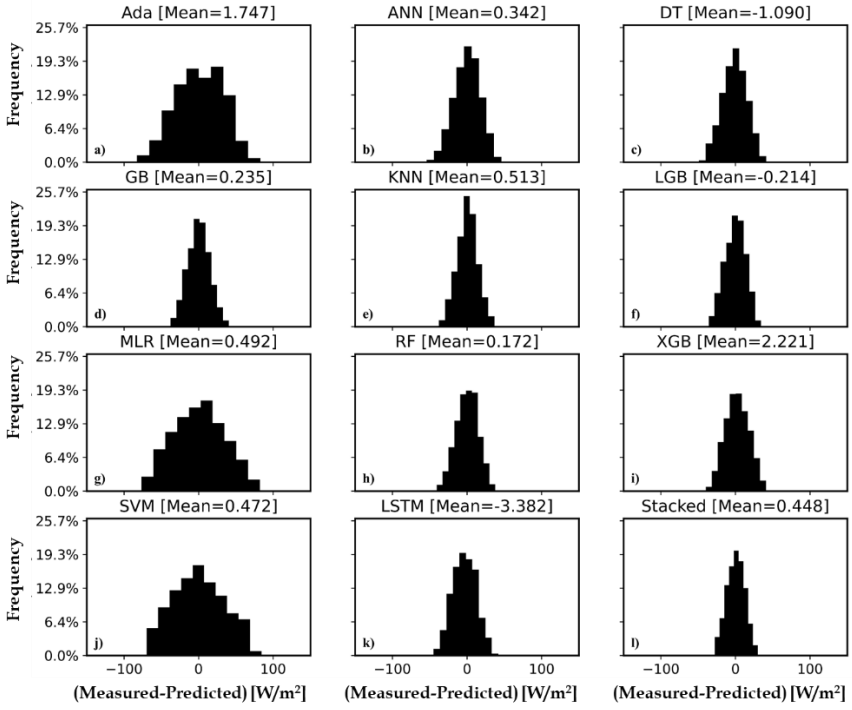

Figure 5: Frequency distribution of daily solar radiation bias relative to observations from 12 ML models to predict daily solar radiation.

4.1.3. Predicting Monthly Solar Radiation

Ten models exhibited impressive R^2 values ranging from 0.770 to 0.956, indicating a strong correlation between monthly predicted and measured values as described in Figure 12. Notably, Stacked, XGB, GB, and RF models emerged as the frontrunners with exceptional R^2 scores of 0.956, 0.946, 0.938, and 0.925, respectively. In contrast, the SVM and LSTM models displayed lower R^2 values of 0.493 and 0.670, respectively, suggesting a weaker association between their predictions and actual measurements. The RMSE values corroborated the R^2 findings. All twelve models exhibited RMSEs between 9.938 and 38.491 W/m². The Stacked, XGB, GB, and RF models maintained their dominance with the lowest RMSEs (Stacked = 9.938 W/m², XGB = 11.034 W/m², GB = 11.962 W/m², and RF = 12.323 W/m²), signifying superior prediction accuracy. Conversely, SVM and LSTM models displayed the highest RMSEs (SVM = 38.491 W/m², and LSTM = 29.745 W/m²), highlighting their limitations in monthly solar radiation prediction. The Stacked model consistently outperformed its counterparts across all evaluation metrics. It achieved the lowest RMSE (9.938 W/m²) and the lowest mean absolute error (MAE) of 8.399 W/m², indicating the most accurate predictions with minimal deviation from actual values. The SVM model exhibited the highest prediction bias, reflected in its significantly higher MAE of 31.393 W/m² compared to other models with MAE values all below 13 W/m². This suggests a systematic over- or underestimation by the SVM model. The summary of model performance evaluation metrics for the prediction of monthly solar radiation is presented in Table 5.

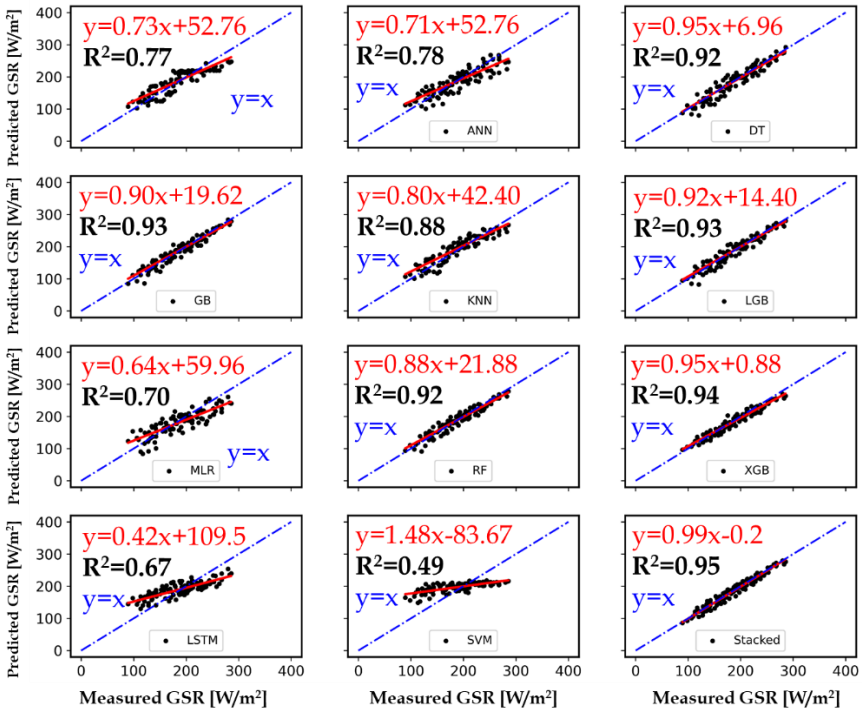

Figure 6: Scatter plots of the cross-validation results for 12 ML models to predict monthly solar radiation.

Table 5: Model evaluation metrics for monthly predicted solar radiation.

ML	*Ada*	*ANN*	*DT*	*GB*	*KNN*	*LGB*	*MLR*	*RF*	*XGB*	*LSTM*	*SVM*	*Stack*
MAE	*19.08*	*17.49*	*12.25*	*9.66*	*14.66*	*10.87*	*21.26*	*10.41*	*8.89*	*25.09*	*31.39*	*8.39*
RMSE	*21.88*	*22.10*	*15.19*	*11.96*	*17.71*	*13.21*	*26.30*	*12.32*	*11.03*	*29.74*	*38.49*	*9.93*
nRMSE	*0.11*	*0.11*	*0.08*	*0.06*	*0.09*	*0.07*	*0.13*	*0.06*	*0.06*	*0.15*	*0.20*	*0.05*
MAPE	*10.50*	*9.84*	*7.18*	*5.69*	*8.53*	*6.39*	*11.84*	*6.01*	*4.86*	*14.78*	*19.15*	*4.80*
NSE	*0.77*	*0.76*	*0.89*	*0.93*	*0.85*	*0.91*	*0.67*	*0.92*	*0.94*	*0.58*	*0.30*	*0.95*
R^2	*0.77*	*0.78*	*0.92*	*0.93*	*0.88*	*0.93*	*0.70*	*0.92*	*0.94*	*0.67*	*0.49*	*0.95*

The error distribution for all models used to estimate monthly solar radiation is illustrated in Figure 13. Except for the Stacked, RF, GB, and XGB models, all models displayed a relatively broad error distribution, which suggests that data size significantly influences their performance in monthly solar radiation estimation. Despite the decreasing data size from hourly to daily and then monthly, the Stacked model

consistently outperformed the individual models, with an error variance ranging from approximately < ±20 W/m². Moreover, among all evaluated models, the Stacked model exhibited the lowest bias (1.185 W/m²) in predicting monthly average global solar radiation. Conversely, SVM (-8.005 W/m²) and LSTM (6.492 W/m²) displayed the highest deviations. Interestingly, while Ada, GB, LSTM, SVM, and KNN models exhibited negative biases, the majority displayed positive biases compared to the daily prediction mean bias. The maximum positive/negative bias with significant frequency was ±50 W/m². Stacked, XGB, GB, and RF models demonstrated superior skill in compete with observed monthly mean solar radiation. Notably, XGB emerged as the fastest model with excellent prediction accuracy for all time scale data sets. GB, RF, LGB, DT, and other models were also computationally efficient. However, Stacked, neural network based models (like ANN, LSTM, and CNN) and SVR models exhibited the longest training times, especially with increasing data size. Furthermore, Stacked, XGB and GB models displayed strong generalization capabilities, mitigating overfitting concerns. This is particularly advantageous with limited training data, making them suitable choices for such scenarios, makes them the best candidate models for transferability test, i.e., spatial solar radiation estimation.

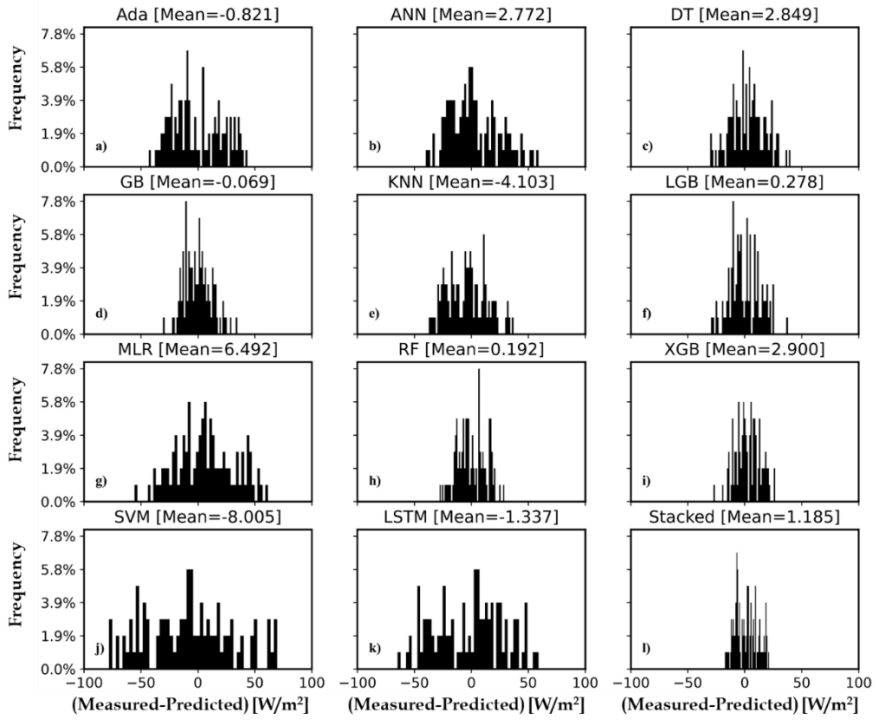

Figure 7: Machine learning model deviation distributions for monthly solar radiation predictions.

To ensure model consistency across all stations, we evaluated the performance of individual models and the Stacked. Individual models exhibited an error range of 2-6%, while the Stacked demonstrated superior performance with an error range of 1-3%. This suggests that the deployed models, especially the Stacked, are robust and effective in predicting global solar radiation across diverse climatic conditions. In contrast, a comprehensive analysis of feature importance, conducted using a random forest model, highlighted substantial differences in feature significance across various stations. Table 6 provides specific examples of these variations.

Table 6: Feature importance for different stations (by using the Random Forest model).

[Lat,Lon]→	All	[9,38.8]	[10,34.6]	[7.1,38.5]	[7.1,40]	[10.3,37.8]	[9.6,41.9]	[8.2,34.6]	[9.3,42.8]
1st	ASSD	ASSD	Temp	CSSD	CSSD	ASSD	Temp	KT	ASSD
2nd	Lon	SZA	CSSD	ASSD	ASSD	Temp	SZA	SZA	CSSD

3rd	Lat	CSSD	KT	Temp	AOD	SZA	WD	CSSD	WS
4th	CSSD	Delclin	WD	Declin	WD	CSSD	Declin	Albed	SZA
5th	Temp	Temp	SZA	AOD	Declin	Declin	KT	ASSD	WD
6th	SZA	WD	Declin	WD	WS	KT	CSSD	Declin	Temp
7th	KT	WS	Albed	WS	SZA	AOD	ASSD	Temp	Declin
8th	Eleva	PM	WS	PM	Temp	WD	WS	WD	KT
9th	Declin	AOD	PM	SZA	PM	WS	PM	WS	AOD
10th	WD	Albed	AOD	KT	KT	PM	AOD	AOD	PM
11th	WS	KT	ASSD	Albed	Albed	Albed	Albed	PM	Albed
12th	Albed	Lat	Lat	Lat	Lat	Lat	Lat	Lat	Lat
13th	PM	Lon	Lon	Lon	Lon	Lon	Lon	Lon	Lon
14th	AOD	Eleva	Eleva	Eleva	Eleva	Eleva	Eleva	Eleva	Eleva

While parameters like Lat, Lon, and Eleva are fixed for each station and therefore not considered by the ML model, other meteorological factors play a crucial role in predicting global solar radiation. The parameter ASSD was found to be a critical factor when considering all stations and a subset of specific stations, as highlighted in Table 6. However, its significance varied across different station groups. This highlights the complex interplay between local climatic conditions and solar radiation patterns, emphasizing the need for station-specific model calibration and parameter optimizations.

4.2. Transferability of Machine Learning Models

4.2.1. Predicting Hourly Solar Radiation

This study evaluates the performance of three ML models (Stacked, XGB, and GB) for predicting solar radiation across various timescales, emphasizing efficiency. Figure 14 showcases hourly solar radiation predictions for three geographically distinct stations (Bahir Dar (BDR), Arba Minch (AM), and Harar (HR)).**Error! Bookmark not defined.** Notably, g lobal solar radiation data from these stations was purposefully excluded from the training datasets to assess model generalizability and transferability. The XGB and GB models achieved remarkable R^2 values ranging from 0.910 to 0.948 for all three stations to predict hourly global solar radiation. This comparative analysis of XGB and GB models revealed distinct performance patterns across the BDR, AM, and HR stations. The XGB model demonstrated superior predictive accuracy at the BDR station, as evidenced by its higher R^2 value. Conversely, the GB model exhibited superior performance at the AM and HR stations. These findings suggest that the GB model may be less effective in capturing the unique solar radiation characteristics of the BDR station. This discrepancy may be attributed to the station's specific climatic conditions, which may deviate from those at the AM and HR stations. To further assess prediction accuracy, RMSE was calculated for both models. RMSE values ranged from 25.598 to 34.485 W/m^2, indicating a good fit between predicted and actual values. The GB model achieved the lowest RMSE (31.599 W/m^2) at the HR station, while the highest RMSE (34.485 W/m^2) occurred at the BDR station for both models. Similarly, the GB model demonstrated the lowest MAE at the HR station (25.598 W/m^2). In essence, this analysis highlights the potential of XGB and GB models for accurate solar radiation prediction across diverse timescales, with minimal computational demands. The findings also emphasize the importance of considering station-specific characteristics when selecting the optimal model for solar radiation prediction. The summary of model performance evaluation metrics for the prediction of hourly solar radiation for the three stations is presented in Table 7.

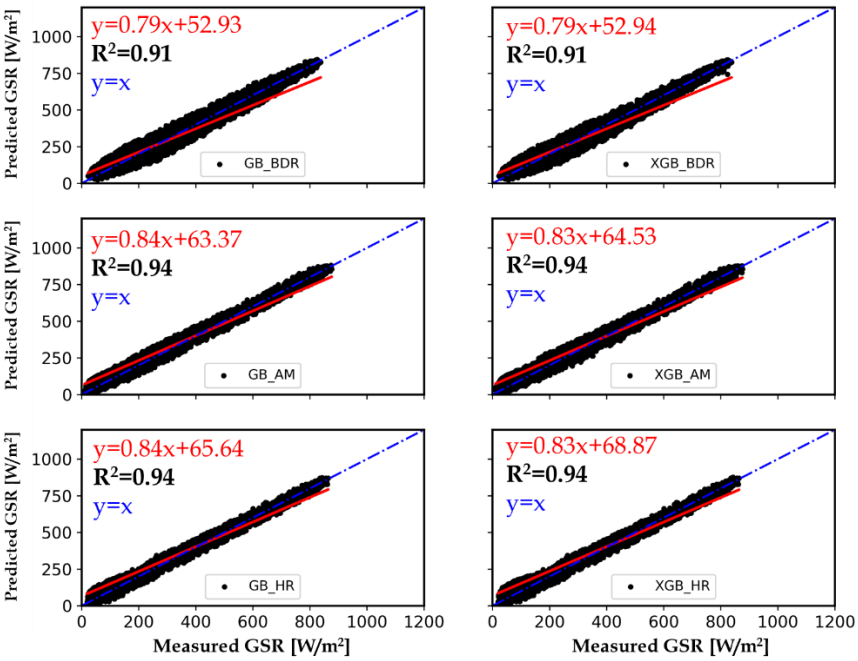

Figure 8: Scatter plots of the cross-validation results for two best ML models in predicting hourly solar radiation for three stations; BDR, AM, and HR.

Table 7: Model evaluation metrics for hourly predicted solar radiation for three stations BDR, AM, and HR stations.

ML	*GB*	*XGB*	*GB*	*XGB*	*GB*	*XGB*
	AM		*BDR*		*HR*	
MAE	*27.49*	*29.74*	*34.48*	*32.73*	*25.59*	*27.76*
RMSE	*33.11*	*35.90*	*41.88*	*39.75*	*31.59*	*34.75*
nRMSE	*0.04*	*0.04*	*0.05*	*0.05*	*0.04*	*0.04*
MAPE	*31.64*	*35.73*	*18.04*	*17.46*	*26.65*	*30.60*
NSE	*0.97*	*0.98*	*0.95*	*0.95*	*0.97*	*0.98*
R²	*0.94*	*0.94*	*0.91*	*0.91*	*0.94*	*0.94*

Figure 15 reveals a significant positive bias in the hourly solar radiation predictions for BDR station using both XGB and GB models. The mean bias for XGB was 10.455 W/m², and for GB, it was 10.714 W/m². This contrasts with the negative biases observed at the other two stations: AM (-31.391 W/m² for XGB, -29.500 W/m² for GB)

and HR (-35.851 W/m² for XGB, -32.025 W/m² for GB). Furthermore, the distribution of hourly bias at BDR station exhibits a wider range (±100 W/m²) compared to the narrower ranges observed at AM and HR. This suggests that the models have greater difficulty capturing the full range of variability in solar radiation at BDR. Overall, the results highlight the importance of station-specific model evaluation. While XGB might outperform GB at BDR, the reverse is true for AM and HR.

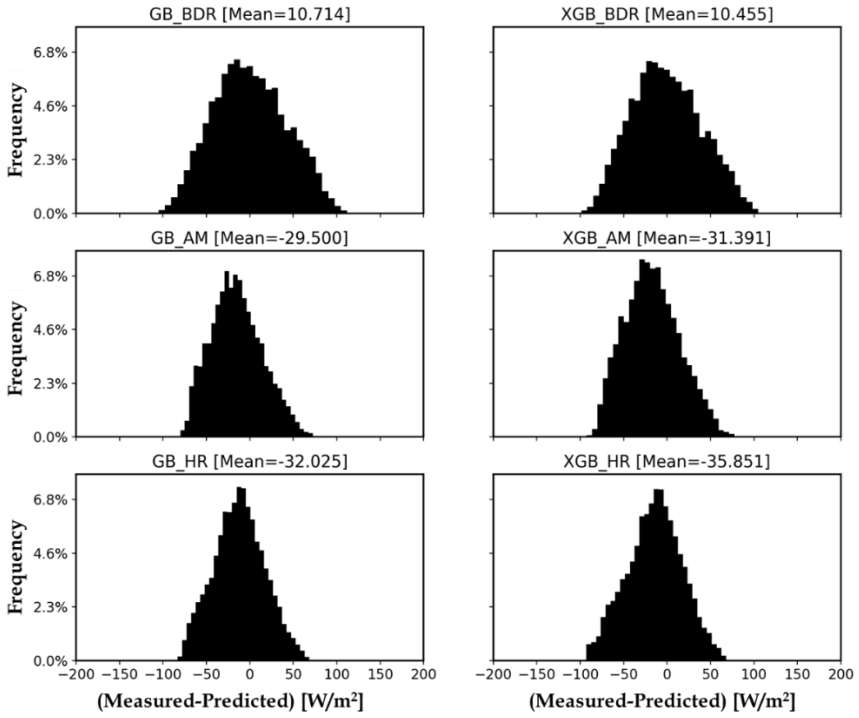

Figure 9: Frequency distribution of hourly solar radiation bias relative to observations from three stations BDR, AM, and HR.

4.2.2. Predicting Daily Solar Radiation

Three ML models (XGB, GB, and Stacked) were evaluated for their ability to predict daily solar radiation at multiple locations (Figure 16). The Stacked model achieved the highest performance, with R^2 0.95 for all locations (*BDR, AM, and HR*) during training, testing, and independent validation. This indicates a strong correlation between predicted and observed solar radiation.

While all models performed well in predicting daily GSR, the Stacked model consistently outperformed individual models, including XGB and GB, across various climatic conditions. This superiority is evident in significantly lower error metrics: MAE, RMSE, nRMSE, and MAPE as presented in Table 8. Additionally, the Stacked model exhibited higher R^2 and NSE. The ensemble approach of the Stacked model, which combines the predictions of multiple models, is the primary reason for its enhanced predictive accuracy across diverse climates. By leveraging the strengths of individual models and mitigating their limitations, the Stacked model provides more robust and accurate estimation across diverse environments. In contrast, standalone models like XGB and GB displayed higher error metrics in specific locations with varying climatic conditions, suggesting a potential lack of adaptability to diverse climatic factors. This underscores the importance of ensemble techniques in improving predictive performance across different environmental settings.

Furthermore, the XGB model demonstrated superior accuracy in predicting hourly global solar radiation at the BDR station but exhibited the lowest performance in predicting daily global solar radiation. This suggests that the effectiveness of standalone models depends not only on climatic conditions but also on the predicted time scale. The summary of model performance evaluation metrics in predicting daily solar radiation is presented in Table 8.

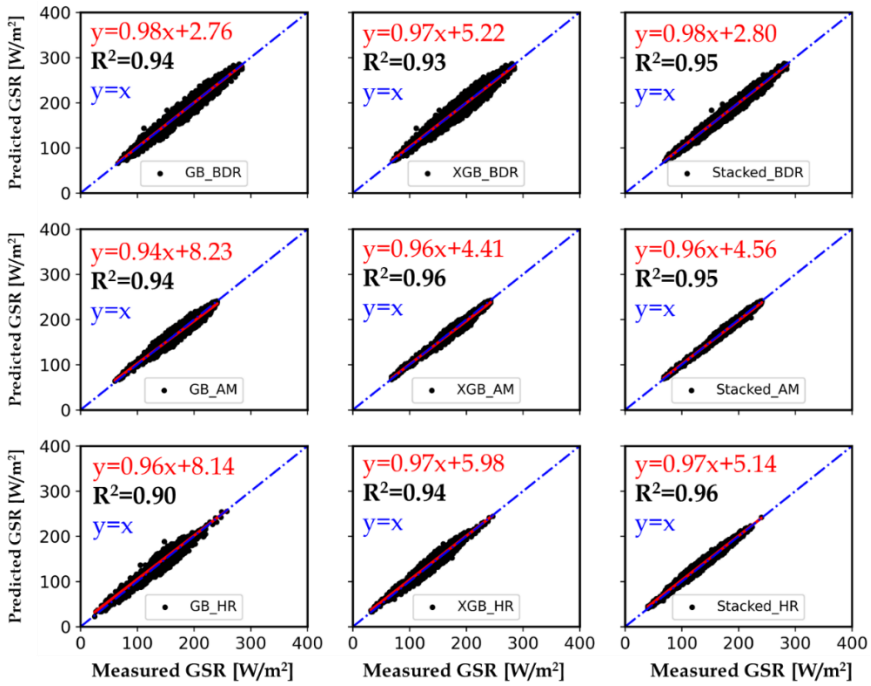

Figure 10: Scatter plots of the cross-validation results for two best models and Stacked models in predicting daily solar radiation for three stations; BDR, AM, and HR.

Table 8: Model evaluation metrics for daily predicted solar radiation for three stations BDR, AM, and HR stations.

ML	*GB*	*XGB*	*Stack*	*GB*	*XGB*	*Stack*	*GB*	*XGB*	*Stack*
	AM			*BDR*			*HR*		
MAE	*8.06*	*6.21*	*5.18*	*9.64*	*10.71*	*7.63*	*9.78*	*7.77*	*5.87*
RMSE	*9.72*	*7.64*	*6.05*	*11.42*	*12.76*	*9.07*	*11.72*	*9.28*	*7.10*
nRMSE	*0.06*	*0.04*	*0.03*	*0.05*	*0.06*	*0.04*	*0.05*	*0.04*	*0.03*
MAPE	*4.67*	*3.54*	*2.99*	*5.45*	*5.95*	*4.34*	*7.46*	*5.98*	*4.62*
NSE	*0.90*	*0.94*	*0.97*	*0.92*	*0.92*	*0.96*	*0.86*	*0.92*	*0.96*
R^2	*0.94*	*0.93*	*0.95*	*0.94*	*0.93*	*0.95*	*0.90*	*0.94*	*0.96*

Analysis of Figure 17 reveals a significantly lower mean bias for all three models (GB, XGB, Stacked) when predicting daily global solar radiation at *BDR, AM, and HR* stations in Ethiopia, compared to their performance on hourly data. This finding aligns with physical expectations, as daily solar radiation exhibits inherently lower variability

than hourly values. The maximum positive/negative bias observed is considerably tighter for daily predictions, ranging from ±40 W/m² at BDR and HR to ±20 W/m² at AM. This tighter range further emphasizes the reduced complexity in modeling daily compared to hourly solar radiation. Among the evaluated models, the Stacked model consistently demonstrates superior performance in predicting daily solar radiation across all stations.

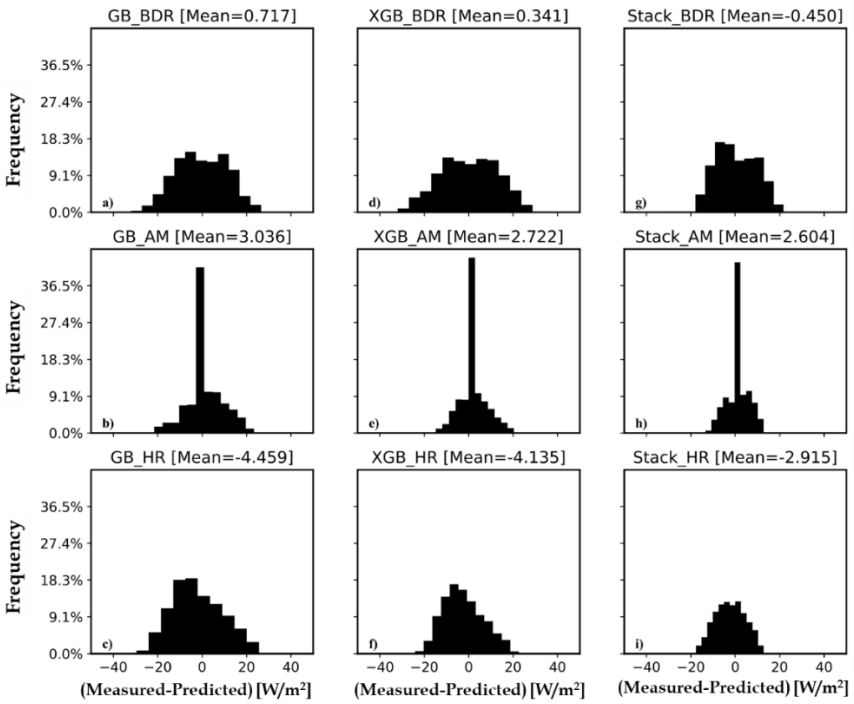

Figure 11: Frequency distribution of daily solar radiation bias relative to observations from three stations; BDR, AM, and HR.

4.2.3. Predicting Monthly Solar Radiation

Figure 18 depicts a comparison of predicted and observed monthly solar radiation for three models evaluated at three stations. The R^2, a metric for goodness-of-fit, varied between the models, ranging from 0.904 for the GB model at AM to 0.959 for the Stacked model at HR. This indicates that the Stacked model exhibited the strongest correlation between predicted and observed values at the HR station. Performance evaluation using RMSE revealed variations across both models and stations. RMSE values for all models

ranged from 5.908 W/m² to 9.047 W/m², with the GB model at AM demonstrating the highest error, suggesting its lower accuracy in predicting solar radiation at that specific location compared to the other two models at the same station and all three models at the other stations. Similarly, the Stacked model achieved the lowest MAE at all three stations (BDR: 5.117 W/m², AM: 7.472 W/m², HR: 5.448 W/m²), signifying its superior performance in capturing the average magnitude of prediction errors across the stations. This analysis highlights the importance of considering both model type and geographical location when assessing solar radiation prediction accuracy. The complete model performance evaluation metrics of the models at the three stations are given in Table 9.

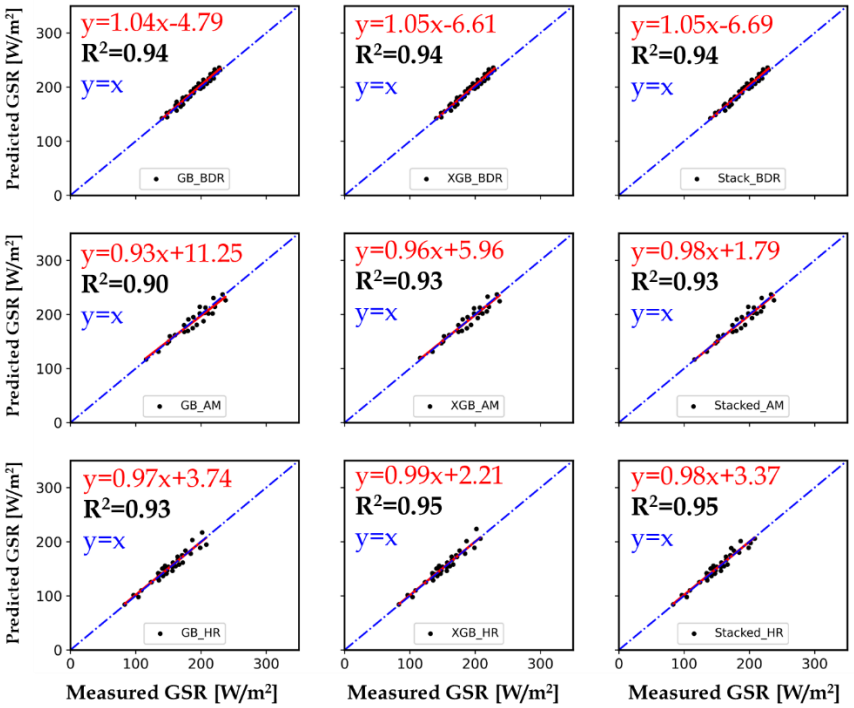

Figure 12: Scatter plots of the cross-validation results for the two best models and Stacked models in predicting monthly solar radiation for three stations; BDR, AM, and HR.

Table 9: Model evaluation metrics for monthly predicted solar radiation for three stations Bahir Dar (BDR), Arba Minch (AM), and Harar (HR) stations.

ML	*GB*	*XGB*	*Stack*	*GB*	*XGB*	*Stack*	*GB*	*XGB*	*Stack*

	AM			*BDR*			*HR*		
MAE	*7.66*	*7.27*	*7.47*	*5.07*	*5.14*	*5.11*	*6.04*	*5.55*	*5.44*
RMSE	*9.04*	*8.43*	*8.55*	*5.90*	*6.02*	*6.02*	*7.31*	*7.07*	*6.63*
nRMSE	*0.07*	*0.07*	*0.07*	*0.07*	*0.07*	*0.07*	*0.06*	*0.06*	*0.05*
MAPE	*3.94*	*9.97*	*11.07*	*2.67*	*2.69*	*2.68*	*3.87*	*3.60*	*3.59*
NSE	*0.91*	*0.92*	*0.92*	*0.94*	*0.94*	*0.94*	*0.93*	*0.93*	*0.94*
R^2	*0.90*	*0.93*	*0.93*	*0.94*	*0.94*	*0.94*	*0.93*	*0.95*	*0.95*

The analysis in Figure 19 reveals that the model bias is primarily concentrated within a range of ±10 W/m². Interestingly, the mean bias for BDR and HR stations exhibits a negative trend, while the AM station displays a positive mean bias. An additional detailed evaluation of model scalability and transferability is presented in Table 10.

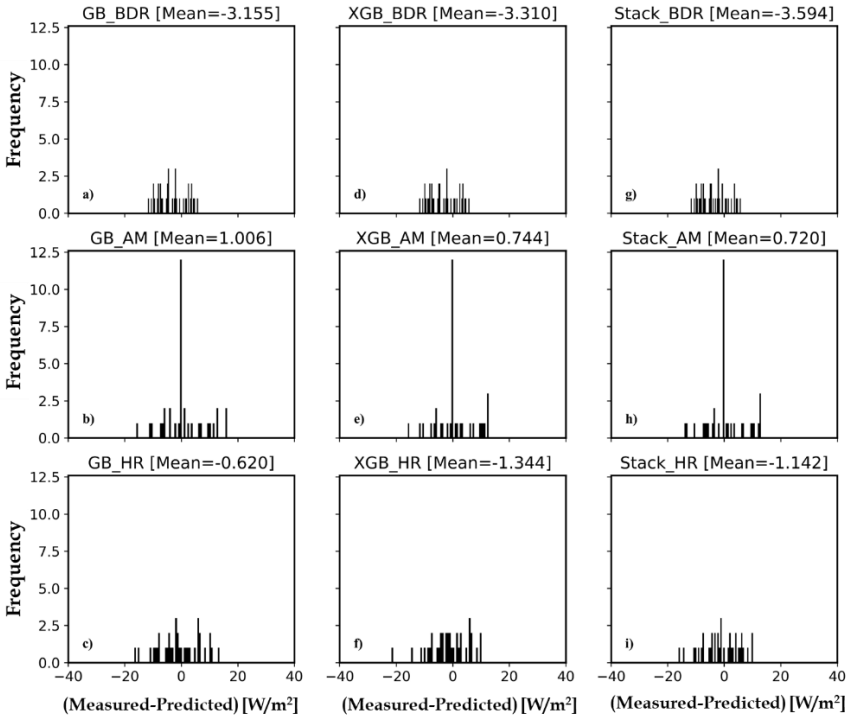

Figure 13: Frequency distribution of monthly solar radiation bias relative to observation at three stations; BDR, AM, and HR from ML models.

Table 10: Summary of model transferability performance for three different stations.

Stations	*Hourly*	*Daily*	*Monthly*
Bahir Dar (BDR)	*XGB > GB*	*Stacked > GB > XGB*	*Stacked > GB > XGB*
Arba Minch (AM)	*GB > XGB*	*Stacked >X GB > GB*	*Stacked >X GB > GB*
Harar (HR)	*GB > XGB*	*Stacked >X GB > GB*	*Stacked >X GB > GB*

Figure 20 depicts box plots that compare the performance of various ML models on three-time scales: hourly, daily, and monthly. The center line of the box represents the median error, the box encompasses the middle quartiles (IQR), and the whiskers extend to data points within 1.5 times the IQR from the median. Outliers are depicted by individual data points beyond the whiskers. The result suggests that the models generally perform better on larger time scales. This is likely because data at higher time scales exhibits a more uniform distribution compared to lower time scales. This characteristic allows the models to more effectively identify patterns within the data. Some of the models, including GB, LGB, RF, XGB, and Stacked, consistently perform well across all time scales. These models are known for their ability to handle complex relationships between features and large datasets. In contrast, models such as Ada, ANN, MLR, CNN, and SVM tend to perform relatively better on shorter time scales. These models are generally simpler to train and may be more suitable for capturing short-term trends. It's important to note that there is a significant variation in performance, even among models applied to the same time scale. This highlights the importance of carefully selecting a model that best suits the specific task, as this choice can significantly impact the outcome. Researchers should thoroughly evaluate different models before deploying them in real-world applications.

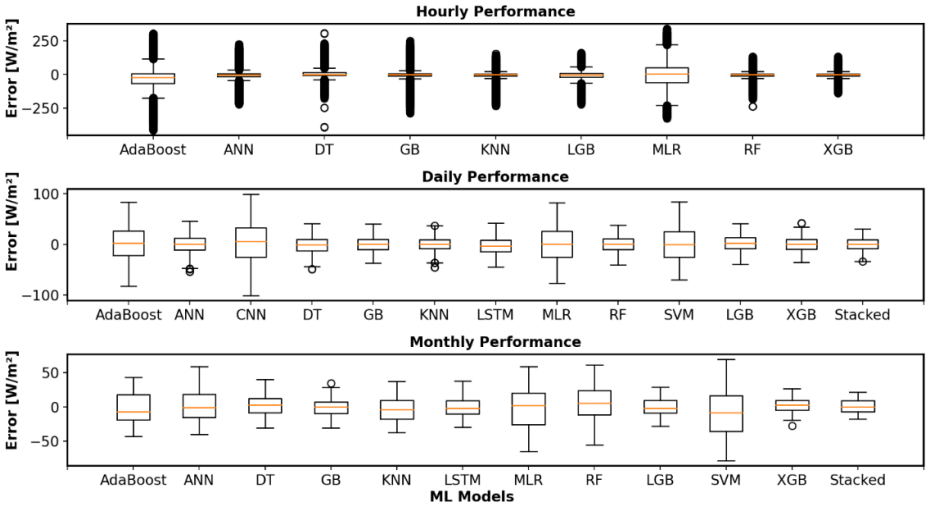

Figure 14: Boxplot diagrams of all ML models for hourly, daily, and monthly time scales.

Similarly, Figure 21 presents box plots visualizing the distribution of performance errors for different ML models across three time scales (hourly, daily, and monthly) at three stations (BDR, AM, and HR). The boxplots tend to be wider on the hourly scale compared to the daily and monthly scales, suggesting greater error variability on the shorter time scale. Models like XGB_AM and XGB_BDR might have consistently lower median errors across all time scales at their respective stations (AM and BDR).

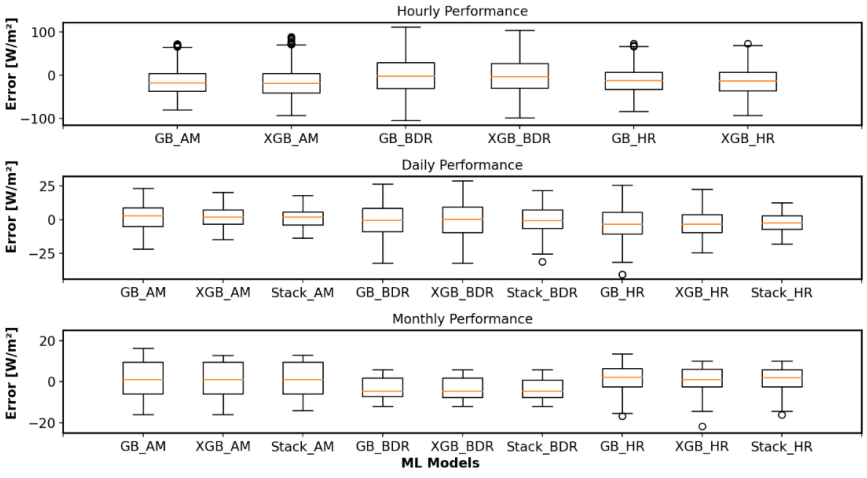

Figure 15: Boxplot diagrams of the three best MLs for hourly, daily, and monthly time scales at three stations; BDR, AM, and HR.

The violin plots (Figure 22) show the distribution of performance errors for all ML models across three-time scales (hourly, daily, monthly). The wider the "body" of the violin plot at a particular point indicates a higher density of errors at that value. The center line represents the median error, and the horizontal lines extending from the violin represent the quartiles (IQR). There appears to be a general trend of improved performance (lower error) with increasing time granularity (hourly to monthly). Models GB, XGB, LGB, Stacked generally have a narrower violin plot across all time scales, suggesting a more consistent distribution of errors and potentially better performance. Whereas Ada, ANN, MLR, RF, and SVM models tend to be wider, particularly on the daily, and monthly scale, indicating greater variability in errors. These models might be more suited for capturing short-term trends.

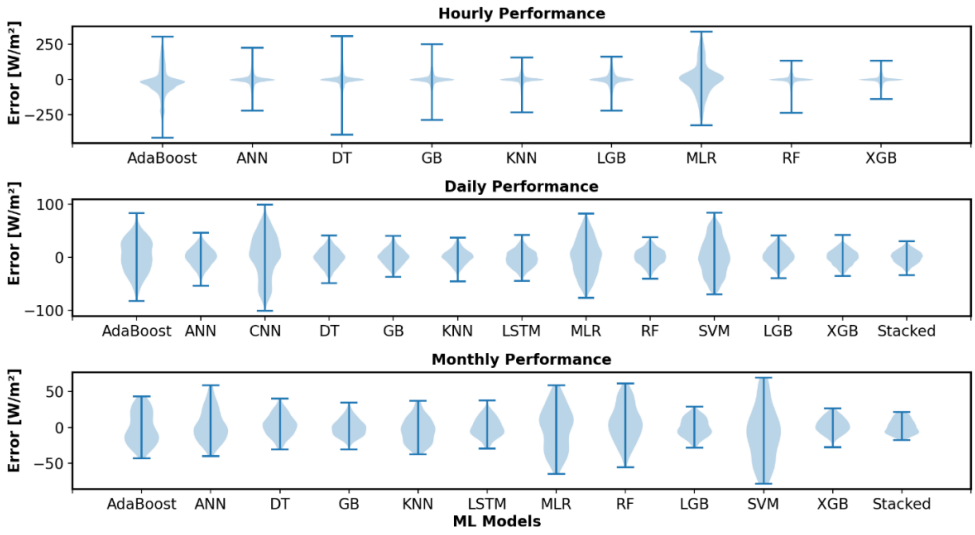

Figure 16: Violin plot diagrams of all ML models for hourly, daily, and monthly time scales.

The violin plots (Figure 23) show the distribution of performance errors for three ML models across three-time scales (hourly, daily, monthly) for each station (BDR, AM, and HR). In BDR station, LGB_BDR and XGB_BDR appear to have consistently lower median errors across all time scales. XGB_AM and Stacked_AM have a narrower violin plot across most time scales, suggesting potentially better and more consistent

performance at the AM station. Similar to BDR, LGB_HR and XGB_HR show generally lower median errors throughout at HR station.

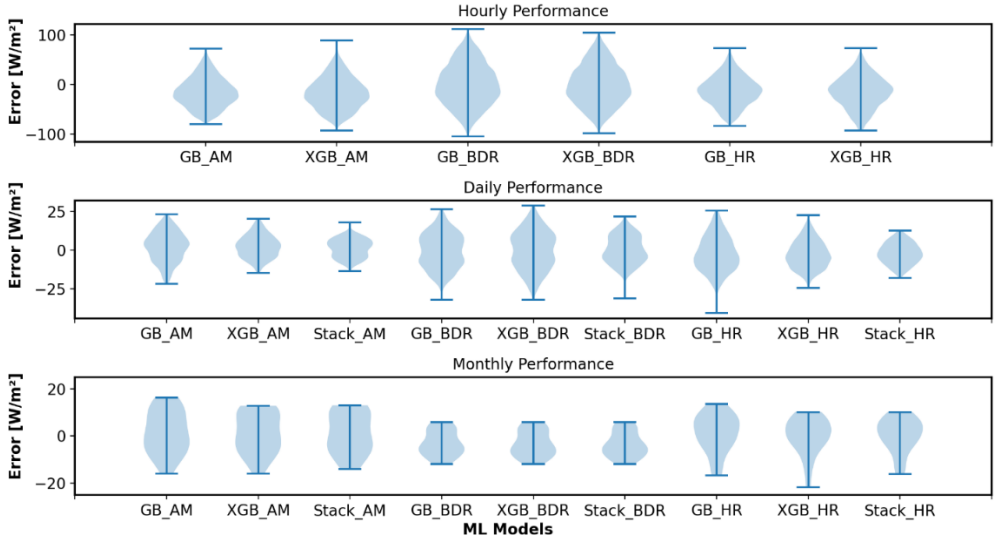

Figure 17: Violin plot diagrams of the three best ML models for hourly, daily, and monthly time scales at three stations; BDR, AM, and HR.

Taylor plots (Figure 24) are graphical tools used to summarize the performance of a model in terms of two key metrics: correlation (accuracy in capturing the pattern of variations), and standard deviation (similarity in spread between predictions and observations). A circular data point in the plot represents each ML model. The closer the point is to the reference point (marked by a red star) in the center, the better the model's performance across two metrics. An ideal model would lie on the reference point, indicating perfect agreement between the model's predictions and the observed values. The model closest to the red star appears to be XGB, followed by RF. This suggests that these models exhibit the best combination of correlation, and standard deviation for hourly predictions (Figure 24a). The Stacked model followed by LGB seems to be the closest to the reference star, indicating potentially superior performance for daily predictions (Figure 24b). Unlike the other plots, there isn't a single model that stands out near the reference point. However, XGB and Stacked appear to be relatively close,

suggesting they might perform better for monthly predictions (Figure 24c), but the standard deviation of the Stacked model is higher than XGB.

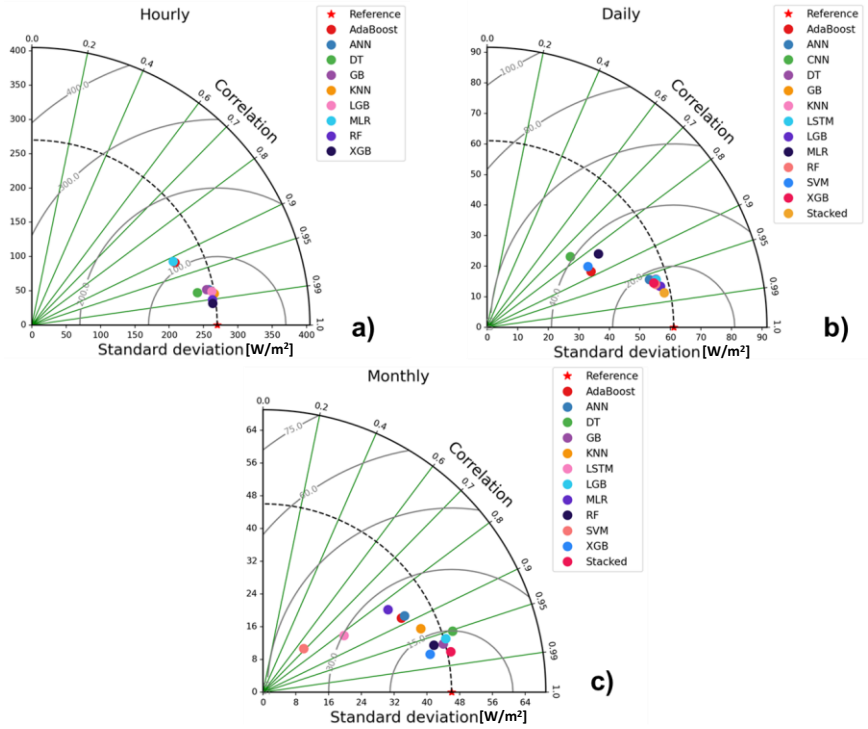

Figure 18: Taylor plot diagrams of all ML models for hourly, daily, and monthly time scales; hourly (a), daily (b), monthly (c).

Figure 25 depicts a seasonal solar radiation map of Ethiopia for the year 2022, generated using the Stacked model. The map is segmented into four seasons: winter (December-February), spring (March-May), summer (June-August), and autumn (September-November). Each season is represented by a distinct color distribution, potentially indicating variations in solar radiation intensity across the country throughout the year. Higher solar radiation intensity is likely illustrated by bright red colors, while dark green colors represent areas with lower intensity. The map provides a visual representation of how solar radiation patterns fluctuate across Ethiopia throughout the year, potentially due to seasonal factors.

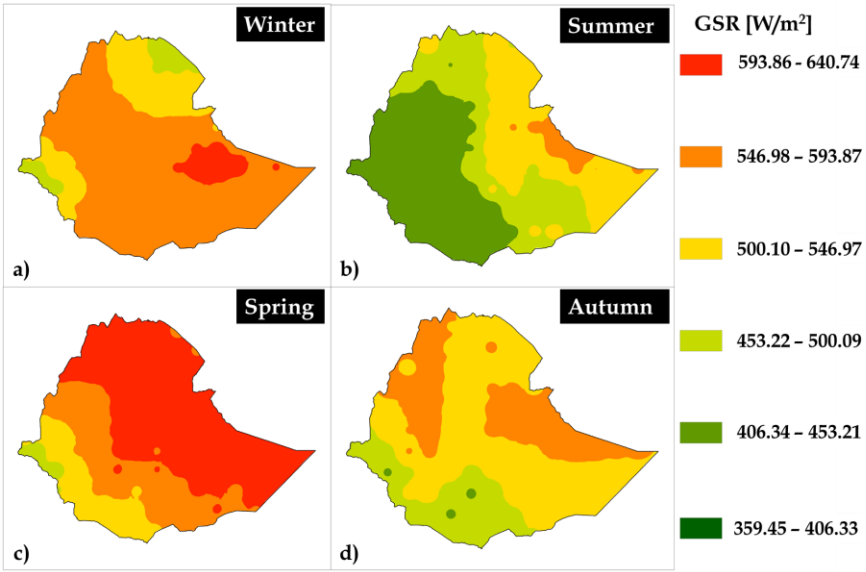

Figure 19: Seasonal distribution global solar radiation (GSR) [in W/m²] map of Ethiopia: winter (a), summer (b), spring (c), and autumn (d) using the Stacked model for the year 2022.

During winter, the northeastern and western regions of Ethiopia, encompassing areas towards Afar and Gambella, exhibit comparatively lower GSR compared to other parts of the nation. The GSR ranges across the country in winter is from 546 to 594 W/m². Most parts of Ethiopia witness the lowest GSR in the Summer. Regions like western, southwestern, and portions of southern Ethiopia receive the least amount of solar radiation during this season, with GSR values ranging from 359 to 406 W/m². Interestingly, eastern and northeastern Ethiopia experience a relative increase in GSR during summer, ranging from 500 to 546 W/m². Compared to the other three seasons, spring boasts the highest GSR across most of Ethiopia, with values reaching between 594 and 641 W/m². Autumn exhibits the third-highest GSR values following winter. GSR in autumn varies from 453 to 593 W/m², with the highest values observed in the eastern and northwestern regions of Ethiopia. In essence, the GSR distribution across Ethiopia demonstrates a clear seasonal pattern. Spring offers the most favorable conditions for solar radiation, followed by winter. Conversely, autumn and summer exhibit the lowest GSR values, with summer experiencing the least radiation in most parts of the country.

Thus, the study found that ML models generally outperform DL models when the training dataset is limited in size.[134] This is likely because ML models are less complex and require fewer data points to learn effectively. In this study, with a dataset size of approximately 341,440 hourly data points, XGB emerged as the single best-performing model in terms of accuracy, transferability, and scalability for solar radiation estimation. This finding aligns with the work of Huang *et al.*, who reported that XGB, along with RF and GB, achieved superior performance for daily and monthly solar radiation prediction.[135] The study also investigated stacked ensemble models, which combine the outputs of multiple ML models. The results indicated that the stacked ensemble model consistently surpassed the performance of individual models across daily, and monthly time scales. This is corroborated by the findings of Basaran *et al.*, who observed enhanced estimation accuracy when employing ensemble models for hourly solar radiation prediction.[136] The analysis of GSR data revealed seasonal variations in solar irradiance across Ethiopia. Generally, spring and winter exhibited the highest solar radiation levels, particularly in the northern, northeastern, and eastern regions period (i.e., regions experience the dry climate). Conversely, the summer season witnessed the lowest solar radiation, especially in the western, northwestern, southwestern, and southern parts of the country (i.e., regions situated topographically at highland area). These seasonal trends can be attributed to several factors. Increased sunshine hours, minimal precipitation, clear skies, and strategic spatial distributions during spring likely contribute to higher irradiance during this period. Conversely, the summer months are characterized by heavy cloud cover and frequent rainfall, leading to reduced direct irradiance and enhanced diffused radiation (reflected into space).[137] These observations are qualitatively inline with the findings of Fazzini *et al.* and Benti *et al.*, who reported similar seasonal variations in Ethiopia's solar radiation.[56,138] The study's findings suggest that Ethiopia has significant potential for solar energy generation throughout the year. The observed range of solar radiation distribution (359 to 641 W/m^2) indicates a favorable resource availability. However, the seasonal variations in solar radiation highlight a degree of dependence on seasonal factors for solar energy harvesting using photovoltaic

(PV) systems. Spring and winter seasons appear most suitable for solar energy production, while summer months may necessitate alternative energy sources or energy storage solutions.

4.3. Spatial and Temporal Variability of Crystalline Silicon Solar Cell Performance in Ethiopia

Assessing solar energy and analyzing solar cell performance nationwide, considering different locations and seasons, are crucial for the efficient use of PV power systems. The accurate evaluation of solar cell/module/panel performance necessitates a comprehensive understanding of several key parameters. These parameters, often detailed on solar cell/module/panel datasheets, directly influence both system design and operational efficiency. The peak sun hours (PSH), plane-of-array (POA) irradiance, PV cell temperature, and PV cell parameters such as, short-circuit current density (J_{sc}), saturation current density (J_o), short-circuit current (I_{sc}), maximum power current (I_{mp}), open-circuit voltage (V_{oc}), maximum power voltage (V_{mp}), fill factor (FF), maximum power point (P_{mp}), and efficiency (η) are determined across the nation.

4.3.1. Peak Sun Hours (PSHs) Estimation

A solar cell's energy depends on the effective solar radiation (insolation) time. PSH measures sunlight intensity, represents the average daily solar insolation and can assist in estimating the electricity output of solar panels. It provides a straightforward way to determine the appropriate size for a PV system[139]. Solar radiation across the globe varies significantly (1.0 – ~7.4 kWh/m²/day) with latitude being the key driver.[140] Regions closest to the equator (latitude ranges between 0^o to 10^o) receive the most intense sunlight due to the sun's rays near-perpendicular incidence angle.[141] Indeed, Ethiopia exemplifies this as its massive landmass (i.e., ~ 97%, within latitude 4 to 12^o), is situated within the closest to equatorial zone.

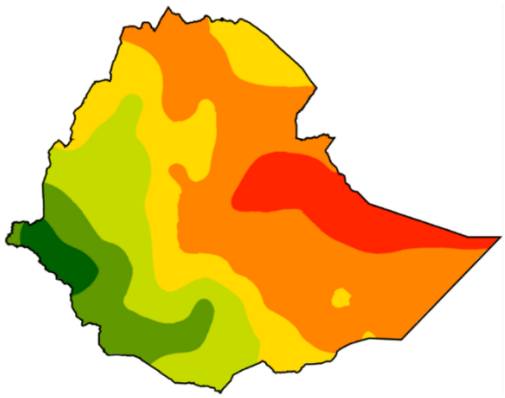

Key	GSR [W/m²]	PSH [kWh/m²/day]
	575.12-601.49	6.29-6.57
	548.73-575.11	6.00-6.28
	522.35-548.72	5.71-5.99
	495.96-522.34	5.42-5.70
	469.58-495.95	5.13-5.41
	443.18-469.57	4.83-5.12

Figure 4-20: Average annual distribution of GSR [in W/m²] and peak sun hour, PSH [in kWh/m²/day] over Ethiopia.

Figure 4-20 summarizes the distribution of solar radiation across Ethiopia for 2022. Based on this study, the average hourly annual global solar radiation and peak sun hour ranges between 443-601 W/m² and 4.83-6.57 kWh/m²/day, respectively. The results are comparable with Solargis data, a reputable source for solar resource assessment (www.solaris.com, solar atlas of Ethiopia). To understand the seasonal dependency of the peak-sun hours, we have studied the daily average seasonal peak-sun hours at different seasons in the year 2022. Figure 4-21 presents the daily average seasonal peak-sun hours over Ethiopia in the four seasons. Figure 4-21 shows a distinct seasonal pattern in peak sun hours in the country. The study found that spring receives the highest irradiance (5.29 - 7.11 kWh/m²/day), followed by winter (5.08 - 6.57 kWh/m²/day). On the other hand, summer experiences the least (3.91 - 6.44 kWh/m²/day), while autumn falls in between (4.69 - 6.42 kWh/m²/day). In summary, the solar radiation decreases from spring, winter, autumn, and summer respectively.

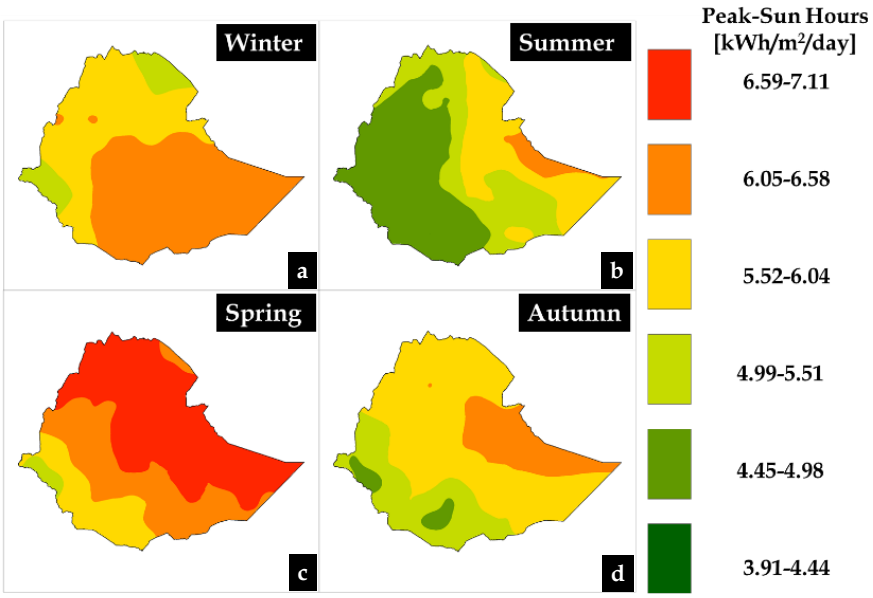

Figure 4-21: Average seasonal peak sun hours (in kWh/m²/day) over Ethiopia during winter (a), summer (b), spring (c), and autumn (d) seasons.

In this study, we also investigated the percentage of landmass that receives specific peak sun hours (PSH) ranges during each season by using a field calculator (ArcGIS). Thus there is significant irradiance (> 71% landmass cover) with PSHs ranging between 6.21 and 7.11 kWh/m²/day in spring, indicating extended sunshine and high solar potential. However, this dominance in irradiance decreases in winter, when more than 64% of the nation's landmass experiences peak sun hours ranging between 5.49 to 6.21 kWh/m²/day. On the other hand, autumn (more than 62% with 5.13 to 5.99 kWh/m²/day) and summer (more than 54% with 4.55 to 5.81 kWh/m²/day) exhibit further reductions, highlighting the progressive decline in sunlight availability. These seasonal trends likely stem from contrasting weather patterns. On the other hand, spring and winter, with minimal precipitation, experience clear skies. Conversely, summer's heavy cloud cover and frequent rainfall significantly reduce direct irradiance, favoring diffused radiation and lower overall solar flux for most regions of the country (see Appendix on peak-sun hour distribution, in % coverage, in Table A1, respectively)[142].

4.3.2. Plane of Array (POA) Irradiance

POA irradiance is used to quantify the incident irradiance on a given solar module/panel/array, and it depends on the Sun's position and PV orientation. It also affects solar cell performance at large. Figure 4-22 illustrates the distribution of average POA irradiance (in kW/m^2) across Ethiopia. As seen from Figure 4-22, the study highlights a seasonal-dependent variation in solar energy throughout the year. Apparently, spring emerges as the season with the most extensive and strong solar resource, and over 71% of the landmass receives exceptionally high irradiance levels, ranging from 0.98-1.20 kW/m^2, indicating exceptional potential for solar power generation. Winter closely follows spring, a significant portion of the country, i.e., more than 71% of the nation experiences irradiance values within a relatively desirable range of 0.87-1.04 kW/m^2. Autumn witnesses a transition, with irradiance levels settling at intermediate values between 0.60 and 0.99 kW/m^2. Notably, here in autumn, over 54% of the land area still receives irradiance in the favorable band of 0.60 to 0.79 kW/m^2 during this season. During the summer, the amount of sunlight and favorable conditions for generating solar energy are at their lowest. Throughout the country, the sunlight levels in summer range from 0.51 to 1.04 kW/m^2, with over 49% of the landmass receiving lower values between 0.51 and 0.78 kW/m^2. The different seasonal sunlight levels, shown in Figure 4-22, highlight Ethiopia's significant potential for producing solar energy all year round. Spring and winter stand out as promising seasons, boasting extensive areas with exceptionally high irradiance levels. Even during autumn and summer, a considerable portion of the country receives favorable conditions for solar power generation. In brief, the spatial and seasonal irradiance results, with variability, present a compelling picture of Ethiopia's abundant solar energy resource (see Appendix of POA irradiance distribution and land mass coverage [%], in Table A2 respectively).

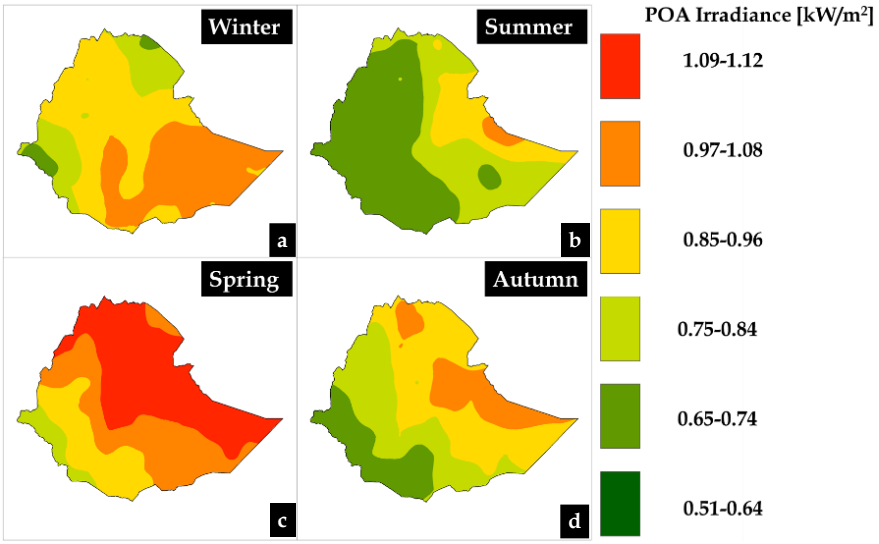

Figure 4-22: Average seasonal distribution of POA irradiance (in W/m²) over Ethiopia during winter (a), summer (b), spring (c), and autumn (d) seasons.

4.3.3. Solar Cell Temperature (T_c)

Crystalline silicon solar cell efficiency diminishes with increasing operating temperature.[143] Yet, the temperature dependence varies spatially and seasonally in a given geographical location or nation. A study investigated the seasonal and locational variations in the operating temperature of c-Si solar cells. Notably, these devices typically operate at temperatures exceeding ambient air temperature due to the conversion of absorbed solar energy into heat. The ambient air and the glass-covered solar cell absorb and convert heat differently. Figure 4-23 presents the average seasonal distribution of solar cell temperature over Ethiopia during the four seasons. As seen from Figure 4-23, Ethiopian solar cell temperatures show significant seasonal variability. The highest temperatures, ranging from 44.55-64.13 °C, are experienced during spring, with over 61% of the landmass exceeding 49.46-59.24 °C. This effect is most prominent in the northeast/east and northwest, likely due to amplified solar radiation (Figure 4-23). Winter temperatures range from 41.85-54.59 °C, with the east, southeast, and northwest experiencing the highest warmth. Central and northern regions experience relatively

coolest winter temperatures, ranging from 40.75-46.45 °C. Summer temperatures are the lowest nationwide, ranging from 29.86-54.08 °C, with over 54% of the range falling between 29.86 and 41.97 °C. Autumn temperatures fall in the middle ground between winter and summer extremes, ranging from 35.85-54.61 °C, with 58% of the range falling between 40.55-49.92 °C. This underscores the critical role of considering seasonal variations in designing and deploying solar energy systems to ensure optimal year-round performance (see Appendix on solar cell temperature distribution and landmass coverage [%], in Table A3 respectively).

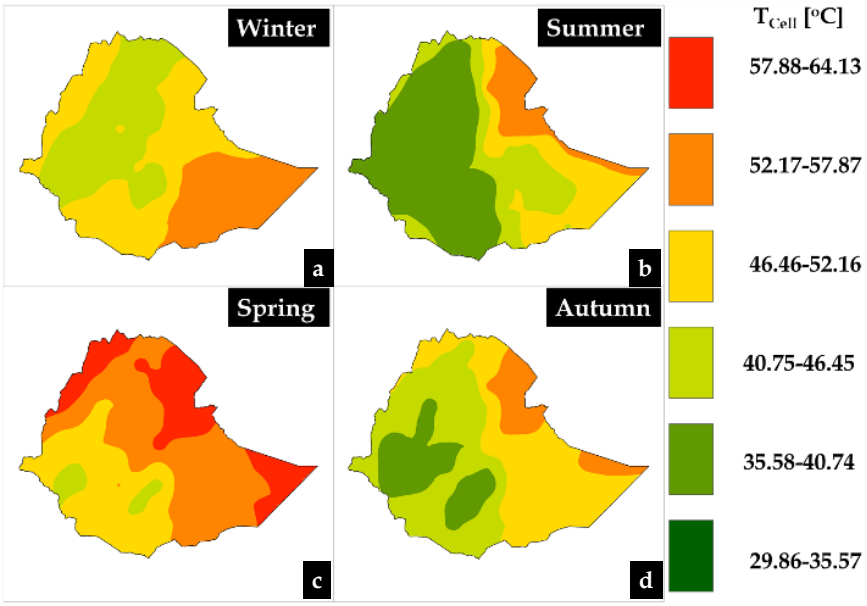

Figure 4-23: Average seasonal distribution of solar cell temperature (in °C) over Ethiopia during winter (a), summer (b), spring (c), and autumn (d) seasons.

4.3.4. Solar Cell Parameters

A. Reverse Saturation Current Density (J_0)

The reverse saturation current density affects the performance of a solar cell and increases with the device's temperature. Figure 4-24 illustrates the average seasonal distribution of reverse saturation current density (J_o). The range of J_o at different seasons,

in mA/cm², is as follows: winter (2.81-9.80) ×10^{-12}, summer (0.46-8.68) ×10^{-12}, spring (2.57-20.86) ×10^{-12}, and autumn (1.13-13.32) ×10^{-12}. Higher temperatures result in higher J_0, as shown in Figure 4-24.[144] Ethiopia exemplifies this connection. Northern and eastern regions, experiencing the hottest temperatures (57.88-64.13°C), exhibit the highest J_0 values (17.47-20.86 mA/cm²). Conversely, cooler western and southwestern regions boast the lowest J_0 (0.46-3.86 mA/cm²). This translates to potentially better solar cell performance in these cooler areas due to lower J_0. J_0 significantly impacts factors like efficiency and power output, highlighting the importance of understanding its spatial and seasonal variation.

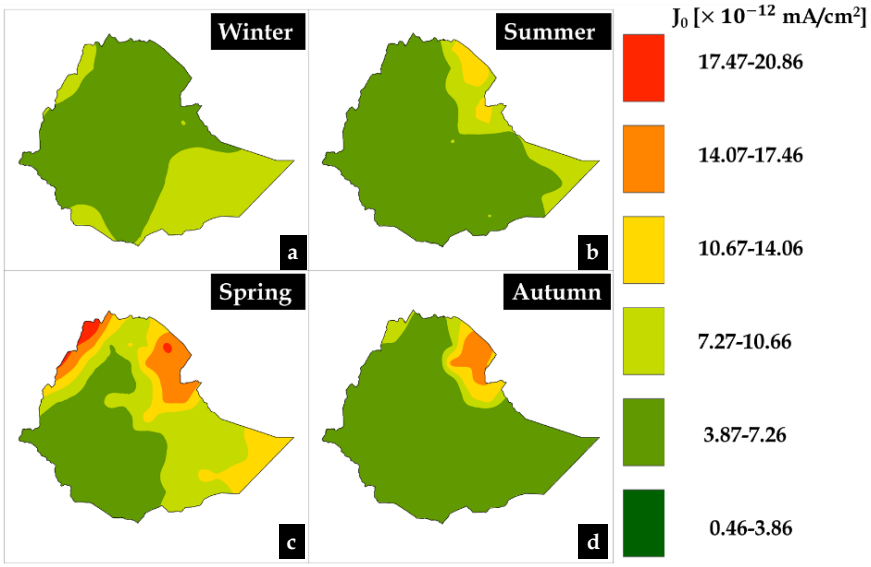

Figure 4-24: Average seasonal distribution of reverse saturation current density (J_0) over Ethiopia during winter (a), summer (b), spring (c), and autumn (d) seasons.

We also study the relative coverage (%) of the J_0, geographical share, within the above ranges in each season. Apparently, spring experiences the highest J_0, with over half (55%) of the landmass reaching a range between 6.02×10^{-12} and 13.18×10^{-12} (mA/cm²), i.e., spring is the season witnessing a relatively high reverse saturation current density. Winter follows closely with J_0 ranging from 2.81 to 6.02×10^{-12} (mA/m²) with more than 52% of the area coverage. Autumn experiences intermediate J_0 (1.13 to 5.24×10^{-12}

mA/cm^2) covering over 58% of the area coverage. Summer exhibits the lowest relative J_o, with over 75% of the country experiencing values between 0.46 and 3.87×10^{-12} (mA/cm^2). This trend highlights the importance of considering seasonal variations when designing and deploying solar energy systems for optimal performance throughout the year (see Appendix of J_o distribution and landmass coverage [%], in Table A4, respectively).

B. Short Circuit Current Density (J_{sc})

The short-circuit current density *(J_{sc})* is related to the generation and collection of light-generated carriers, and it determines how many amps a cell/panel can handle when connected to a solar charge controller or an inverter. It is highly dependent on the POA irradiance. Figure 4-25 presents the average seasonal distribution of short circuit current density J_{sc} in the four seasons. In the Figure 4-25, there appears to be a positive correlation between incident solar irradiance (POA irradiance, Figure 4-22) and J_{sc} of solar cells. This means that regions with stronger sunlight tend to have a higher J_{sc}, as the photocurrent increases with the intensity of light. Generally, unlike tropical regions, Ethiopia experiences relatively better light intensity and therefore higher J_{sc} values. However, within Ethiopia, northeastern and eastern areas, receiving the highest POA irradiance (1.09-1.12 kW/m^2, see Figure 4-22), exhibit the greatest J_{sc} values (29.98-33.30 mA/cm^2). On the other hand, cooler western and southwestern regions with the lowest temperatures also have the lowest J_{sc} (13.34-16.67 mA/cm^2). Here, it is also worth knowing that the average seasonal distribution of J_{sc} within Ethiopia in winter, summer, spring, and autumn are 19.02-28.52, 13.34-28.40, 20.54-33.30, and 15.79-26.94 (mA/cm^2), respectively. These results exhibit excellent agreement with the experimental values reported by Green *et al.*[145]

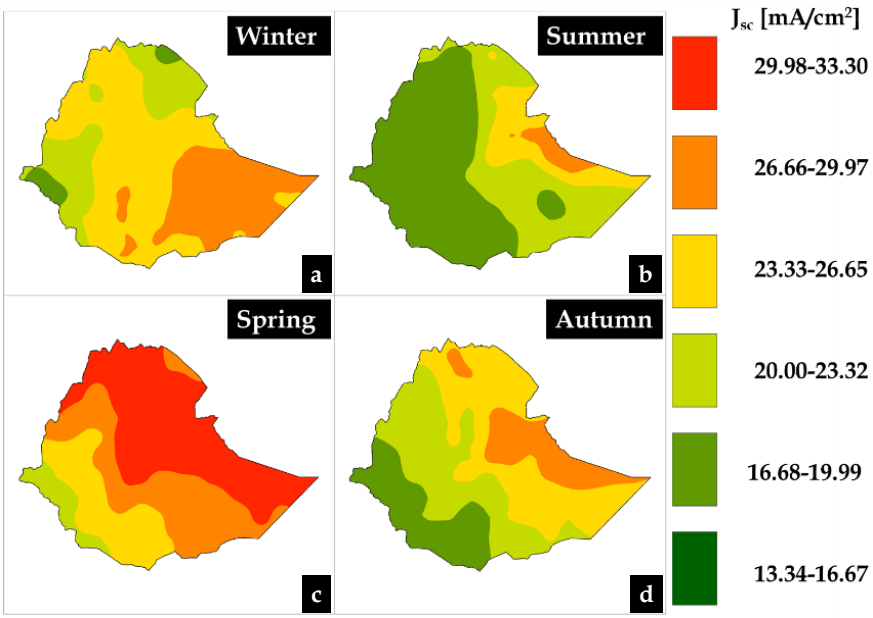

Figure 4-25: Average seasonal distribution of short circuit current density (J_{sc} in mA/cm²) over Ethiopia during winter (a), summer (b), spring (c), and autumn (d) seasons.

The relative coverage of the short circuit current density, dominating range of J_{sc}, in each season, is also studied based on their corresponding percentage coverage. Based on our areal-based irradiance coverage, using percentage calculation, spring emerges as the leading season for solar cell electricity production as over 69% of the nation is experiencing a superior range of short-circuit current density (J_{sc}: 27.96-33.30 mA/m²). Winter comes in a close second place (>63%: 24.62-28.52 mA/m²), while autumn occupies the middle ground (> 53%: 19.95-24.45 mA/m²). Summer (>50%: 20.38-28.40 mA/m²) brings up the relatively lowest J_{sc} (though comparable to autumn with small values difference). Besides, it is important to note that the trend I_{mp} *[A]* over Ethiopia during the four seasons is similar to J_{sc} as both (J_{sc} and I_{mp}) are determined in the same way (see Appendix Figure A1 for I_{mp}). Such a seasonal variation is a key factor to consider when designing and installing solar energy or PV-based systems to ensure their functionality at their best year-round (see Appendix of J_{sc} distribution and landmass coverage [%] in Table A5, respectively).

C. Open Circuit Voltage (V_{oc})

The open circuit voltage of a PV cell, the maximum voltage it can produce when no current flowing, is another parameter that controls the performance of the device like that of J_{sc}. Figure 4-26 presents the average seasonal distribution of open circuit voltage over Ethiopia in four seasons. As seen in Figure 4-26, the seasonal V_{oc} distribution ranges are presented as follows: winter (0.61 - 0.64 V), summer (0.61 - 0.63 V), spring (0.61 - 0.65 V), and autumn (0.60 - 0.62 V). The results indicate that the solar cell in summer experiences the lowest solar cell temperature when compared with the other three seasons. Here, summer showed a relatively high V_{oc}, which is related to the season's nationwide reduced temperature (> 54% ranges between 29.86 and 41.97 °C). On the contrary, spring and winter (hottest solar cell records) showed a relatively low V_{oc}, possibly due to the effect of increased temperature arising from the decline of V_{oc}. In Figure 4-26, it is observed that the northeast/east regions exhibit relatively low V_{oc} values, ranging from 0.603 V to 0.610 V across the four seasons. In contrast, the cooler western/central regions tend to have relatively high V_{oc} values, ranging from 0.64 V to 0.65 V. Here, it is worth to notice that northeast/east regions have a relatively high device temperature ranging from 57.88 °C to 64.13 °C while the cooler western/central regions have relatively low temperatures between 29.86 °C and 35.57 °C (see Figure 4-23). In brief, both the spatial and seasonal-based results tend to indicate a decrease in V_{oc} as device temperature increases. This seems to be consistent with the common trend, where V_{oc} is drastically affected by a rise of a solar cell temperature, i.e., V_{oc} considerably decreases by an increase in cell temperature while irradiance has a minimal effect (slight increase) on it.[146]

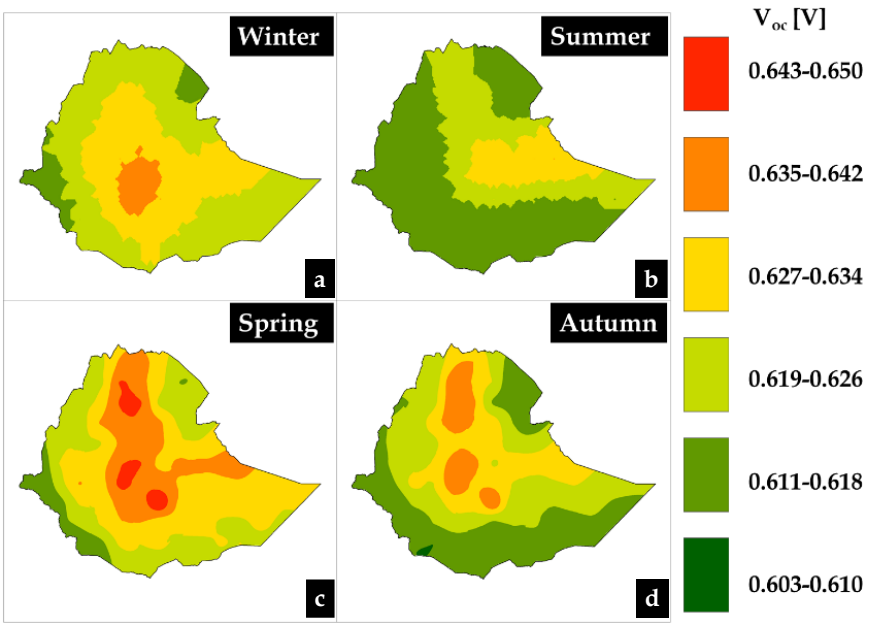

Figure 4-26: Average seasonal distribution of open circuit voltage (V_{oc} in V) over Ethiopia during winter (a), summer (b), spring (c), and autumn (d) seasons.

In each season, the relative areal coverage of the V_{oc} is also studied based on their corresponding percentage coverage. A nationwide analysis revealed that over 67% of the landmass exhibits open-circuit voltage (V_{oc}) within the range of 0.62 V to 0.63 V during the winter season. This value reduces slightly in spring, with over 66% of the regions demonstrating a V_{oc} between 0.62 V and 0.64 V. Autumn experiences a further decrease, with over 56% of the area showing a V_{oc} range of 0.62 V to 0.63 V. Summer exhibits the lowest V_{oc} values, with over 62% of the landmass recording a range of 0.61 V to 0.62 V. Here, it is worth to note that the trend V_{mp} *[V]*, over Ethiopia during the four seasons, is similar to V_{oc} as both (V_{oc} and V_{mp}) are determined in the same way. The details, including the % of coverage, are available in the Appendix in Figure A2 and Table A8 and Table A9.

D. Solar Cell Efficiency and Maximum Power (η & P_{mp})

Solar cell efficiency refers to the ratio of the power output of the device to the incident light power, and it depends on the environmental conditions including irradiance, temperature, and related issues. Figure 4-27 presents the average annual solar cell efficiency (η in %) and its corresponding maximum power output P_{mp} (in W, and $P_{mp} = V_{mp} \, x \, I_{mp}$) distribution within Ethiopia. Here, both parameters, P_{mp} and η, are controlled by the fill factor (FF) of the solar cell (average annual and seasonal FF is presented in the Appendix: Figure A13 and A14). In the northeastern and eastern/southeast parts of the country, solar cell efficiency is relatively high (~20.81-22.35%) with a P_{mp} of ~3.25-3.49 W. Conversely, the western and southwestern regions show relatively lower efficiency (~13.02-14.58%) with a P_{mp} of ~2.03-2.27 W. The higher efficiency in the northeast and east seems to be linked to the dominance of irradiance in these areas, indicated by the relatively high GSR, PSH, and POA irradiance as shown in Figures 4-20, Figure 4-21, and Figure 4-22, respectively. Here, it is important to indicate that some of the solar cell parameters will be reduced (e.g., V_{oc}) in the northeast/east, as compared to the western/southwestern parts of the country; but such an effect can be overcompensated by the significantly gained irradiance (or I_{sc}) in the eastern/northeastern regions. As an example, I_{sc} increases linearly while V_{oc} significantly decreases by the increases of irradiance and temperature, respectively. In other words, at a given location, the Sun's irradiance increases with the temperature; however, the increasing (or change) impact of J_{sc}/I_{sc} by the irradiance on device efficiency is a way far higher than the decreasing impact of temperature on V_{oc}. In brief, as presented in Figure 4-27, the increasing effect of solar irradiance, or POA irradiance, by far dominates the temperature, a hindering factor, and resulted in better device efficiency.

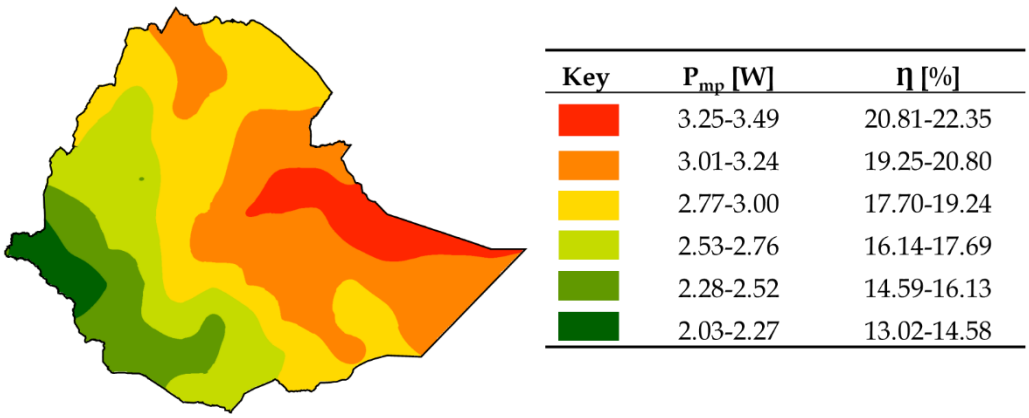

Figure 4-27: Average annual solar cell (P_{mp} in W) and efficiency (η in %) distributions over Ethiopia.

Figure 4-28 investigated the average seasonal variations in solar cell performance throughout Ethiopia, i.e., solar cell performance at different geographical locations and seasons of Ethiopia. As presented in Figure 4-28, spring showed the best solar cell efficiency of all seasons in Ethiopia. On the other hand, summer exhibited the least solar cell efficiency while winter (and then autumn) showed moderate device efficiency. This trend, the order of device efficiency in seasons, is similar to seasonal irradiance (POA irradiance) presented in Figure 4-22, and it indicates the dominancy of POA irradiance, above the other parameters, in controlling the device efficiency. In fact, during the summer months, the western/northwestern and southern/southwestern regions exhibited the lowest performance, ranging from 13.02% to 14.58%. This decline coincides with the lowest seasonal readings of POA irradiance and I_{sc} across the country. The primary causes for this seasonal lower device efficiency are likely the increased cloud cover and rainfall prevalent in these areas during summer.[142] Conversely, the northern regions experienced peak performance (23.29-25.96%) during spring. This situation too coincides with seasonal high POA irradiance and its corresponding I_{sc} trends across the nation. Overall, the annual average efficiency ranged from 13.02% to 22.35%. This strong agreement validates the observed trends in real-world performance. Thus, this study highlights the impact of seasonal variations and their range of change on solar cell performance in Ethiopia, and is vital for designing and optimizing of solar energy (PV)

across the country. Besides, the study can be element of incentives/policies, infrastructure, training on installation/maintenance, and commercialization/investment platforms in relation to site selection for energy harvesting of c-Si PV.

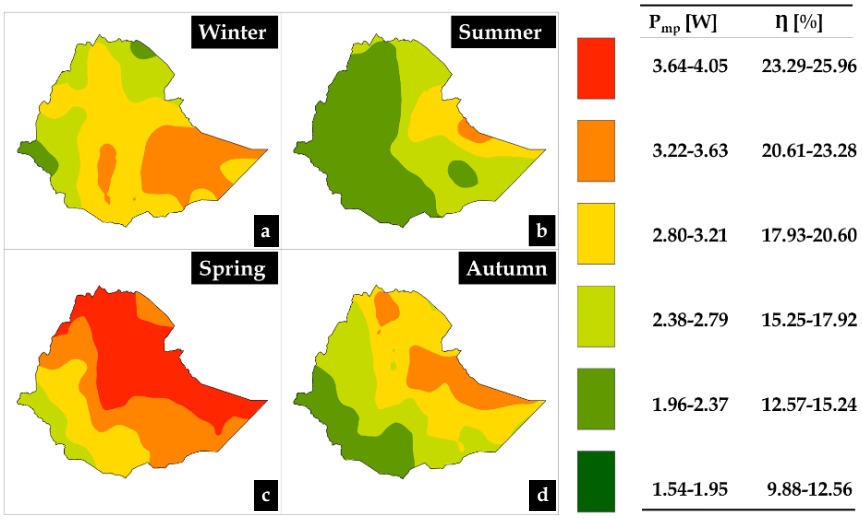

Figure 4-28: Average seasonal distribution of solar cell efficiency, η [%] over Ethiopia during winter (a), summer (b), spring (c), and autumn (d) seasons.

The relative efficiency ranges, in areal coverage at different seasons, is also studied based on their own percentage coverage (see Figure 4-28). This variation is evident in the geographical distribution of efficient landmass and the overall output levels across different seasons. Table 4-8 presents the average seasonal distribution of solar cell efficiency within the nation. As seen in Table 4-8, during winter, over 78% of the country exhibits solar cell efficiency within a narrow range of 20.28% to 22.52%, where this indicates that the major range of efficiency change is about 2.25 %. Interestingly, spring surpasses all other seasons in terms of efficiency. Here, we observed the highest seasonal output, with more than 70% of the land area registering efficiencies between 20.67% and 23.39%. Summer presents an explicit contrast, and the efficiency levels fall, with over 49% of the landmass exhibiting a significant drop to a range of 13.77% to 14.28%, i.e., it witnessed a widespread decline in solar cell performance during this season. Finally, autumn displays a moderate efficiency level, with over 55% of the landmass contributing

power within the range of 17.61% to 21.06%. This analysis highlights the substantial impact of seasonal variations on solar cell efficiency across the country, and understanding this spatial and seasonal distribution for solar energy harvesting.

Table 4-11: Average seasonal distribution of solar cell efficiency (η) and its percentage of coverage in Ethiopia.

Seasons	Values	Area [%]	Seasons	Values	Area [%]
Winter	14.14-16.10	8.21	Spring	15.47-18.09	8.70
	16.11-18.07	13.20		18.10-20.71	20.35
	18.08-20.04	31.18		20.72-23.33	33.10
	20.05-22.00	47.41		23.34-25.96	37.85
Summer	9.88-12.95	29.66	Autumn	11.73-13.99	23.91
	12.96-16.01	20.66		14.00-16.26	32.14
	16.02-19.08	28.41		16.27-18.52	23.08
	19.09-22.14	21.26		18.53-20.78	20.87

Figure 4-29 presents the weighted average seasonal POA irradiance and efficiency across the country; the Equation calculates it ($W = \sum_{i=1}^{n} w_i \eta_i / \sum_{i=1}^{n} w_i$, where; n is the number of samples to be averaged, w is the weights of the values, η is the efficiency, and W is the weighted average). As seen in Figure 4-29, the seasonal variations in solar cell efficiency across the country revealed a range of 9.88 % to 25.96 % for 0.51 to 1.12 kW/m^2 POA irradiances respectively (i.e., strongly correlates with POA irradiance). Spring exhibited the highest weighted average efficiency (22.03 %), while the lowest efficiency (15.75 %) occurred during summer. Efficiency values in winter (19.41 %) and autumn (16.99 %) were intermediate between those of summer and spring. The device performance trend of c-Si PV, seasonal/annual or location is expected to be qualitatively similar to other existing and new PV technologies, i.e., north/northeast and east/southeast are ideal for energy harvesting from a PV. In brief, as seen on Table 4-8 and or Figure 4-29, the overall efficiency of c-Si solar cells exhibits a relatively high

efficiency – ideal for a systematic PV based energy harvesting. However, challenges such as temperature, irradiance, cloud cover (seasonal effect), and the like needs to be well understood within Ethiopia.

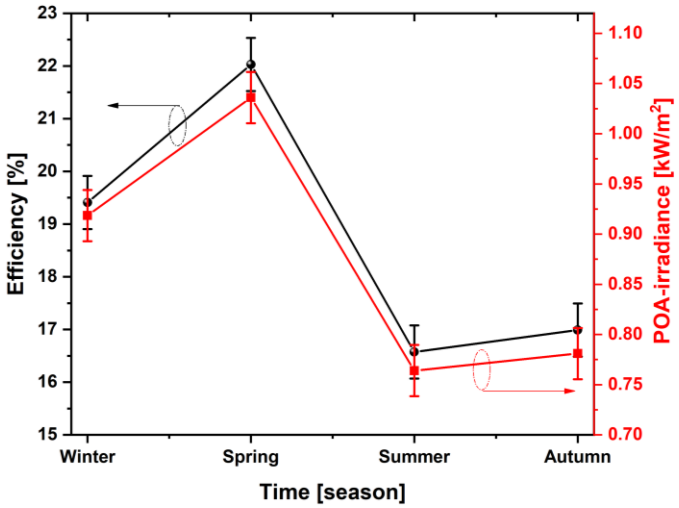

Figure 4-29: Weighted average seasonal POA irradiance and efficiency of c-Si solar cell.

4.4. The Impact of Tilt Angles and Tracking Mechanisms

The efficiency of PV systems hinges on their ability to capture and convert solar radiation into electricity. Two key factors significantly influence this performance: tilt angle and tracking mechanisms. The optimal tilt angle of a PV panel varies with geographic location and seasonal changes. By aligning panels at an angle that maximizes solar radiation exposure throughout the year, system owners can enhance energy production. This reduces energy losses due to shading and reflection, leading to improved overall efficiency. While fixed-tilt systems are simpler to install and maintain, tracking mechanisms offer a more advanced approach to optimizing solar energy capture. These systems can be categorized into single-axis and dual-axis trackers. Single-axis trackers adjust the panel angle to follow the sun's path along the east-west axis, while dual-axis trackers can rotate both horizontally and vertically, ensuring maximum solar exposure throughout the day. This section investigated the optimization of tilt angle and the implementation of various tracking mechanisms.

4.4.1. Optimum Tilt Angle

A. Monthly Optimal Tilt Angle

Figure 4-30 presents monthly distributions of the optimum tilt angle across the country. As seen in Figure 4-30, the PV module's optimum tilt angle increases with the latitude. The optimum tilt angle of the country ranges from 0^o in Jun, July, and August to 47.9^o in January. This seems to indicate that, to achieve a higher solar gain maximum tilt angle PV module/panel is required for the winter and autumn months of the year. For instance, months like January, February, December, September, October, and November. Whereas, for spring months like March, April, and May the lowest PV module/panel tilt angle seemed to be required, but for summer months like Jun, July, and August no tilting is required (likely while we took isotropic model such as Liu-Jordan model). The monthly model equations for the linear trend of optimum tilt angle as a function of latitude are presented in Table 4-9. The effect of latitude on the optimum tilt angle to achieve maximum solar gain is also reported by Aksoy *et al.,* Yunus *et al.,* and Alhamer *et al.* and the effect is qualitatively comparable to these studies.[147,148,149]

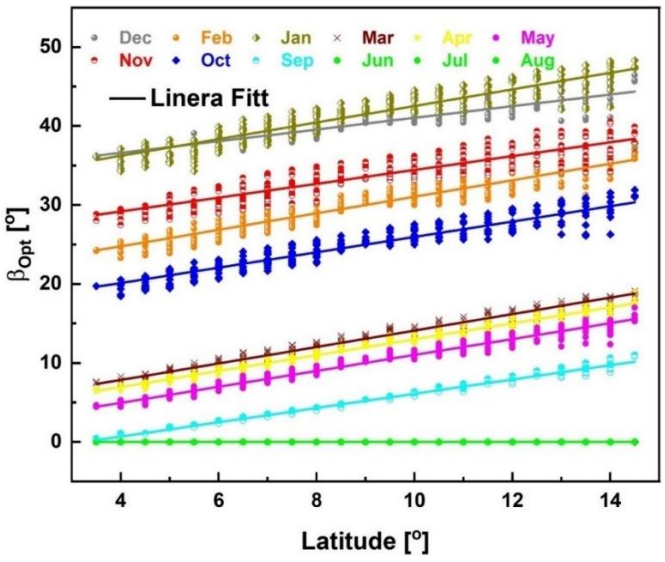

Figure 4-30: Monthly optimum tilt angle as a function of latitude [Erbs-Liu-Jordan model].

Table 4-12: Derived monthly optimum tilt angle models across the country.

Months	Equations	Months	Equations
Jan.	$\beta_{opt} = 1.05\phi + 32.04,$	Jul.	$\beta_{opt} = 0,$
Feb.	$\beta_{opt} = 1.05\phi + 20.58,$	Aug.	$\beta_{opt} = 0,$
Mar.	$\beta_{opt} = 1.04\phi + 3.68,$	Sep.	$\beta_{opt} = 0.90\phi - 2.92,$
Apr.	$\beta_{opt} = 1.01\phi + 2.93,$	Oct.	$\beta_{opt} = 0.97\phi + 16.23,$
May.	$\beta_{opt} = 1.01\phi + 0.93,$	Nov.	$\beta_{opt} = 0.88\phi + 33.6425.68,$
Jun.	$\beta_{opt} = 0,$	Dec.	$\beta_{opt} = 0.74\phi + 33.64,$

B. Seasonal Optimal Tilt Angle

Figure 4-31 presents the seasonal optimal tilt angle distribution as a function of latitude across the country. To improve the estimation of the optimum tilt angle, we incorporated anisotropic (i.e., considering diffused part of solar radiation) models alongside isotropic models. Thus, the average optimal tilt angle of all thirty (five decomposition and six transposition) model combinations ranges from 24.80-33.60^{o}, 17.53-25.77^{o}, 8.67-16.00^{o}, and 7.47-10.13^{o} for winter, autumn, spring, and summer, respectively. As presented in section 3.1A, a higher tilt angle was required in the winter compared to a lower tilt angle in the summer to achieve maximum solar gain. The seasonal model equations for the linear trend of optimal tilt angle as a function of latitude are presented in Table 6-9. Such an effect of latitude angle on optimal tilt angle is also reported by Ashetehe *et al.*, and the result is qualitatively comparable to this study.[97]

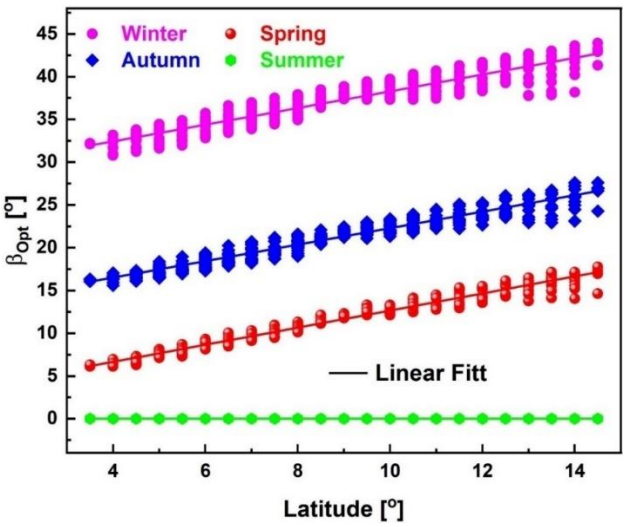

Figure 4-31: Seasonal distribution of optimal tilt angle across the country [Erbs-Liu-Jordan combination model].

Figure 4-32 illustrates, the average spatial and seasonal optimum tilt angle distribution of thirty independent combinations. As seen in Figure 4-32, analyzing optimal tilt angle models across location and seasons reveals that model selection significantly impacts on optimum tilt angle determinations. For instance, during autumn, R^2 values for optimal tilt angles varied drastically from 0.05 (DISC-Reindl) to 0.92 (Louche-Koronakis), underscoring the critical role of model choice (Appendix Table A13). Similarly, in spring, R^2 values ranged from 0.00 to 0.80, with DISC-Koronakis, Orgill-Holland-Koronakis, Orgill-Holland-Liu-Jordan, Orgill-Holland-Hay, and Louche-Koronakis consistently showing strong correlations (Appendix Table A14). Conversely, DISC and Erbs *et al.* with Liu-Jordan exhibited weak correlations. For summer, most models indicated an optimal tilt angle of zero (Appendix Table A15). However, Boland-Liu-Jordan, Boland-Steven-Unsworth, DISC-Hay, Louche-Steven-Unsworth, and Orgill-Holland-Steven-Unsworth presented weaker correlations and non-zero angles ($\beta \neq 0^o$), possibly due to an additional term for diffuse radiation coefficients in their anisotropic models. This tends to indicate that the additional term in the anisotropic model to determine the diffused radiation coefficient (F. Besharat *et al.*[150], and A.A. Ashetehe *et al.*[97]). Winter necessitated significantly larger tilt angle adjustments, evident from the

steeper slopes in winter models, emphasizing the need to account for seasonal solar patterns (Appendix Table A16). A consistent finding was that anisotropic models generally resulted in higher optimal tilt angles across all seasons. This suggests their superior ability to accurately capture complex diffuse radiation, leading to more precise estimations. Over all, the meticulous selection of appropriate model combinations is key for precise and reliable optimal tilt angle estimations, maximizing solar energy capture year-round. These findings are vital for optimizing solar energy system design and overall energy efficiency, considering specific climatic conditions and energy needs.

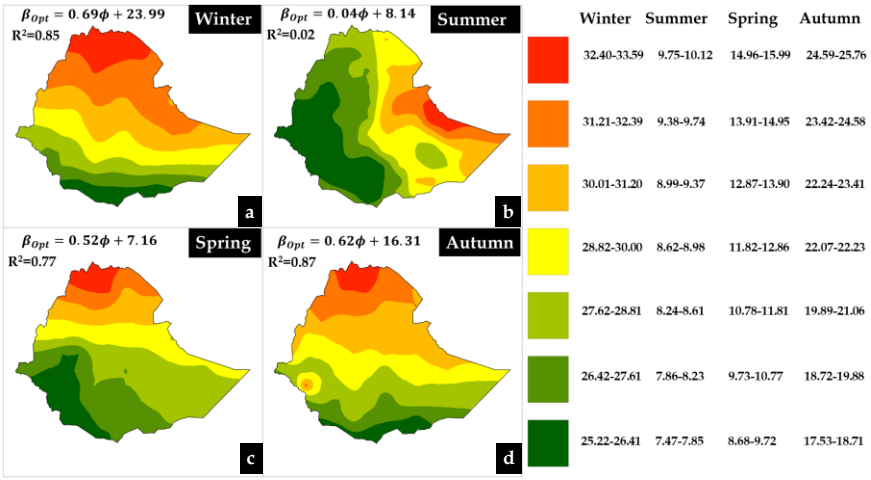

Figure 4-32: Seasonal optimal tilt angle distribution map of Ethiopia.

C. Annual Optimal Tilt Angle

Figure 4-33 presents the annual optimal tilt angle distribution of isotropic (Erbs *et al.*-Liu-Jordan) model as a function of latitude across the country. The data points that seem to scatter in Figure 4-33 are also due to longitude considerations during analysis.

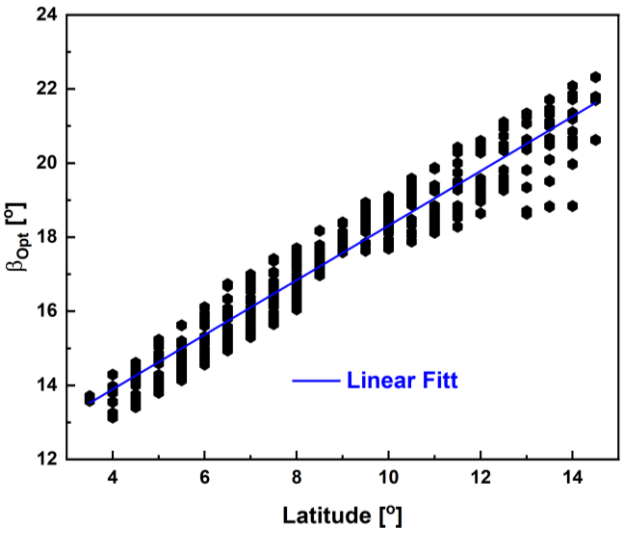

Figure 4-33: Annual distribution of optimal tilt angle across the country.

Figure 4-34 also illustrates the distribution map of average annual optimal tilt angle of thirty independent combinations across the country. As shown in Figure 4-34, the annual optimal tilt angle ranges from 14.10 to 21.53 degrees, which is 7 to 10° greater than the latitude of the site under consideration. Alhamer *et al.* also reported such a difference in optimal tilt angle as compared to the latitude of the site, and the result is qualitatively comparable.[149] The annual model equations for the linear trend of optimal tilt angle as a function of latitude for all thirty model combinations are presented in Appendix Table A17.

Likely due to country situated in the Northern Hemisphere, exhibits a well-established correlation between latitude and optimal solar panel tilt angle. Thus, regions at higher latitudes necessitate steeper panel tilts to maximize solar energy capture (see Figure 4-34). This trend is evident within the country, where areas with greater latitude require more pronounced panel inclinations for optimal solar energy harvesting. This relationship between latitude and optimal tilt angle has been documented in previous studies by A.A. Ashetehe *et al.* and Duffie *et al.*, and the findings of this study are qualitatively consistent with these earlier works.[97,151]

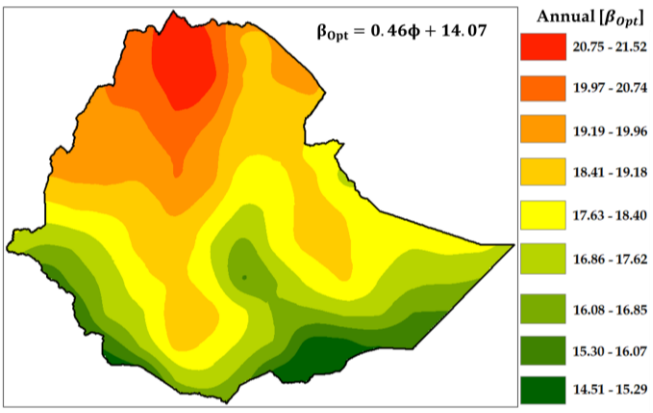

Figure 4-34: Annual optimal tilt angle distribution map of Ethiopia.

Overall, while frequent adjustments to solar PV panel tilt angles can significantly enhance energy production, the associated labor costs often outweigh the potential benefits. Numerous studies have demonstrated that less frequent adjustments, such as quarterly or annually, can still yield substantial energy gains.[152,153,154] For instance, adjusting solar PV panels four times per year can lead to energy increases ranging from 0% (during summer months) to 19.49% (during winter months) across diverse geographic locations. This approach offers a practical balance between maximizing energy output and minimizing maintenance costs. The optimal adjustment frequency is influenced by several factors, including geographic location, panel tilt, and local solar irradiance patterns. However, for most installations, quarterly or annual adjustments are generally sufficient to achieve a significant portion of the maximum possible energy yield. This finding suggests that, while frequent adjustments can provide incremental benefits, the diminishing returns on investment often outweigh the additional costs. Therefore, a well-considered adjustment schedule, tailored to specific site conditions, can optimize energy production while minimizing operational expenses.

4.4.2. PV Module Performance

A. PV module Mount at Horizontal

The seasonal performance of the horizontally faced mono-crystalline PV module is presented in Figure 4-35. As seen in Figure 4-35, the performance efficiency of the PV module reveals a seasonal variation. PV module showed the best performance during the spring season followed by winter, autumn, and summer, respectively. As a result, the efficiency of PV modules in the spring season ranges from 9.16-12.75%, whereas, 9.30-12.34%, 8.31-11.93%, and 6.88-12.06% for winter, autumn, and summer seasons, respectively. The PV module performed intermediate during the winter and autumn seasons. We also computed the landmass coverage of PV module performance to gain more details. In the spring season, over 70% of the nation experiences 10.97-12.75% PV module efficiency. In contrast, in the summer the performance of PV modules exhibits a significant drop in a range of 6.88-9.47% with over 50% landmass coverage across the nation. However, winter and autumn seasons experience intermediate performance with values ranging from 10.83-12.34% and 10.52-12.29%, which is over 55% and 67% landmass coverage, respectively as presented in Table 4-10. Such investigation highlights the substantial impact of seasonal variations on simple horizontally faced PV module performance across the nations, and understanding this spatial and seasonal distribution is vital for optimizing and/or site selection for solar energy harvesting.

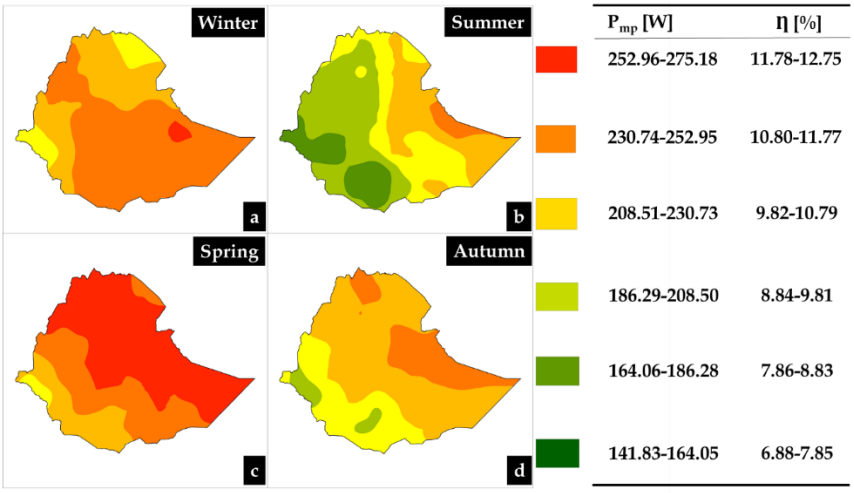

Figure 4-35: Seasonal distribution of horizontally faced PV module efficiency, η [%] over Ethiopia during winter (a), summer (b), spring (c), and autumn (d) seasons.

Table 4-13: PV module performance and landmass coverage in [%]: horizontal mount.

	Summer [Area: %]	Spring [Area: %]	Autumn [Area: %]	Winter [Area: %]
Horizontal	6.88-9.47 [50.23]	9.16-10.96 [30.82]	8.73-10.51 [32.49]	9.30-10.82 [45.01]
	9.48-12.06 [49.77]	10.97-12.75 [69.18]	10.52-12.29 [67.51]	10.83-12.34 [54.99]

B. PV Module Mount at Optimum Angle

Figure 4-36 illustrates the seasonal distribution of a mono-crystalline silicon PV module mounted at an optimum angle across the nation. As seen in Figure 4-36, the PV module showed the best performance during the winter season followed by spring, autumn, and summer, respectively. The efficiency of PV modules in the winter season ranges from 11.59-14.27%, whereas, 9.59-13.36%, 8.81-12.60%, and 6.88-12.06% for spring, autumn, and summer seasons, respectively. This seems to indicate that there is a substantial amount of solar gain due to the mounting of solar PV modules at an optimum angle. As a result, the percentage of solar gain relative to horizontally mounted solar PV modules (Figure 4-35) ranges from 0% (no gain in summer, months) to 19.49% (winter season, months) see Appendix Figure A6. During the summer season, no tilting PV module is required as we presented in section 4.3.1 B. These gains in solar energy due to mounting solar PV modules at optimum angles emphasize the importance of determining the optimum tilt angle for a certain site across the nation. We also computed the landmass coverage of PV module performance to gain more details as presented in section 4.3.2 A. In the winter season, over 70% of the nation experiences 12.94-14.27% PV module efficiency. In contrast, in the summer the performance of PV modules exhibits a significant drop in a range of 6.88-9.47% with over 50% landmass coverage across the nation (i.e., unchanged). However, spring and autumn seasons experience intermediate

performance with values ranging from 11.54-13.36% and 10.72-12.60%, which is over 69% and 58% landmass coverage, respectively as presented in Table 4-11.

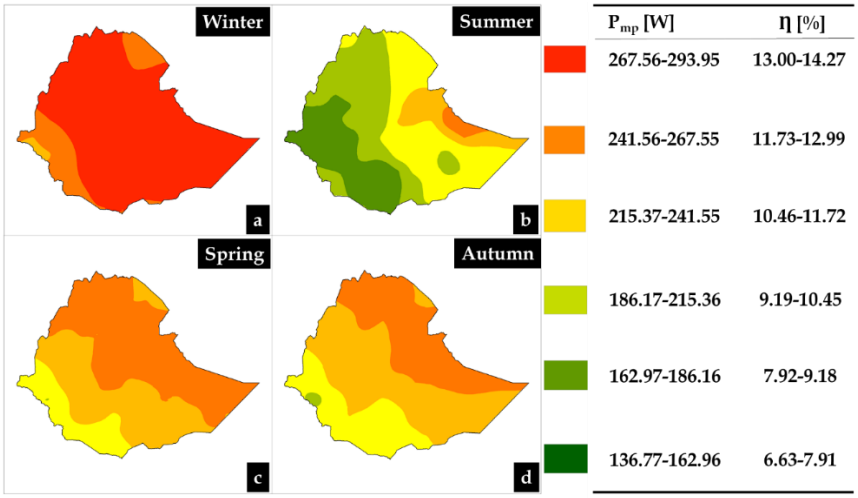

Figure 4-36: Seasonal distribution of tilted at optimum angle PV module efficiency, η [%] over Ethiopia during winter (a), summer (b), spring (c), and autumn (d) seasons.

Table 4-14: PV module performance and landmass coverage in [%]: optimum tilt angle.

	Summer [Area: %]	Spring [Area: %]	Autumn [Area: %]	Winter [Area: %]
Tilted	6.88-9.47 [50.23]	9.69-11.53 [30.28]	8.81-10.71 [41.54]	11.59-12.93 [29.55]
	9.48-12.06 [49.77]	11.54-13.36 [69.72]	10.72-12.60 [58.46]	12.94-14.27 [70.45]

4.4.3. Tracking Mechanisms

A. Vertical-axis Tracking

The seasonal performance of the vertical axis tilted at a seasonal optimum tilt angle PV module is depicted in Figure 4-37. As seen in Figure 4-37, the PV module tends to show qualitatively comparable seasonal distribution as Figure 4-36 (mounted at optimum tilt angle). However, in this instance, the performance of the PV module during the autumn season increased following winter. The efficiency of PV modules in the winter season ranges from 15.11-18.69%, whereas, 11.00-15.71%, 11.08-15.63%, and 6.88-12.06% for autumn, spring, and summer seasons, respectively. This seems to indicate that there is an increase in solar energy as a result of vertical-axis tracking. The percentage of solar gain relative to horizontally, and optimum tilt angle mounted solar PV modules (Figures 4-35 and 4-36) ranges from 0% (no gain in summer) to 56.15% (winter season) and ranges from 0% (no gain in summer) to 30.68% (winter season) see Appendix Figure A7, respectively. As we presented, no vertical-axis tracking of PV modules is required during the summer season. These gains in solar energy due to vertical-axis tracking emphasize the importance of solar tracking in addition to determining the optimum tilt angle for a certain site across the nation. We also computed the landmass coverage of PV module performance to gain more insights. In the winter season, over 64% of the nation experiences 16.91-18.69% PV module efficiency. In contrast, in the summer the performance of PV modules exhibits a significant drop in a range of 6.88-9.47% with over 50% landmass coverage across the nation (i.e., unchanged as shown in Section 4.3.2 B). However, autumn and spring seasons experience intermediate performance with values ranging from 13.36-15.71% and 13.37-15.63%, which is over 55% and 61% landmass coverage, respectively as presented in Table 4-12.

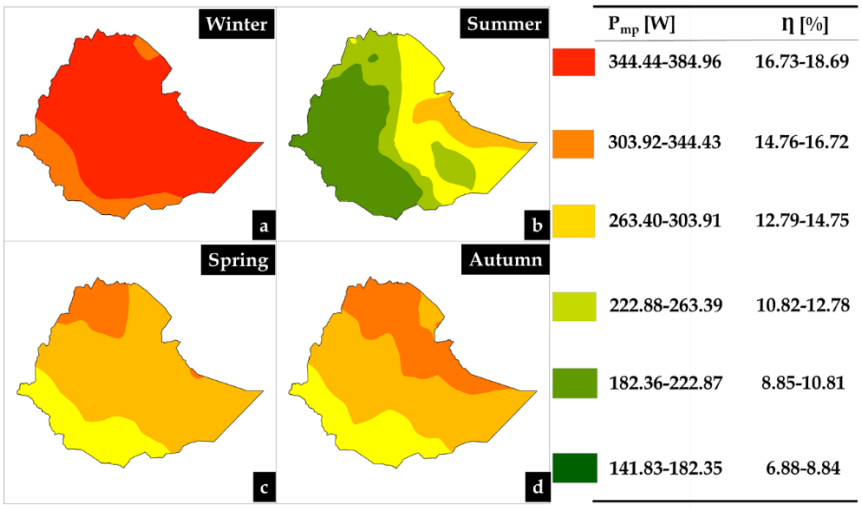

Figure 4-37: Seasonal distribution of vertically tracked PV module efficiency, η [%] over Ethiopia during winter (a), summer (b), spring (c), and autumn (d) seasons.

Table 4-15: PV module performance and landmass coverage in [%]: vertical-axis tracking.

	Summer [Area: %]	Spring [Area: %]	Autumn [Area: %]	Winter [Area: %]
Vertical	6.88-9.47 [50.23]	11.08-13.36 [38.21]	11.00-13.35 [44.10]	15.11-16.90 [35.28]
	9.48-12.06 [49.77]	13.37-15.63 [61.79]	13.36-15.71 [55.90]	16.91-18.69 [64.72]

B. East-West (EW/IEW) Tracking

Figure 4-38 presents the seasonal performance of the east-west (EW) or east-west inclined/tilted at a maximum angle (IEW) tracked PV module. As seen in Figure 4-38, adjusting the PV module at an optimum tilt angle or implementing different tracking mechanisms like (vertical-axis, and EW/IEW) made winter the leading season for PV

module performance. The efficiency of PV modules in the winter season ranges from 15.91-19.37%, whereas, 13.37-16.59%, 12.83-17.20%, and 9.82-15.44% for spring, autumn, and summer seasons. This seems to indicate that there is an increase in solar energy as a result of EW/IEW tracking. The percentage of solar gain relative to horizontally mounted PV modules: ranges from 33.36% (in summer) to 63.00% (winter season), optimum tilt angle mounted: ranges from 33.36% (in summer) to 40.22% (autumn season), and vertical-axis tracked: ranges from 4.40% (in winter) to 33.36% (summer season), see Appendix Figure A8 for better insight. In the winter season, over 66% of the nation experiences 15.05-16.99% PV module efficiency. In contrast, in the summer the performance of PV modules exhibits a significant drop in a range of 9.82-12.63% with over 50% landmass coverage across the nation. However, spring and autumn seasons experience intermediate performance with values ranging from 15.03-17.20% and 14.99-16.59%, which is over 69 and 57% landmass coverage, respectively as presented in Table 4-13.

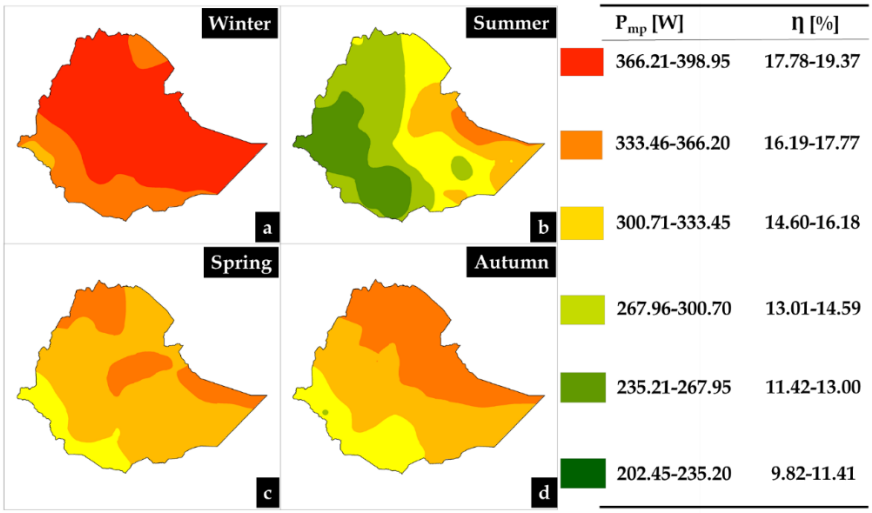

Figure 4-38: Seasonal distribution of inclined at optimum tilt angle and east-west tracked PV module efficiency, η [%] over Ethiopia during winter (a), summer (b), spring (c), and autumn (d) seasons.

Table 4-16: PV module performance and landmass coverage in [%]: EW/IEW tracking.

	Summer [Area: %]	Spring [Area: %]	Autumn [Area: %]	Winter [Area: %]
EW/IEW	9.82-12.63 [50.49]	13.37-14.98 [30.37]	12.83-15.02 [42.28]	13.10-15.04 [32.71]
	12.64-15.44 [49.51]	14.99-16.59 [69.63]	15.03-17.20 [57.72]	15.05-16.99 [66.07]

C. North-South (NS) Tracking

The effects of NS tracking mechanisms on the seasonal performance of mono-crystalline silicon PV modules are illustrated in Figure 4-39. As seen in Figure 4-39, implementing NS tracking in low-latitude countries like Ethiopia is not effective. Such an effect of latitude on the NS tracking mechanism is also reported by Bahrami *et al*., and the finding is qualitatively comparable to this study.[101] The PV modules revealed relatively best performance in the spring season for this particular tracking mechanism. The performance value ranges as follows: winter 5.84-8.29%, spring 6.42-10.70%, autumn 6.87-8.08%, and summer 5.70-8.42%. The maximum loss in solar energy relative to horizontally, mounted at optimum tilt, vertical-axis tracked, and IEW tracked were 63.00% (winter season), 40.22% (autumn season), and 33.36% (summer season), respectively see Appendix Figure A9 for better insight. In the spring season, over 56% of the nation experiences 6.42-8.56% PV module efficiency, and 7.08-8.29%, 6.87-7.47, and 5.70-7.06 covers over 64%, 51%, and 56% in winter, autumn, and summer seasons, respectively as presented in Table 4-14.

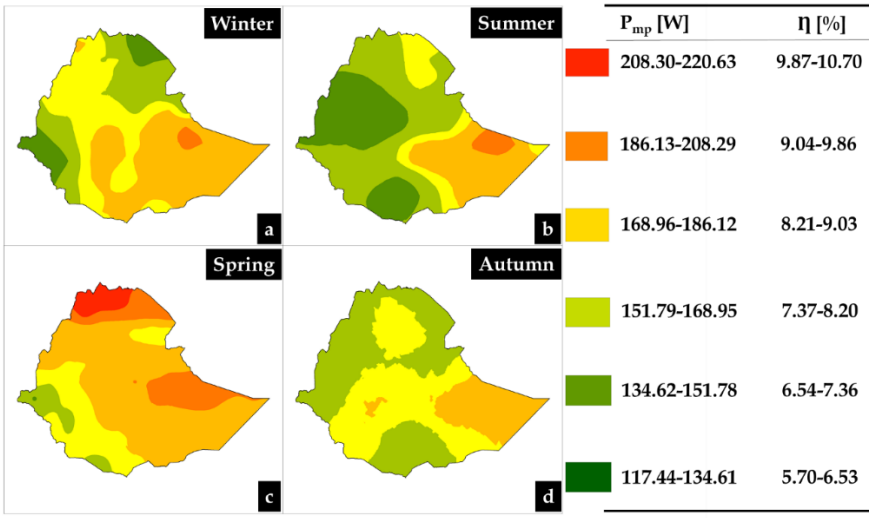

Figure 4-39: Seasonal distribution of north-south tracked PV module efficiency, η [%] over Ethiopia during winter (a), summer (b), spring (c), and autumn (d) seasons.

Table 4-17: PV module performance and landmass coverage in [%]: NS tracking.

	Summer [Area: %]	Spring [Area: %]	Autumn [Area: %]	Winter [Area: %]
N-S Tracking	5.70-7.06 [56.26]	6.42-8.56 [56.78]	6.87-7.47 [51.62]	5.84-7.07 [35.30]
	7.07-8.42 [43.74]	8.57-10.70 [43.22]	7.48-8.08 [48.38]	7.08-8.29 [64.70]

D. Dual-axis or Full Tracking (DAT)

Figure 4-40 presents the seasonal performance of the full/dual-axis tracked PV module. As seen in Figure 4-40, adjusting the PV module at an optimum tilt angle or implementing different tracking mechanisms (like vertical-axis, EW/IEW, and full/dual-axis) made winter the leading season for PV module performance. The efficiency of PV modules in the winter season ranges from 15.91-19.37%, whereas, 13.69-16.99%, 12.82-17.27%, and 10.29-15.82% for spring, autumn, and summer seasons. This seems to indicate that there is an increase in solar energy as a result of dual-axis tracking relative

to other tracking mechanisms. The maximum gain in solar energy relative to horizontally, mounted at optimum tilt, vertical-axis tracked, IEW tracked, and NS tracked were 62.99% (winter season), 40.26% (autumn season), 37.71% (summer season), and 14.64% (in winter), respectively see Figure 4-40 for better insight. There is no significant gain in solar energy was observed between dual-axis and EW/IEW tracking mechanisms, particularly for the winter and autumn seasons (seen in Appendix Figure A10). This seems to suggest that the EW/IEW tracking mechanisms nearly perform as dual/full tracking across the nation. During the winter season, over 66% of the nation experiences 17.65-19.37% PV module efficiency, and 15.35-16.99%, 15.02-17.27%, and 10.26-13.04% covers over 70%, 57%, and 51% of landmass in spring, autumn, and summer seasons, respectively as presented in Table 4-15.

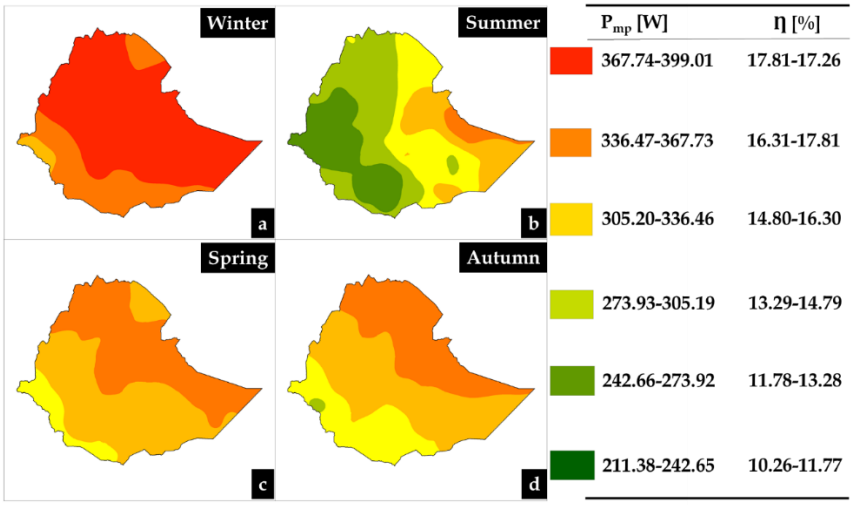

Figure 4-40: Seasonal distribution of dual-axis tracked PV module efficiency, η [%] over Ethiopia during winter (a), summer (b), spring (c), and autumn (d) seasons.

Table 4-18: PV module performance and landmass coverage in [%]: Dual tracking.

	Summer [Area: %]	Spring [Area: %]	Autumn [Area: %]	Winter [Area: %]
Dual-tracking	10.26-13.04 [51.64]	13.69-15.34 [30.24]	12.82-15.01 [42.39]	15.91-17.64 [33.78]

	13.05-15.82 [48.36]	15.35-16.99 [69.76]	15.02-17.27 [57.61]	17.65-19.37 [66.22]

E. Annual Performance

The cumulative annual PV module performance for the whole implemented tracking mechanism is depicted in Figure 4-41. The annual performance efficiency of PV modules for each tracking mechanism ranges as follows: for horizontally mounted (8.73-12.29%), for optimum tilt angle (9.12-12.78%), vertical-axis tracked (11.09-15.18%), for EW/IEW tracked (13.10-16.99%), for NS tracked (6.34-8.70%), and dual/full tracked (13.27-17.19%). As seen in Figure 4-41, the PV module/panel implemented with dual/full tracking showed the best annual performance, and EW/IEW tracked took the second rank. The annual solar energy gain in percent due to dual/full tracking compared to other ranges from 1.22 % (EW/IEW) to 50.62% (NS) across the nation. As a result, EW/IEW showed comparatively close performance with dual/full tracking mechanisms. This seems to indicate that implementing the yearly optimum tilt angle of south faced PV module/panel to EW/IEW tracking is ideal and knowing the specific annual optimum tilt angle of IEW might not be required. To get further insight, as usual, we calculated the performance of each tracking mechanism with its land mass coverage as illustrated in Table 4-16. In addition, the performance of each tracking mechanism relative to the horizontally mounted PV module was also presented in Figure 4-42.

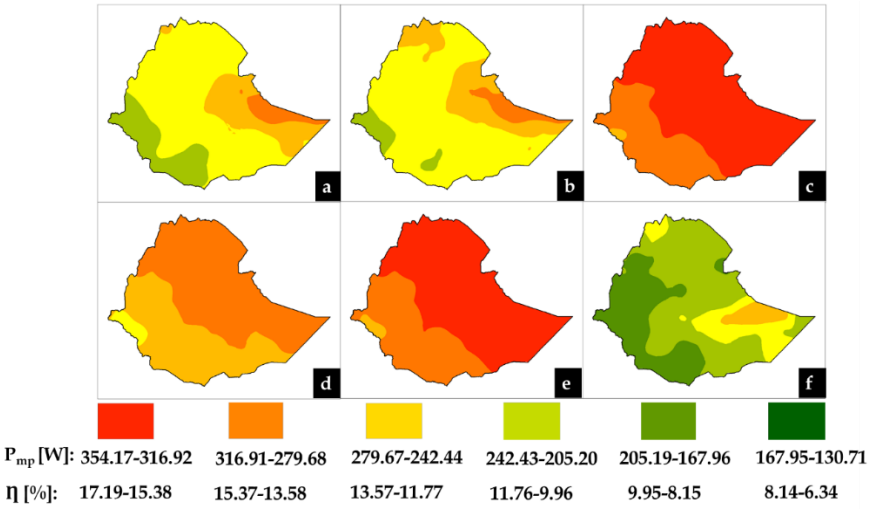

Figure 4-41: Annual distribution of PV module efficiency η [%] for all implemented mechanisms across the country, horizontally mounted (a), mounted at optimum tilt angle (b), dual/full tracked (c), vertical-axis tracked (d), EW/IEW tracked (e), and NS tracked (f).

Table 4-19: PV module performance and landmass coverage in [%]: Annual.

Horizontal	8.73-9.32	9.33-9.92	9.93-10.51	10.52-11.11	11.12-11.70	11.71-12.29
Area [%]	3.9	14.69	13.9	30.45	24.44	12.62
Opt_Angle	9.12-9.73	9.74-10.34	10.35-10.95	10.96-11.56	11.57-12.17	12.18-12.78
Area [%]	3.69	14.67	13.99	25.16	28.49	14
DAT	13.27-13.92	13.93-14.58	14.59-15.23	15.24-15.88	15.89-16.54	16.55-17.19
Area [%]	5.81	13.43	13.63	23.96	28.64	14.52
V-axis	11.09-11.77	11.78-12.45	12.46-13.13	13.14-13.81	13.82-14.50	14.51-15.18
Area [%]	13.87	10.84	16.77	22.54	20.86	15.13
EW/IEW	13.10-13.75	13.76-14.40	14.41-15.04	15.05-15.69	15.70-16.34	16.35-16.99
Area [%]	6.00	13.19	13.52	23.73	28.69	14.87
NS	6.34-6.73	6.74-7.13	7.14-7.52	7.53-7.91	7.92-8.31	8.32-8.70
Area [%]	5.21	16.24	28.62	18.83	22.4	8.69

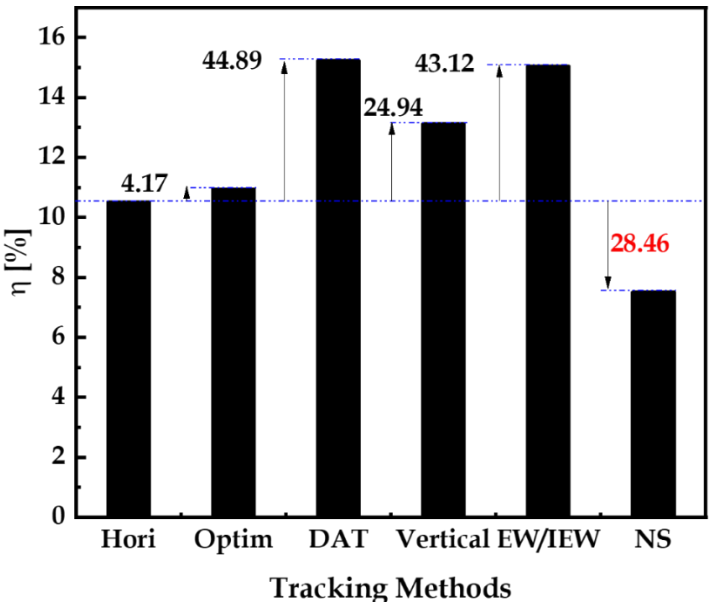

Figure 4-42: Annual solar energy gain for different implemented mechanisms relative to horizontally mounted solar PV module/panel.

Chapter 5

5. Conclusions and Recommendations

5.1. Conclusions

This study rigorously evaluated solar irradiance prediction and PV performance across Ethiopia, employing advanced ML techniques and detailed spatiotemporal analysis, alongside implementing various performance optimization techniques. A stacked ensemble ML model demonstrated superior accuracy in predicting solar irradiance across hourly, daily, and monthly timescales, evidenced by high coefficients of determination (R^2 values ranging from 0.956 to 0.963) and low root mean square errors (RMSE values ranging from 9.938 to 11.784 W/m^2). The study elucidated the spatiotemporal variability of solar radiation, revealing seasonal fluctuations with peak irradiance during spring and winter, and minima during summer. This variability directly impacted c-Si PV cell performance, with significant spatial and temporal disparities observed in POA irradiance. Higher POA irradiance, peaking during spring and winter in the northern and eastern regions, correlated with increased J_{sc}. Conversely, V_{oc} exhibited an inverse relationship with temperature, resulting relatively higher values in cooler regions. Solar cell efficiency varied substantially, ranging from 13.02% to 22.35%, with the northern and eastern regions and the spring season demonstrating the highest average efficiencies. Furthermore, the study determined optimal PV module tilt angles, demonstrating a latitude-dependent relationship by combining five decomposition and six transposition models (i.e., total of thirty different combinations). The derived model equations facilitated precise tilt angle adjustments for varying timescales. Consequently, the seasonal optimal tilt angle varies from 8.68-15.99^o, 25.22-33.59^o, 17.53-25.76^o, and 7.47-10.12^o for spring, winter, autumn, and summer, respectively. The annual optimum tilt angle also varies from 14.51-21.52^o, i.e., ~ 7-10^o higher than the latitude of the location. In addition, the study incorporates different tracking mechanisms, including dual-axis, vertical-axis, east-west/inclined east-west

(EW/IEW), and north-south (NS) tracking, revealed significant energy gains compared to horizontally mounted modules. Dual-axis tracking exhibited the highest annual average efficiency (15.23%), while NS tracking resulted in a performance reduction. Overall, this study provides a comprehensive assessment of solar resource availability to evaluate c-Si PV performance in Ethiopia. The high predictive accuracy of the stacked ensemble ML model, coupled with detailed spatiotemporal analysis, enables improved solar energy resource assessment and forecasting. The identified spatial and temporal variations in PV performance, influenced by POA irradiance, temperature, optimum tilt angles, and implementing different tracking mechanisms, are crucial for strategic site selection and deployment of PV systems. The demonstrated efficacy of advanced tracking mechanisms, particularly dual-axis tracking, highlights their potential for enhancing solar energy harvesting efficiency. These findings contribute to the advancement of PV-based energy solutions in Ethiopia, facilitating informed decision-making for sustainable energy development.

5.2. Recommendations

This study highlights some scientific points as future outlook:

- **Temporal Data Expansion:** Future research should utilize long-term datasets exceeding ten years to enhance model robustness in capturing extended solar radiation variability.
- **Architectural Exploration:** Investigating advanced machine learning (ML) and deep learning (DL) architectures, such as convolutional neural networks (CNNs) for weather pattern recognition, is recommended to potentially improve solar radiation prediction accuracy.
- **PV Efficiency Parameterization:** Future models should incorporate physical factors such as dust, shading, humidity, and other parameters to represent more accurate real-world photovoltaic (PV) performance.

- **Regional Optimization Analysis:** Regional variations in optimal tilt angles and tracking mechanisms should be investigated to address climate, topography, and land use differences within Ethiopia.

References

1. M. Iqbal, *An introduction to solar radiation*. Elsevier, (2012).
2. L. Wald, *Fundamentals of solar radiation*. CRC Press (2021).
3. V. Badescu, Modeling solar radiation at the earth's surface. *SpringerVerlag, Berlin/Heidelberg, (*2008*)*.
4. J. Twidell, *Renewable energy resources*. Routledge (2021).
5. J. Kleissl, *Solar energy forecasting and resource assessment*. Academic Press (2013).
6. J. Nelson; The physics of solar cells. *World Scientific Publishing Company*, *2*, (2003).
7. M. Peplow, *A new kind of solar cell is coming: is it the future of green energy*?, Nature, 623, 902 (2013).
8. X. Wang, X. Tian, X. Chen, L. Ren, and C. Geng, A review of end-of-life crystalline silicon solar photovoltaic panel recycling technology. *Sol. Energy Mater. Sol. Cells*, *248*, 111976 (2022).
9. M. Di Sabatino, R. Hendawi, and A.S. Garcia, Silicon Solar Cells: Trends, Manufacturing Challenges, and AI Perspectives. *Crystals*, *14*(2), (2024).
10. P. R. Dias, L. Schmidt, N. L. Chang, M. M. Lunardi, R. Deng, B. Trigger, L. B. Gomes, R. Egan, and H. Veit, High yield, low cost, environmentally friendly process to recycle silicon solar panels: Technical, economic and environmental feasibility assessment. *Renew. Sust. Energ.*, *169*, (2022).
11. A. Goetzberger, and C. Hebling, Photovoltaic materials, past, present, future. *Sol. Energy Mater. Sol. Cells*, *62*(1-2), (2000).
12. L. M. Shaker, A. A. Al-Amiery, M. M. Hanoon, W. K. Al-Azzawi, and A. A. H. Kadhum, Examining the influence of thermal effects on solar cells: a comprehensive review. *Sustainable Energy Research*, *11*(1), p.6 (2024).
13. M. M. Fouad, L. A. Shihata, and E. I. Morgan, An integrated review of factors influencing the perfomance of photovoltaic panels. *Renewable and Sustainable Energy Reviews*, *80*, pp.1499-1511, (2017).
14. O. Bamisile, C. Acen, D. Cai, Q. Huang, and I. Staffell, The environmental factors affecting solar photovoltaic output. *Renewable and sustainable energy reviews*, *208*, p.115073, (2025).

15. A. Karafil, H. Ozbay, and M. Kesler, Temperature and solar radiation effects on photovoltaic panel power. *Journal of New Results in Science*, *5*, pp.48-58, (2016).
16. M. Q. Raza, M. Nadarajah, and C. Ekanayake, On recent advances in PV output power forecast. *Solar Energy*, *136*, pp.125-144, (2016).
17. M. ed. Aghaei, *Solar Radiation: Measurement, Modeling and Forecasting Techniques for Photovoltaic Solar Energy Applications*. BoD–Books on Demand, (2022).
18. N. S. Chukwujindu, A comprehensive review of empirical models for estimating global solar radiation in Africa. *Renewable and sustainable energy reviews*, *78*, pp.955-995, (2017).
19. F. Besharat, A. A. Dehghan, and A. R. Faghih, Empirical models for estimating global solar radiation: A review and case study. *Renewable and sustainable energy reviews*, *21*, pp.798-821, (2013).
20. A. Khair, L. M. Putranto, and D. D. Arianandа, Time Series Analysis for Solar Irradiance Forecasting: A Systematic Review. In *2025 15th International Conference on Electrical Engineering (ICEENG)* (pp. 1-6). IEEE, (2025).
21. A. E. Gürel, Ü. Ağbulut, H. Bakır, A. Ergün, and G. Yıldız, A state of art review on estimation of solar radiation with various models. *Heliyon*, *9*(2), (2023).
22. L. Huang, J. Kang, M. Wan, L. Fang, C. Zhang, and Z. Zeng, Solar radiation prediction using different machine learning algorithms and implications for extreme climate events. *Frontiers in Earth Science*, *9*, p.596860, (2021).
23. B. Brahma, and R. Wadhvani, Solar irradiance forecasting based on deep learning methodologies and multi-site data. *Symmetry*, *12*(11), p.1830, (2020).
24. E. O. Yuzer and A. Bozkurt, Deep learning model for regional solar radiation estimation using satellite images. *Ain Shams Engineering Journal*, *14*(8), p.102057, (2023).
25. T. Zhu, Y. Guo, Z. Li, and C. Wang, Solar radiation prediction based on convolution neural network and long short-term memory. *Energies*, *14*(24), p.8498, (2021).
26. H. Kim, S. Park, H. J. Park, H. G. Son, and S. Kim, Solar radiation forecasting based on the hybrid CNN-CatBoost model. *Ieee Access*, *11*, pp.13492-13500, (2023).
27. M. Lave, W. Hayes, A. Pohl, and C.W. Hansen, Evaluation of global horizontal irradiance to plane-of-array irradiance models at locations across the United States. *IEEE journal of Photovoltaics*, *5*(2), pp.597-606, (2015).

28. T. Mekonnen, R. Bhandari, and V. Ramayya: Modeling, analysis and optimization of grid-integrated and islanded solar PV systems for the Ethiopian residential sector: Considering an emerging utility tariff plan for 2021 and beyond. *Energies*, *14*(11), (2021).
29. A. B. Mulatu, W. A. Negash, and M. Teshome, The Status of Solar Energy Utilization and Development in Ethiopia. *Am. J. Appl. Sci. Res.*, *9*(3), (2023).
30. Q. Hassan, P. Viktor, T. J. Al-Musawi, B. M. Ali, S. Algburi, H. M. Alzoubi, A. K. Al-Jiboory, A. Z. Sameen, H. M. Salman, and M. Jaszczur, The renewable energy role in the global energy Transformations. *Renew. Energy Focus*, *48*, (2024).
31. A. A. Adenle, Assessment of solar energy technologies in Africa-opportunities and challenges in meeting the 2030 agenda and sustainable development goals. *Energy Policy*, *137*, (2020).
32. L. L. Nathans, F.L. Oswald, and K. Nimon, *Interpreting multiple linear regression: a guidebook of variable importance.* Practical assessment, research & evaluation, **17**(9), 9, (2012).
33. A. K. Yadav, & S. S. Chandel, Solar radiation prediction using Artificial Neural Network techniques: A review. *Renewable and sustainable energy reviews*, *33*, 772-781 (2014).
34. Z. Deng, Z. Xiaoshu, C. Debo, Z. Ming, Z. Shichao, Efficient kNN classification algorithm for big data, *Neurocomputing*, **195**, 143-148 (2016).
35. M.A. Friedl, and C.E. Brodley, Decision tree classification of land cover from remotely sensed data, *Remote Sensing of Environment*, **61**(3), 399-409 (1997).
36. C. J. Burges, A tutorial on support vector machines for pattern recognition, *Data Mining and Knowledge Discovery*, **2**(2), 121-167 (1998).
37. T. Hastie, J. Zhu, S. Rosset, and H. H. Zou, "*Multi-class AdaBoost,*", Tech. Rep., Department of Statistics, University of Michigan, Ann Arbor, MI 48109, (2006).
38. J. Fan, X. Wang, L. Wu, H. Zhou, F. Zhang, X. Yu, X. Lu & Y. Xiang, Comparison of Support Vector Machine and Extreme Gradient Boosting for predicting daily global solar radiation using temperature and precipitation in humid subtropical climates: A case study in China. *Energy conversion and management*, *164*, 102-111, (2018).
39. T. Kapwata, and M.T. Gebreslasie, *Random Forest variable selection in spatial malaria transmission modelling in Mpumalanga Province, South Africa.* Geospatial health, **11**(3), (2016).

40. J. Park, M. Jihoon, J. Seungmin, H. Eenjun, Multistep-ahead solar radiation forecasting scheme based on the light gradient boosting machine: A case study of Jeju Island. *Remote Sensing*, **12**(14), 2271, (2020).
41. J. Huang, and M. Perry, A semi-empirical approach using gradient boosting and k-nearest neighbors' regression for GEFCom2014 probabilistic solar power forecasting, *Int. J. Forecasting*, **32**(3), 1081-1086 (2016).
42. M. Golam, A. Rubina, L. Jae-Min, K. D. -Seong, A long short-term memory-based solar irradiance prediction scheme using meteorological data, *IEEE Geoscience and Remote Sensing Letters*, **19**, 1-5, (2021).
43. H. -Y. Cheng, C. -C. Yu, and C. -L. Lin, Day-ahead to week-ahead solar irradiance prediction using convolutional long short-term memory networks, *Renewable Energy*, **179**, 2300-2308, (2021).
44. A. Gedifew, A. Benor, Evaluating the Impact of Tilt Angles and Tracking Mechanisms on Photovoltaic Modules in Ethiopia. *Front. Energy Res.*, *12*, (2025).
45. D. G. Erbs, S.A. Klein, J.A. Duffie, Estimation of the diffuse radiation fraction for hourly, daily, and monthly-average global radiation. Sol. Energy 28, (1982).
46. E. L. Maxwell, *A quasi-physical model for converting hourly global horizontal to direct normal insolation* (No. SERI/TR-215-3087). Solar Energy Research Inst., Golden, CO (USA), (1987).
47. J. Boland, J. Huang, and B. Ridley, Decomposing global solar radiation into its direct and diffuse components. *Renewable and Sustainable Energy Reviews*, *28*, (2013).
48. A. Louche, G. Notton, P. Poggi, G. Simonnot, Correlation for direct normal and global horizontal irradiations on a French Mediterranean site. Solar Energy, 46(4), (1991).
49. J. F. Orgill, K.G.T. Hollands, Correlation equation for hourly diffuse radiation on a horizontal surface. Solar Energy (1977).
50. B. Y. H. Liu, R.C. Jordan, The interrelationship and characteristic distribution of direct, diffuse and total solar radiation. Solar Energy; 4(3), (1960).
51. V. Badescu, "A new kind of cloudy sky model to compute instantaneous values of diffuse and global solar irradiance," Theoretical and Applied Climatology, vol. 72, no. 1-2, (2002).
52. P. S. Koronakis, "On the choice of the angle of tilt for south facing solar collectors in the Athens basin area," Solar Energy, vol. 36, no. 3, (1986).

53. D. T. Reindl, W. A. Beckman, and J. A. Duffie, "Evaluation of hourly tilted surface radiation models," Solar Energy, vol. 45, no. 1, (1990).
54. J. E. Hay, "Calculation of monthly mean solar radiation for horizontal and inclined surfaces," Solar Energy, vol. 23, no. 4, (1979).
55. M. D. Steven and M. H. Unsworth, "The angular distribution and interception of diffuse solar radiation below overcast skies," Quarterly Journal of the Royal Meteorological Society, vol. 106, no. 447, (1980).
56. N.E. Benti, A.B. Aneseyee, A.A. Asfaw, C.A. Geffe, G.A. Tiruye, and Y.S. Mekonnen, Estimation of global solar radiation using sunshine-based models in Ethiopia. *Cogent Engineering*, ***9***(1), p.2114200 (2022).
57. D. Gielen, F. Boshell, D. Saygin, M. D. Bazilian, N. Wagner, and R. Gorini, The role of renewable energy in the global energy transformation. *Energy strategy reviews*, *24*, (2019).
58. A. O. Maka, T. Ghalut, and E. Elsaye, The pathway towards decarbonisation and net-zero emissions by 2050: The role of solar energy technology. *Green Technologies and Sustainability*, *2*(3), (2024).
59. M. Lackner, B. Sajjadi, and W. Y. eds. Chen, *Handbook of climate change mitigation and adaptation*. Cham, Switzerland: Springer, (2022).
60. D.I. Stern, and A. Kander; The role of energy in the industrial revolution and modern economic growth. *The Energy Journal*, *33*(3), (2012).
61. G. Mombekova, M. Nurgabylov, A. Baimbetova, B. Keneshbayev, and B. Izatullayeva; The relationship between energy consumption, population and economic growth in developing countries. *International Journal of Energy Economics and Policy*, *14*(3), (2024).
62. International Energy Agency (IEA). *World Energy Outlook (2024)*.
63. K.O. Yoro, and M.O. Daramola, CO2 emission sources, greenhouse gases, and the global warming effect. In *Advances in carbon capture*. Woodhead Publishing (2020).
64. R. Hannah and R. Pablo - "Energy Mix" Published online at OurWorldinData.org (2020). Retrieved from: 'https://ourworldindata.org/energy-mix'.
65. L. Liu; Comment on 'recent progress in thermodynamics of radiation-exergy of radiation, effective temperature of photon and entropy constant of photon'. Sci China, Ser E Technol Sci. ;52, (2009).

66. ASBM. Shah, H. Yokoyama N. Kakimoto; High- precision fore casting model of solar irradiance based on grid point value data analysis for an efficient photovoltaic system. IEEE Trans Sustain Energy; 6(2), (2015).
67. Renewable energy: sustainable energy concepts for the fu ture. Choice Rev Online; 46(05), (2009).
68. Development and Climate Change. Dev. Clim. Chang.; (2008).
69. E. Asmelash, G. Prakash, R. Gorini, and D. Gielen; Role of IRENA for global transition to 100% renewable energy. *Accelerating the transition to a 100% renewable energy era*, (2020).
70. A. Jäger-Waldau, Snapshot of photovoltaics− May 2023. *EPJ Photovoltaics*, *14*, (2023).
71. Africa's solar energy potential burns bright [WWW Document], The solar revolution in Africa, (2017).
72. A.A. Adenle; Assessment of solar energy technologies in Africa opportunities and challenges in meeting the 2030 agenda and sustainable development goals. *Energy Policy* 137, (2020).
73. L. Zhao, W. Wang, L. Zhu, Y. Liu, A. Dubios; Economic analysis of solar energy development in North Africa. *Global Energy Interconnect*. 1, (2018).
74. A. Rachid, and N. NAJMI, A review on the present and future of solar power in Africa, (2024).
75. M. K. Abdelrazik, S.E. Abdelaziz, M.F. Hassan, and T.M. Hatem; Climate action: Prospects of solar energy in Africa. *Energy Reports*, *8*, (2022).
76. T. Dewi, P. Risma, Y. Oktarina; A review of factors affecting the efficiency and output of a PV system applied in tropical climate. *IOP Conf Ser Earth Environ Sci*.; 258 (2019).
77. K. Hasan, S.B. Yousuf, M.S.H.K. Tushar, B.K. Das, P. Das, and M.S. Islam; Effects of different environmental and operational factors on the PV performance: A comprehensive review. *Energy Science & Engineering*, *10*(2), (2022).
78. P. Dwivedi, K. Sudhakar, A. Soni, E. Solomin, and I. Kirpichnikova, Advanced cooling techniques of PV modules: A state of art, Case Stud. *Therm. Eng.* 21 (2020).
79. M. Hasanuzzaman, A.B.M.A. Malek, M.M. Islam, A.K. Pandey, and N.A. Rahim; Global advancement of cooling technologies for PV systems: A review. *Solar Energy*, *137*, (2016).

80. L. Wang, O. Kisi, M. Zounemat-Kermani, G.A. Salazar, Z. Zhu, W. Gong; Solar radiation prediction using different techniques: model evaluation and comparison, Renew. Sustain. Energy Rev. 61 (2016).
81. Global Atlas, Available online: URL: https://globalsolaratlas.info/download/world, 2022.
82. O. A. Karaman, T. T. A˘ gır, ˙ I. Arsel; Estimation of solar radiation using modern methods, *Alex. Eng. J.* 60 (2) (2021).
83. Ü. A˘ gbulut, A.E. Gürel, Y. Biçen; Prediction of daily global solar radiation using different machine learning algorithms: evaluation and comparison, *Renew. Sustain. Energy Rev.* 135 (2021).
84. P. Bouquet, I. Jackson, M. Nick, and A. Kaboli, AI-based forecasting for optimised solar energy management and smart grid efficiency. *International Journal of Production Research*, *62*(13), (2024).
85. H. Alkahtani, T.H. Aldhyani, and S.N. Alsubari; Application of artificial intelligence model solar radiation prediction for renewable energy systems. *Sustainability*, *15*(8), (2023).
86. S. Zaim, M. El Ibrahimi, A. Arbaoui, A. Samaouali, M. Tlemcani, and A. Barhdadi; Using artificial intelligence for global solar radiation modeling from meteorological variables. *Renewable Energy*, *215*, (2023).
87. A. Mellit; Artificial Intelligence technique for modelling and forecasting of solar radiation data: a review. *International Journal of Artificial intelligence and soft computing*, *1*(1), (2008).
88. M. Soori, B. Arezoo, and R. Dastres, Artificial intelligence, machine learning and deep learning in advanced robotics, a review. *Cognitive Robotics*, *3*, (2023).
89. G. E. Batista, and M. C. Monard, An analysis of four missing data treatment methods for supervised learning. *Applied artificial intelligence*, *17*(5-6), (2003).
90. E. S. Solano, and C. M. Affonso, Solar irradiation forecasting using ensemble voting based on machine learning algorithms. *Sustainability*, *15*(10), (2023).
91. F. A. Ramírez-Rivera, and N. F. Guerrero-Rodríguez, Ensemble Learning Algorithms for Solar Radiation Prediction in Santo Domingo: Measurements and Evaluation. *Sustainability*, *16*(18), (2024).
92. A. E. Gürel, Ü. Ağbulut, H. Bakır, A. Ergün, and G. Yıldız, A state of art review on estimation of solar radiation with various models. *Heliyon*, *9*(2), (2023).

93. Z. Dong, D. Yang, T. Reindl, W.M. Walsh, A novel hybrid approach based on self-organizing maps, support vector regression and particle swarm optimization to forecast solar irradiance, *Energy* 82 (2015).
94. F. M. Daniel-Durandt, and A.J. Rix, New Decomposition Models for Hourly Direct Normal Irradiance Estimations for Southern Africa. In *Solar* (Vol. 4, No. 2), *MDPI*, (May, 2024).
95. M. Lave, W. Hayes, A. Pohl, and C.W. Hansen, Evaluation of global horizontal irradiance to plane-of-array irradiance models at locations across the United States. *IEEE journal of Photovoltaics*, *5*(2), (2015).
96. S. Pelland, G. Galanis, and G. Kallos; Solar and photovoltaic forecasting through post-processing of the Global Environmental Multiscale numerical weather prediction model. *Progress in photovoltaics: Research and Applications*, *21*(3), (2013).
97. A. A. Ashetehe, B.B. Gessesse, and F. Shewarega, Development of optimal tilt angle models of a photovoltaic module for maximum power production: Ethiopia. *International Journal of Photoenergy*, (1), (2022).
98. Y. Zhu, J. Liu, and X. Yang, Design and performance analysis of a solar tracking system with a novel single-axis tracking structure to maximize energy collection. *Applied Energy*, *264*, (2020).
99. A. Senpinar, M. Cebeci; Evaluation of power output for fixed and two-axis tracking pvarrays. *Appl Energy* 92, (2012).
100. T. P. Chang, Performance study on the east-west oriented single-axis tracked panel. *Energy* 34(10), (2009).
101. A. Bahrami, C.O. Okoye, and U. Atikol, The effect of latitude on the performance of different solar trackers in Europe and Africa. *Applied energy*, *177*, (2016).
102. Z. Li, X. Liu, R.Tang, Optical performance of vertical single-axis tracked solar panels. Renew Energy 36(1), (2011).
103. T.P. Chang, The gain of single-axis tracked panel according to extraterrestrial ra diation. *Appl Energy* 86(7–8), (2009).
104. C. O. Okoye, A. Bahrami, and U. Atikol, Evaluating the solar resource potential on different tracking surfaces in Nigeria. *Renewable and Sustainable Energy Reviews*, *81*, (2018).
105. P. Singh, and N. M. Ravindra, Temperature dependence of solar cell performance—an analysis. *Solar energy materials and solar cells*, *101*, (2012).

106. A. Q. Malik, and S.J.B.H. Damit, Outdoor testing of single crystal silicon solar cells. *Renewable energy*, *28*(**9**), (2003).
107. C. Cui, Y. Zou, L. Wei, and Y. Wang, Evaluating combination models of solar irradiance on inclined surfaces and forecasting photovoltaic power generation. *IET Smart Grid*, *2*(1), pp.123-130(2019).
108. P. Singh, and N.M. Ravindra, Temperature dependence of solar cell performance—an analysis. *Solar energy materials and solar cells*, *101*, (2012).
109. Sunpower C60 spec sheet (2010), https://www.scribd.com.
110. M. E. Nell, A. M. Barnett, The spectral p–n junction model for tandem solar-cell design, *IEEE Transactions on Electron Devices* 24, (1987).
111. N.D. Kaushika, A. Mishra, and A.K. Rai, Solar photovoltaics. *New Delhi, India*, (2018).
112. T. Saga, Advances in crystalline silicon solar cell technology for industrial mass production. *npg asia materials*, *2*(**3**), (2010).
113. V.V. Starovoitov, and Y.I. Golub; Data normalization in machine learning. In *Informatics* (Vol. 18, No. 3, 2021).
114. L.O. Joel, W. Doorsamy, and B.S. Paul; A review of missing data handling techniques for machine learning. *International Journal of Innovative Technology and Interdisciplinary Sciences*, *5*(3), (2022).
115. J. Yang, S. Rahardja, and P. Fränti; Outlier detection: how to threshold outlier scores?. In *Proceedings of the international conference on artificial intelligence, information processing and cloud computing*, (2019).
116. L. Wilkinson, Visualizing big data outliers through distributed aggregation. *IEEE transactions on visualization and computer graphics*, *24*(1), (2017).
117. NASA. NASA Power; *https://power.larc.nasa.gov/docs/methodology/solar* accessed from (2023).
118. NASA Giovanni; Giovanni (nasa.gov) accessed from (2023).
119. National Meteorological Institute of Ethiopia (NMI); National Meteorology Agency (2023).
120. S. García, J. Luengo, and F. Herrera, *Data preprocessing in data mining*. Cham, Switzerland: Springer International Publishing, Vol. 72, (2015).
121. D. Pyle, *Data preparation for data mining*. morgan kaufmann (1999).

122. B. Mahesh, Machine learning algorithms-a review. *International Journal of Science and Research (IJSR). [Internet]*, *9*(1), (2020).
123. D. G. Erbs, S. A. Klein, J. A. Duffie, Estimation of the diffuse radiation fraction for hourly, daily, and monthly-average global radiation. *Sol. Energy* 28, (1982).
124. E. L. Maxwell, *A quasi-physical model for converting hourly global horizontal to direct normal insolation* (No. SERI/TR-215-3087). *Solar Energy Research Inst., Golden*, CO (USA), (1987).
125. J. Boland, J. Huang, and B. Ridley, Decomposing global solar radiation into its direct and diffuse components. *Renew. Sustain. Energy Rev.*, *28*, (2013).
126. A. Louche, G. Notton, P. Poggi, G. Simonnot, Correlation for direct normal and global horizontal irradiations on a French Mediterranean site. *Sol. Energy*, 46(4), (1991).
127. J. F. Orgill, K. G. T. Hollands, Correlation Equation for hourly diffuse radiation on a horizontal surface. *Sol. Energy* (1977).
128. B. Y. H. Liu, R. C. Jordan, The interrelationship and characteristic distribution of direct, diffuse and total solar radiation. *Sol. Energy*; 4(3), (1960).
129. V. Badescu, A new kind of cloudy sky model to compute instantaneous values of diffuse and global solar irradiance, *Theor. Appl. Climatol.*, 72, (1) (2002).
130. P. S. Koronakis, On the choice of the angle of tilt for south facing solar collectors in the Athens basin area, *Sol. Energy*, 36 (3), (1986).
131. D. T. Reindl, W. A. Beckman, and J. A. Duffie, Evaluation of hourly tilted surface radiation models, *Sol. Energy*, 45 (1), (1990).
132. J. E. Hay, Calculation of monthly mean solar radiation for horizontal and inclined surfaces, *Sol. Energy*, vol. 23 (4), (1979).
133. M. D. Steven and M. H. Unsworth, The angular distribution and interception of diffuse solar radiation below overcast skies, *Q J R Meteorol Soc*., 106 (447), (1980).
134. O. Bamisile, D. Cai, A. Oluwasanmi, C. Ejiyi, C.C. Ukwuoma, O. Ojo, M. Mukhtar, and Q. Huang, Comprehensive assessment, review, and comparison of AI models for solar irradiance prediction based on different time/estimation intervals. *Scientific Reports*, ***12***(1), p.9644 (2022).
135. L. Huang, J. Kang, M. Wan, L. Fang, C. Zhang, and Z. Zeng, Solar radiation prediction using different machine learning algorithms and implications for extreme climate events. *Frontiers in Earth Science*, ***9***, p.596860 (2021).

136. K. Basaran, A. Özçift, and D. Kılınç, A new approach for prediction of solar radiation with using ensemble learning algorithm. *Arabian Journal for Science and Engineering*, *44*, pp.7159-7171 (2019).
137. M. Fazzini, C. Bisci, and P. Billi, The climate of Ethiopia. Landscapes and landforms of Ethiopia, pp.65-87 (2015).
138. M. Fazzini, C. Bisci, and P. Billi, The climate of Ethiopia. *Landscapes and landforms of Ethiopia*, pp.65-87(2015).
139. S.A. Kalogirou, *Solar energy engineering: processes and systems*. Elsevier (2023).
140. B. S. Richards, and A. I. Schäfer, Renewable energy powered water treatment systems. *Sustain. Sci.*, *2*, (2010).
141. M. Iqbal, *An introduction to solar radiation*. Elsevier (2012).
142. M. Fazzini, C. Bisci, and P. Billi, The climate of Ethiopia. *Landscapes and landforms of Ethiopia*, (2015).
143. E. Radziemska, The effect of temperature on the power drop in crystalline silicon solar cells. *Renewable energy*, 28(1), (2003).
144. A. D. Dhass, Y. Prakash, and K. C. Ramya, Effect of temperature on internal parameters of solar cell. *Mater. Today Proc.*, *33*, (2020).
145. M. A. Green, K. Emery, Y. Hishikawa, W. Warta, Solar cell efficiency tables (version 37), Progress in Photovoltaics: *Res. and Appl.,* 19, (2011).
146. B.V. Chikate, Y. Sadawarte, and B.D.C.O.E. Sewagram, The factors affecting the performance of solar cell. *Int. J. Comput. Appl.*, *1*(1), (2015).
147. C. Aksoy Tırmıkçı, and C. Yavuz, Determining optimum tilt angles of solar surfaces in Sakarya, Turkey. *Theoretical and Applied Climatology*, *133*, (2018).
148. T.M. Yunus Khan *et al.*, Optimum location and influence of tilt angle on performance of solar PV panels. *Journal of Thermal Analysis and Calorimetry*, *141*, (2020).
149. E. Alhamer, A. Grigsby, and R. Mulford, The Influence of Seasonal Cloud Cover, Ambient Temperature and Seasonal Variations in Daylight Hours on the Optimal PV Panel Tilt Angle in the United States. *Energies*, *15*(20), (2022).
150. F. Besharat, A.A. Dehghann, A.R. FaGHRh, Empirical models for estimating global solar radiation: A review and case study; *Renewable and Sustainable Energy Reviews,* 21 (2013).

151. J.A. Duffie, and W.A. Beckman, Solar engineering of thermal processes. *New York: Wiley* (1980).
152. H.Z. Al Garni, A. Awasthi, and D. Wright, Optimal orientation angles for maximizing energy yield for solar PV in Saudi Arabia. *Renewable energy*, *133*, (2019).
153. Machidon, D. and M. Istrate, Tilt angle adjustment for incident solar energy increase: A case study for Europe. *Sustainability*, *15*(8), (2023).
154. K. Osmani, M. Ramadan, T. Lemenand, B. Castanier, and A. Haddad, Optimization of PV array tilt angle for minimum levelized cost of energy. *Computers & Electrical Engineering*, *96*, (2021).

Appendices

Table A1: Daily average seasonal peak-sun hour, and its percentage [%] of coverage in Ethiopia.

Seasons	Values [kWh/m2/day]	Area [%]	Seasons	Values [kWh/m2/day]	Area [%]
Winter	5.12-5.48	12.92	Spring	5.28-5.74	15.14
	5.49-5.84	32.94		5.75-6.20	16.90
	5.85-6.21	31.43		6.21-6.65	30.97
	6.22-6.57	22.72		6.66-7.11	36.99
Summer	3.91-4.54	30.12	Autumn	4.68-5.12	18.35
	4.55-5.18	24.11		5.13-5.55	19.87
	5.19-5.81	30.04		5.56-5.99	42.88
	5.82-6.44	15.74		6.0-6.42	18.90

A2. Plain of Array (POA) Irradiance

Table A2: Average seasonal distribution of POA irradiance and its [%] of coverage in Ethiopia.

Seasons	Values [kW/m2]	Area [%]	Seasons	Values [kW/m2]	Area [%]
Winter	1.28-1.35	9.18	Spring	1.27-1.35	8.59
	1.36-1.41	18.98		1.36-1.43	19.68
	1.42-1.48	29.72		1.44-1.51	32.17
	1.49-1.54	42.12		1.52-1.59	39.56
Summer	1.01-1.13	29.60	Autumn	1.14-1.25	24.67
	1.14-1.24	20.59		1.26-1.35	30.99
	1.25-1.36	28.03		1.36-1.45	23.68
	1.37-1.47	21.78		1.46-1.55	20.66

A3. Solar Cell Temperature

Table A3: Average seasonal distribution of solar cell temperature T [oC] and its [%] of coverage in Ethiopia.

Seasons	Values [oC]	Area [%]	Seasons	Values [oC]	Area [%]
Winter	55.26-58.72	30.90	Spring	57.81-62.15	24.55
	58.73-62.18	17.71		62.16-66.48	23.76
	62.19-65.64	23.45		66.49-70.82	38.63
	65.65-69.11	27.93		70.83-75.16	13.07
Summer	44.74-50.50	30.15	Autumn	51.49-56.47	30.95
	50.51-56.27	24.41		56.48-61.46	21.35
	56.28-62.03	27.62		61.47-66.44	37.98

	62.04-67.79	17.83		66.45-71.43	9.72

A4. Solar Cell Parameters

S4.1. Reverse Saturation Current Density (*Jo*)

Table A4: Average seasonal distribution of reverse saturation current density J0 [pA/cm2], (p=10-12) and its [%] of coverage in Ethiopia.

Seasons	Values [*pA/cm2*]	Area [%]	Seasons	Values [*pA/cm2*]	Area [%]
Winter	1.85-3.93	34.13	Spring	2.55-7.06	31.93
	3.94-6.02	18.62		7.07-11.6	23.50
	6.03-8.11	20.63		11.7-16.1	32.80
	8.12-10.2	26.62		16.2-20.6	11.78
Summer	0.456-2.52	51.00	Autumn	1.12-4.19	38.68
	2.53-4.58	24.13		4.20-7.25	20.21
	4.59-6.65	16.12		7.26-10.3	32.40
	6.66-8.71	8.75		10.4-13.4	8.71

A4.2. Short Circuit Current Density (*Jsc*)

Table A5: Average seasonal distribution of short circuit current density Jsc [mA/cm2] and its [%] of coverage in Ethiopia.

Seasons	Values [mA/cm2]	Area [%]	Seasons	Values [mA/cm2]	Area [%]
Winter	35.79-37.79	10.32	Spring	35.41-37.95	12.24
	37.80-39.39.79	25.49		37.96-40.48	17.67
	39.80-41.79	29.65		40.49-43.02	30.53
	41.80-43.79	34.54		43.03-45.56	39.56
Summer	27.39-30.87	29.89	Autumn	31.42-34.53	25.00
	30.88-34.35	19.93		34.54-37.64	24.35
	34.36-37.83	25.14		37.65-40.75	29.82
	37.84-41.3	25.03		40.76-43.86	20.83

A4.3. Short Circuit Current (*Isc*)

Table A6: Average seasonal distribution of short circuit current Isc [A] and its [%] of coverage in Ethiopia.

Seasons	Values [A]	Area [%]	Seasons	Values [A]	Area [%]
Winter	8.71-9.20	10.32	Spring	8.62-9.24	12.24
	9.21-9.68	25.49		9.25-9.85	17.67
	9.69-10.2	29.65		9.86-10.5	30.53
	10.3-10.7	34.54		10.6-11.1	39.56
Summer	6.67-7.51	29.89	Autumn	7.65-8.40	25.00
	7.52-8.36	19.93		8.41-9.16	24.35
	8.37-9.21	25.14		9.17-9.92	29.82
	9.22-10.1	25.03		9.93-10.7	20.83

A4.4. Current at Maximum Power (*Imp*)

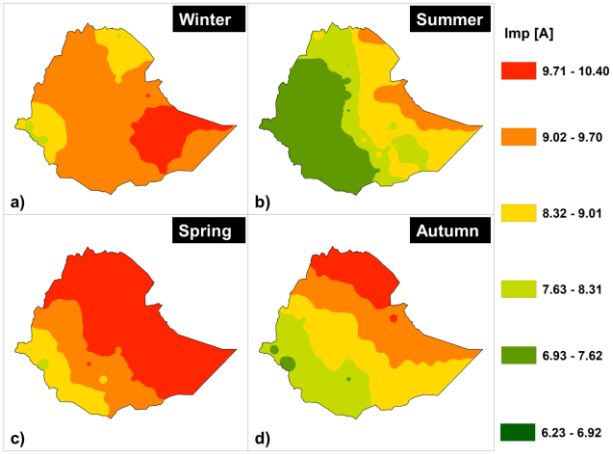

Figure A1: Average seasonal distribution of current at maximum power point Imp [A] over Ethiopia during winter (a), summer (b), spring (c), and autumn (d) seasons.

Table A7: Average seasonal distribution of current at maximum power Imp [A] and its [%] of coverage in Ethiopia.

Seasons	Values [A]	Area [%]	Seasons	Values [A]	Area [%]
Winter	8.14-8.59	10.32	Spring	8.05-8.63	12.24
	8.60-9.05	25.49		8.64-9.21	17.67
	9.06-9.50	29.65		9.22-9.78	30.53
	9.51-9.96	34.54		9.79-10.4	39.56
Summer	6.23-7.02	29.89	Autumn	7.14-7.85	25.00
	7.03-7.81	19.93		7.86-8.56	24.35
	7.82-8.60	25.14		8.57-9.27	29.82
	8.61-9.39	25.03		9.28-9.97	20.83

A4.5. Open Circuit Voltage (*Voc*)

Table A8: Average seasonal distribution of open circuit voltage Voc [V] and its [%] of coverage in Ethiopia.

Seasons	Values [V]	Area [%]	Seasons	Values [V]	Area [%]
Winter	0.638-0.648	9.87	Spring	0.638-0.647	16.32
	0.649-0.657	36.81		0.648-0.656	33.01
	0.658-0.667	31.68		0.657-0.665	33.64
	0.668-0.676	21.65		0.666-0.674	17.04
Summer	0.635-0.643	17.84	Autumn	0.638-0.646	20.60
	0.644-0.651	32.79		0.647-0.654	28.33
	0.652-0.659	30.13		0.655-0.662	28.41
	0.660-0.667	19.24		0.663-0.670	22.66

A4.6. Voltage at Maximum Power (*Vmp*)

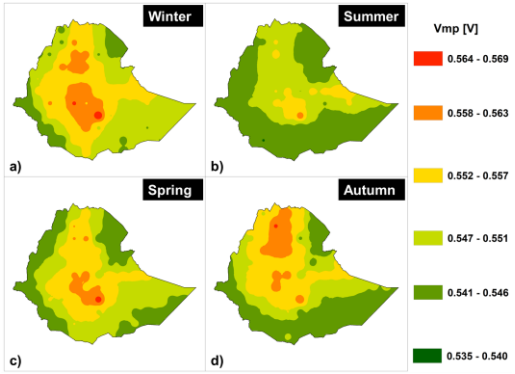

Figure A2: Average seasonal distribution of voltage at maximum power output Vmp [V] over Ethiopia during winter (a), summer (b), spring (c), and autumn (d) seasons.

Table A9: Average seasonal distribution of voltage at maximum power Vmp [V] and its [%] of coverage in Ethiopia.

Seasons	Values [V]	Area [%]	Seasons	Values [V]	Area [%]
Winter	0.537-0.545	9.87	Spring	0.537-0.544	16.32
	0.546-0.553	36.81		0.545-0.552	33.01
	0.554-0.561	31.68		0.553-0.559	33.64
	0.562-0.569	21.65		0.560-0.567	17.04
Summer	0.535-0.541	17.84	Autumn	0.537-0.544	20.60
	0.542-0.548	32.79		0.545-0.551	28.33
	0.549-0.555	30.13		0.552-0.557	28.41
	0.556-0.562	19.24		0.558-0.564	22.66

A4.7. Fill Factor (*FF*)

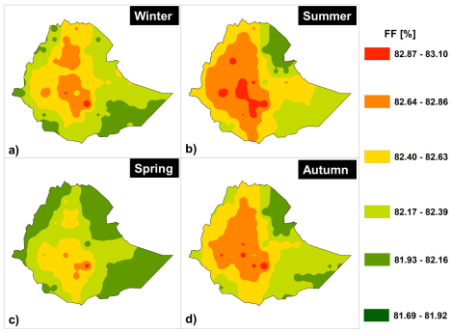

Figure A3: Average seasonal distribution of FF [%] over Ethiopia; a) winter, b) summer, c) spring, and d) autumn seasons.

Table A10: Average seasonal distribution of fill factor (FF) and its [%] of coverage in Ethiopia.

Seasons	Values [%]	Area [%]	Seasons	Values [%]	Area [%]
Winter	81.99-82.27	33.97	Spring	81.69-82.01	11.35
	82.28-82.54	26.23		82.02-82.33	34.09

	82.55-82.82	22.11		82.34-82.64	30.66
	82.83-83.10	17.69		82.65-82.96	23.90
Summer	81.86-82.16	7.82	Autumn	81.86-82.16	6.74
	82.17-82.46	28.11		82.17-82.47	31.94
	82.47-82.76	31.79		82.48-82.78	39.62
	82.77-83.06	32.28		82.79-83.09	21.71

A4.8. Maximum Power (*Pmp*)

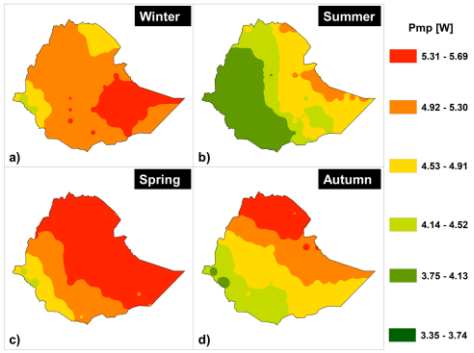

Figure A4: Average seasonal distribution of maximum power output over Pmp [W] over Ethiopia during winter (a), summer (b), spring (c), and autumn (d) seasons.

Table A11Error! Main Document Only.: Average seasonal distribution of maximum power Pmax [W] and its [%] of coverage in Ethiopia.

Seasons	Values [W]	Area [%]	Seasons	Values [W]	Area [%]
Winter	4.39-4.66	8.21	Spring	4.36-4.69	8.70
	4.67-4.93	13.20		4.70-5.03	20.35
	4.94-5.21	31.18		5.04-5.36	33.10
	5.22-5.48	47.41		5.37-5.69	37.85
Summer	3.35-3.81	29.66	Autumn	3.86-4.28	23.91
	3.82-4.28	20.66		4.29-4.70	32.14
	4.29-4.74	28.41		4.71-5.12	23.08
	4.75-5.20	21.26		5.13-5.53	20.87

A5.1. Basic Solar Angle

The basic solar angle diagrams like incident angle (θ), altitude angle (α), solar zenith angle (θ_z), solar azimuth angle (γ), surface azimuth angle (γ_s), and solar tilt angles (β) for different types of tracking mechanisms are illustrated in Figure S1.154,154

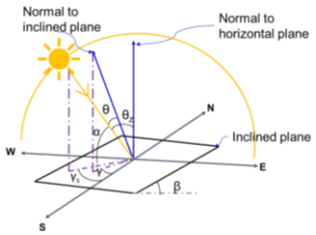

Figure A5: Solar angle diagrams.

A5.2. Cell Parameters at Reference Condition

Table A12: Common PV module values at reference conditions that were implemented in the study: Canadian Solar-Datasheet.

Parameter	Value	Parameter	Value
Cell Type	Mono-Si	α_{sc}	0.0005*Isc
pdc0	420 [W]	β_{voc}	-0.0029*Voc
Vmp	44.9 [V]	γ_{pdc}	-0.37
Imp	9.37 [A]	Tref	25 [oC]
Voc	53.8 [V]	Isc	9.8 [A]

A5.3. Seasonal Model Equations

Table A13: Derived optimal tilt angle models across the country in the autumn .

Equation [R2]	Equation [R2]	Equation [R2]
$\beta_{Opt} = 0.85\phi + 1.69$ [0.85] Boland-Liu-Jordan	$\beta_{Opt} = 0.99\phi + 18.65$ [0.14] DISC-Hay	$\beta_{Opt} = 0.82\phi + 4.67$ [0.92] Louche-Koronakis
$\beta_{Opt} = 0.54\phi + 0.70$ [0.75] Boland-Badescu	$\beta_{Opt} = 0.19\phi + 44.06$ [0.22] DISC-Steven-Unsworth	$\beta_{Opt} = 0.27\phi + 17.11$ [0.29] Louche-Reindl
$\beta_{Opt} = 1.00\phi + 3.14$ [0.88] Boland-Koronakis	$\beta_{Opt} = 0.96\phi + 12.65$ [0.06] Erbs-Liu-Jordan	$\beta_{Opt} = 0.39\phi + 17.14$ [0.25] Louche-Hay
$\beta_{Opt} = 0.25\phi + 19.10$ [0.03] Boland-Reindl	$\beta_{Opt} = 0.69\phi + 0.60$ [0.79] Erbs-Badescu	$\beta_{Opt} = 0.43\phi + 47.25$ [0.22] Louche-Steven-Unsworth
$\beta_{Opt} = 1.00\phi + 15.70$ [0.24] Boland-Hay	$\beta_{Opt} = 1.09\phi + 3.63$ [0.89] Erbs-Koronakis	$\beta_{Opt} = 0.95\phi + 2.71$ [0.87] Orgill-Holland-Liu-Jordan
$\beta_{Opt} = 0.26\phi + 44.74$ [0.22] Boland-Steven-Unsworth	$\beta_{Opt} = 0.19\phi + 18.19$ [0.06] Erbs-Reindl	$\beta_{Opt} = 0.58\phi + 1.82$ [0.74] Orgill-Holland-Badescu
$\beta_{Opt} = 0.43\phi + 23.82$ [0.05] DISC-Liu-Jordan	$\beta_{Opt} = 0.59\phi + 16.70$ [0.20] Erbs-Hay	$\beta_{Opt} = 1.10\phi + 3.97$ [0.90] Orgill-Holland-Koronakis
$\beta_{Opt} = 0.44\phi + 0.59$ [0.76] DISC-Badescu	$\beta_{Opt} = 0.41\phi + 45.57$ [0.23] Erbs-Steven-Unsworth	$\beta_{Opt} = 0.18\phi + 18.18$ [0.07] Orgill-Holland-Reindl
$\beta_{Opt} = 0.94\phi + 2.59$ [0.87] DISC-Koronakis	$\beta_{Opt} = 0.99\phi + 2.92$ [0.89] Louche-Liu-Jordan	$\beta_{Opt} = 0.53\phi + 16.54$ [0.23] Orgill-Holland-Hay
$\beta_{Opt} = 0.47\phi + 19.83$ [0.05] DISC-Reindl	$\beta_{Opt} = 0.74\phi + 1.25$ [0.83] Louche-Badescu	$\beta_{Opt} = 0.37\phi + 46.56$ [0.85] Orgill-Holland-Steven-Unsworth

Table A14: Derived optimal tilt angle models across the country in the spring season.

Equation [R2]	Equation [R2]	Equation [R2]
$\beta_{Opt} = 0.40\phi - 2.47$ [0.79]	$\beta_{Opt} = 0.89\phi - 5.37$ [0.77]	$\beta_{Opt} = 0.54\phi - 3.34$ [0.80]
Boland-Liu-Jordan	DISC-Hay	Louche-Koronakis
$\beta_{Opt} = 0.27\phi - 1.67$ [0.74]	$\beta_{Opt} = 0.35\phi + 46.04$ [0.28]	$\beta_{Opt} = 0.59\phi - 3.72$ [0.78]
Boland-Badescu	DISC-Steven-Unsworth	Louche-Reindl
$\beta_{Opt} = 0.48\phi - 2.96$[0.79]	$\beta_{Opt} = 1.00\phi + 2.65$ [0.00]	$\beta_{Opt} = 0.75\phi - 4.62$ [0.79]
Boland-Koronakis	Erbs-Liu-Jordan	Louche-Hay
$\beta_{Opt} = 0.61\phi - 3.76$ [0.75]	$\beta_{Opt} = 0.32\phi - 2.04$ [0.76]	$\beta_{Opt} = 0.90\phi + 51.14$ [0.30]
Boland-Reindl	Erbs-Badescu	Louche-Steven-Unsworth
$\beta_{Opt} = 0.84\phi - 5.06$ [0.78]	$\beta_{Opt} = 0.51\phi - 3.13$ [0.79]	$\beta_{Opt} = 0.45\phi - 2.80$ [0.80]
Boland-Hay	Erbs-Koronakis	Orgill-Holland-Liu-Jordan
$\beta_{Opt} = 0.54\phi + 47.15$ [0.29]	$\beta_{Opt} = 0.60\phi - 3.69$ [0.06]	$\beta_{Opt} = 0.32\phi - 2.0$[0.76]
Boland-Steven-Unsworth	Erbs-Reindl	Orgill-Holland-Dadescu
$\beta_{Opt} = 0.02\phi + 20.96$ [0.00]	$\beta_{Opt} = 0.79\phi - 4.78$ [0.78]	$\beta_{Opt} = 0.51\phi - 3.19$ [0.80]
DISC-Liu-Jordan	Erbs-Hay	Orgill-Holland-Koronakis
$\beta_{Opt} = 0.23\phi - 1.43$ [0.73]	$\beta_{Opt} = 0.81\phi + 49.28$ [0.29]	$\beta_{Opt} = 0.60\phi - 3.78$ [0.77]
DISC-Badescu	Erbs-Steven-Unsworth	Orgill-Holland-Reindl
$\beta_{Opt} = 0.45\phi - 2.75$ [0.80]	$\beta_{Opt} = 0.47\phi - 2.97$ [0.78]	$\beta_{Opt} = 0.79\phi - 4.85$ [0.80]
DISC-Koronakis	Louche-Liu-Jordan	Orgill-Holland-Hay
$\beta_{Opt} = 0.52\phi - 3.19$ [0.64]	$\beta_{Opt} = 0.34\phi - 2.18$ [0.76]	$\beta_{Opt} = 0.66\phi + 49.74$ [0.10]
DISC-Reindl	Louche-Badescu	Orgill-Holland-Steven-Unsworth

Table A15: Derived optimal tilt angle models across the country in the summer season.

Equation [R2]	Equation [R2]	Equation [R2]
$\beta_{Opt} = 0$	$\beta_{Opt} = 0$	$\beta_{Opt} = 0$
Boland-Liu-Jordan	DISC-Hay	Louche-Koronakis
$\beta_{Opt} = 0$	$\beta_{Opt} = 0.13\phi + 43.77$ [0.06]	$\beta_{Opt} = 0$
Boland-Badescu	DISC-Steven-Unsworth	Louche-Reindl
$\beta_{Opt} = 0$	$\beta_{Opt} = 0$	$\beta_{Opt} = 0$
Boland-Koronakis	Erbs-Liu-Jordan	Louche-Hay
$\beta_{Opt} = 0$	$\beta_{Opt} = 0$	$\beta_{Opt} = 0.24\phi + 46.81$[0.04]
Boland-Reindl	Erbs-Badescu	Louche-Steven-Unsworth
$\beta_{Opt} = 0$	$\beta_{Opt} = 0$	$\beta_{Opt} = 0$
Boland-Hay	Erbs-Koronakis	Orgill-Holland-Liu-Jordan
$\beta_{Opt} = 0.22\phi + 43.78$ [0.08]	$\beta_{Opt} = 0$	$\beta_{Opt} = 0$
Boland-Steven-Unsworth	Erbs-Reindl	Orgill-Holland-Dadescu
$\beta_{Opt} = 0.01\phi + 8.13$ [0.00]	$\beta_{Opt} = 0$	$\beta_{Opt} = 0$
DISC-Liu-Jordan	Erbs-Hay	Orgill-Holland-Koronakis
$\beta_{Opt} = 0$	$\beta_{Opt} = 0$	$\beta_{Opt} = 0$

DISC-Badescu	Erbs-Steven-Unsworth	Orgill-Holland-Reindl
$\beta_{Opt} = 0$	$\beta_{Opt} = 0$	$\beta_{Opt} = 0$
DISC-Koronakis	Louche-Liu-Jordan	Orgill-Holland-Hay
$\beta_{Opt} = 0$	$\beta_{Opt} = 0$	$\beta_{Opt} = 0.25\phi + 45.64$ [0.05]
DISC-Reindl	Louche-Badescu	Orgill-Holland-Steven-Unsworth

Table A16: Derived optimal tilt angle models across the country in the winter season.

Equation [R2]	Equation [R2]	Equation [R2]
$\beta_{Opt} = 0.43\phi + 12.54$ [0.30]	$\beta_{Opt} = 0.66\phi + 24.01$ [0.65]	$\beta_{Opt} = 0.39\phi + 20.21$ [0.36]
Boland-Liu-Jordan	DISC-Hay	Louche-Koronakis
$\beta_{Opt} = 0.18\phi + 8.70$ [0.09]	$\beta_{Opt} = 0.22\phi + 48.8$ [0.21]	$\beta_{Opt} = 1.84\phi + 14.10$ [0.86]
Boland-Badescu	DISC-Steven-Unsworth	Louche-Reindl
$\beta_{Opt} = 0.79\phi + 14.71$ [0.51]	$\beta_{Opt} = 0.98\phi + 28.52$ [0.06]	$\beta_{Opt} = 1.48\phi + 20.53$ [0.89]
Boland-Koronakis	Erbs-Liu-Jordan	Louche-Hay
$\beta_{Opt} = 2.06\phi + 14.86$ [0.73]	$\beta_{Opt} = 0.26\phi + 10.37$ [0.13]	$\beta_{Opt} = 0.47\phi + 57.7$ [0.19]
Boland-Reindl	Erbs-Badescu	Louche-Steven-Unsworth
$\beta_{Opt} = 1.59\phi + 22.51$ [0.72]	$\beta_{Opt} = 0.51\phi + 18.37$ [0.37]	$\beta_{Opt} = 0.60\phi + 13.97$ [0.51]
Boland-Hay	Erbs-Koronakis	Orgill-Holland-Liu-Jordan
$\beta_{Opt} = 0.28\phi + 51.0$ [0.21]	$\beta_{Opt} = 1.94\phi + 13.97$ [0.81]	$\beta_{Opt} = 0.36\phi + 9.99$ [0.26]
Boland-Steven-Unsworth	Erbs-Reindl	Orgill-Holland-Dadescu
$\beta_{Opt} = 0.71\phi + 46.2$ [0.09]	$\beta_{Opt} = 1.56\phi + 20.74$ [0.81]	$\beta_{Opt} = 0.50\phi + 18.60$ [0.42]
DISC-Liu-Jordan	Erbs-Hay	Orgill-Holland-Koronakis
$\beta_{Opt} = 0.16\phi + 7.22$ [0.10]	$\beta_{Opt} = 0.44\phi + 55.3$ [0.21]	$\beta_{Opt} = 1.90\phi + 14.15$ [0.83]
DISC-Badescu	Erbs-Steven-Unsworth	Orgill-Holland-Reindl
$\beta_{Opt} = 0.84\phi + 12.42$ [0.52]	$\beta_{Opt} = 0.61\phi + 14.78$ [0.54]	$\beta_{Opt} = 1.51\phi + 20.88$ [0.86]
DISC-Koronakis	Louche-Liu-Jordan	Orgill-Holland-Hay
$\beta_{Opt} = 2.0\phi + 17.81$ [0.64]	$\beta_{Opt} = 0.39\phi + 10.72$ [0.27]	$\beta_{Opt} = 0.38\phi + 55.1$ [0.14]
DISC-Reindl	Louche-Badescu	Orgill-Holland-Steven-Unsworth

A5.4. Annual Model Equations

Table A17: Derived annual optimal tilt angle models across the country.

Equation [R2]	Equation [R2]	Equation [R2]
$\beta_{Opt} = 0.48\phi + 1.96$ [0.68	$\beta_{Opt} = 0.49\phi + 13.64$ [0.22]	$\beta_{Opt} = 0.65\phi + 3.02$ [0.74]
Boland-Liu-Jordan	DISC-Hay	Louche-Koronakis
$\beta_{Opt} = 0.27\phi + 122$ [0.62]	$\beta_{Opt} = 0.11\phi + 45.72$ [0.06]	$\beta_{Opt} = 0.92\phi + 5.28$ [0.54]
Boland-Badescu	DISC-Steven-Unsworth	Louche-Reindl
$\beta_{Opt} = 0.54\phi + 2.79$ [0.67]	$\beta_{Opt} = 0.74\phi + 10.95$ [0.80]	$\beta_{Opt} = 0.93\phi + 7.28$ [0.53]
Boland-Koronakis	Erbs-Liu-Jordan	Louche-Hay
$\beta_{Opt} = 0.75\phi + 8.69$ [0.30]	$\beta_{Opt} = 0.36\phi + 1.38$ [0.64]	$\beta_{Opt} = 0.23\phi + 50.92$ [0.05]

Boland-Reindl $\beta_{Opt} = 0.62\phi + 11.67$ [0.27] Boland-Hay $\beta_{Opt} = 0.15\phi + 47.02$ [0.06] Boland-Steven-Unsworth $\beta_{Opt} = -0.33\phi + 28.8$ [0.03] DISC-Liu-Jordan $\beta_{Opt} = 0.21\phi + 1.06$ [0.52] DISC-Badescu $\beta_{Opt} = 0.50\phi + 2.46$ [0.69] DISC-Koronakis $\beta_{Opt} = 0.59\phi + 10.83$ [0.19] DISC-Reindl	Erbs-Badescu $\beta_{Opt} = 0.57\phi + 3.33$ [0.65] Erbs-Koronakis $\beta_{Opt} = 0.18\phi + 7.10$ [0.37] Erbs-Reindl $\beta_{Opt} = 0.77\phi + 9.40$ [0.36] Erbs-Hay $\beta_{Opt} = 0.22\phi + 48.89$ [0.06] Erbs-Steven-Unsworth $\beta_{Opt} = 0.59\phi + 2.19$ [0.77] Louche-Liu-Jordan $\beta_{Opt} = 0.41\phi + 1.34$ [0.72] Louche-Badescu	Louche-Steven-Unsworth $\beta_{Opt} = 0.47\phi + 2.68$ [0.68] Orgill-Holland-Liu-Jordan $\beta_{Opt} = 0.37\phi + 1.32$ [0.66] Orgill-Holland-Dadescu $\beta_{Opt} = 0.63\phi + 2.99$ [0.72] Orgill-Holland-Koronakis $\beta_{Opt} = 0.91\phi + 6.11$ [0.45] Orgill-Holland-Reindl $\beta_{Opt} = 0.88\phi + 8.37$ [0.44] Orgill-Holland-Hay $\beta_{Opt} = 0.21\phi + 49.52$ [0.06] Orgill-Holland-Steven-Unsworth

A5.5. Seasonal Distribution Map

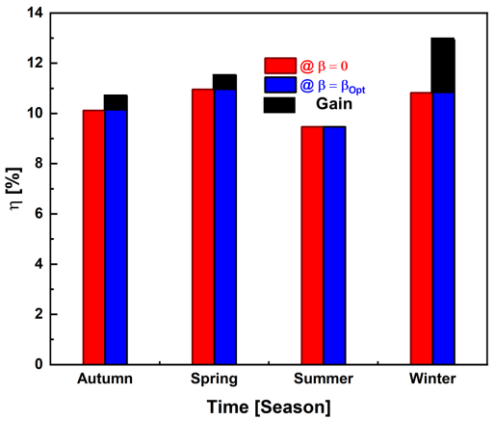

Figure A6: Solar energy gain [in %] is due to the PV module being mounted at an optimal tilt angle relative to the horizontal.

A5.6. Solar Tracking Mechanisms

A5.6.1 Vertical Axis Tracking

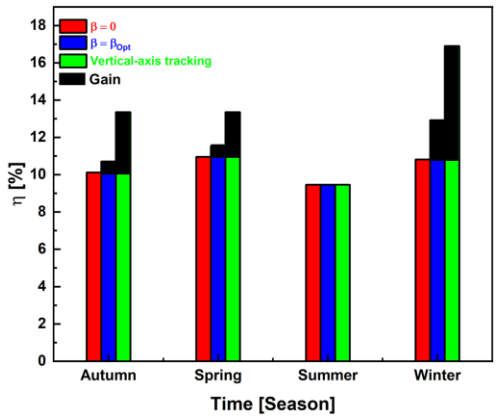

Figure A7: Solar energy gain [in %] due to vertical-axis tracked PV module relative to mounted at optimal tilt angle and mounted at horizontal.

A5.6.2 East-West Tracking

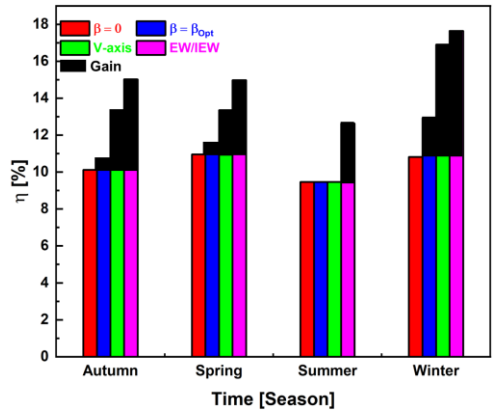

Figure A8: Solar energy gain [in %] due to EW/IEW tracked PV module relative to mounted at optimal tilt angle, mounted at horizontal, and vertical-axis tracking.

A5.6.3 North-South Axis Tracking

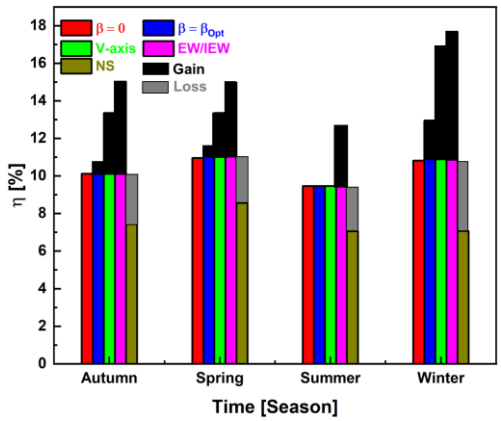

Figure A9: Solar energy loss [in %] due to NS tracked PV module relative to mounted at optimal tilt angle, mounted at horizontal, vertical-axis tracked, and EW/IEW tracked.

A5.6.4 Dual Axis Tracking

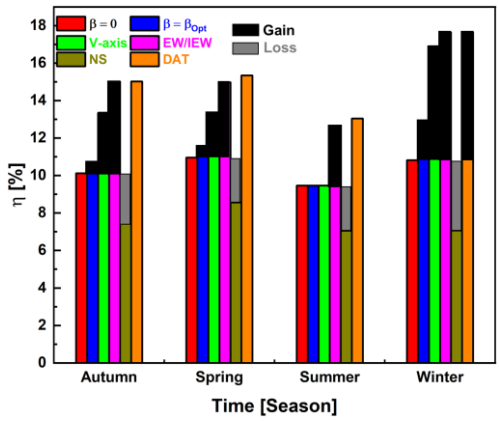

Figure A10: Solar energy gain [in %] due to dual/full tracked PV module relative to mounted at optimal tilt angle, mounted at horizontal, vertical-axis tracked, EW/IEW tracked, and NS tracked.